THE UNIVERSITY OF CHICAGO

ION TRANSPORT IN HYDRATED POLYMER ELECTROLYTES –
ROLE OF SEGMENTAL DYNAMICS, WATER CONCENTRATION, AND INTERFACE

A DISSERTATION SUBMITTED TO
THE FACULTY OF THE PRITZKER SCHOOL OF MOLECULAR ENGINEERING
IN CANDIDACY FOR THE DEGREE OF
DOCTOR OF PHILOSOPHY

BY
KAI WANG

CHICAGO, ILLINOIS
AUGUST 2023

TABLE OF CONTENTS

LIST OF FIGURES

LIST OF TABLES

ACKNOWLEDGEMENTS

I would like to express my deepest gratitude and appreciation to all those who have supported and contributed to the completion of this dissertation. The journey towards earning my Ph.D. has been both challenging and rewarding, and I could not have accomplished this feat without the help and encouragement of numerous individuals.

First and foremost, I would like to extend my heartfelt thanks to my advisor, Prof. Paul F. Nealey, for his invaluable guidance, unwavering patience, and continuous support throughout my research projects. His expertise, insights, and mentorship have been instrumental in shaping my academic and professional growth. I am also grateful to the members of my dissertation committee, Prof. Shrayesh N. Patel and Prof. Matthew V. Tirrell, for their constructive feedback, helpful suggestions, and steadfast encouragement throughout the development and refinement of my work.

My sincere appreciation goes to my colleagues and friends at PME of UChicago and beyond, who have provided a stimulating and nurturing environment for my research. A special thanks to Dr. Zhongyang Wang, who has been a great companion throughout the past few years, discussing science and sharing life experiences. I am grateful to Mincheol Kim, whose enthusiasm for research and willingness to offer help has been inspiring; Christopher Eom, a highly productive and skilled chemist; Sarah Chen, and Ge Sun from the De Pablo group, who have demonstrated profound intelligence and a deep understanding of polymer physics. I'd also like to thank Dr. Daniel Sunday from NIST for his relentless help with X-ray scattering measurements.

Additionally, I am grateful to the former Nealey group members. Jiaxing Ren, Xuanxuan Chen, Moshe Dolejsi, Dr. Xiao Li, Yu Kambe, and Jiajing Li were the first people I met in 2017 as a summer research undergrad. Thanks to you all, I gained beautiful and unforgettable memories in the Nealey Lab, which inspired me to join the group as a Ph.D. student the following year. I also want to thank former group members Dr. Hongbo Feng, Dr. Daniel Sharon, Peter Bennington, and Dr. Whitney Loo, who generously shared their research experiences with me. Lastly, I would like to extend my gratitude to the rest of the current Nealey group members such as Wen Chen and Kushal Bagchi as well as the people I have met during my time at UChicago.

My deepest appreciation goes to my family for their unwavering love, understanding, and support throughout this journey. Being far from family during my Ph.D. wasn't easy, especially during the COVID-19 pandemic. Fortunately, I met my wife, Fangyuan Zhao, during that time. You are a well-rounded, independent-minded, kind-hearted, and magnanimous woman, excelling both inside and out. We have faced many difficulties together, and I am grateful for your constant encouragement and confidence in me. Your love has been the pillar that has sustained me through the darkest and most challenging times. I am honored to accompany you as the most enduring testament to my love.

Abstract

Solid polymer electrolytes (SPEs) have gained prominence for their potential in fuel cell performance. However, the acidic environment in which PEMs operate limits the choice of catalysts to precious metals such as platinum. As an alternative, anion exchange membrane fuel cells (AEMFCs) operate in an alkaline environment, facilitating oxygen reduction and fuel oxidation reactions and permitting the use of low-cost, non-noble metal catalysts. Despite this, AEMs typically exhibit lower ionic conductivity than PEMs due to the intrinsically lower mobility of OH^-.

In this thesis, we studied ion transport in polymer electrolytes in thin film format, with which extrinsic factors can be avoided and insights into the molecular level ion transport mechanism can be obtained. In chapter 3, we used crosslinking to tune the segmental dynamics of the polymer chain to study the effect on ion transport property. The reduced chain dynamics has no influence on ion transport, instead, the water concentration in the polymer was found to be the key parameters that determined the ion transport efficiency. In chapter 4, we investigated how the interface in block copolymer electrolytes affect ion transport through the confinement of water. BCEs with different molecular weights were chosen to change the volume fraction of interface. The higher volume fraction of interface in lower molecular weight polymer can more effectively confine water in the interface, leading to higher conductivity due to higher water concentration. MD simulation further explains the reason for the confinement of water in the interface. More free volume presents at the interface compared to the bulk, which enables accommodation of water without experiencing excessive swelling. These studies can shed light on the design and optimization of polymer electrolytes to solve the inferior conductivity problem for the AEMFCs.

CHAPTER 1

INTRODUCTION

1.1 Anion Exchange Membranes

Anion exchange membranes (AEMs) are a unique class of solid polymer electrolytes that have garnered significant attention in the scientific community due to their versatility and potential for broad applications. These membranes are characterized by their ability to selectively transport anions, which are negatively charged ions, across the membrane while effectively blocking the passage of other ions and molecules.[1] This selective ion transport capability enables AEMs to be utilized in a diverse range of electrochemical energy conversion and storage devices, as well as in separation and purification processes.[2]

AEMs are typically composed of a polymeric backbone with positively charged functional groups, which are responsible for facilitating anion transport through the membrane. These functional groups, such as quaternary ammonium or phosphonium cations, interact with anions and enable their movement from one side of the membrane to the other.[3] As a result, AEMs play a pivotal role in the efficient functioning of various electrochemical devices, including but not limited to fuel cells, batteries, electrolyzers, capacitive deionization systems, and redox flow batteries.[4] Their applications also extend to other fields, such as water treatment, where they can help remove contaminants and pollutants from water by selective ion transport.[5]

The use of AEMs in other electrochemical devices have been explored, such as batteries and electrolyzers. In these applications, AEMs can provide a stable and efficient platform for selective ion transport, which is essential for high-performance energy storage and conversion.[6,7] Moreover, the development of AEMs with tailored properties and functionalities has opened up new possibilities for their integration into next-generation electrochemical systems, offering potential breakthroughs in energy efficiency, cost-effectiveness, and environmental sustainability.

In recent years, there has been a growing interest in developing AEMs for sustainable energy conversion and storage systems. This is primarily driven by the global need for clean, renewable energy sources and technologies that can efficiently store and convert energy while minimizing environmental impact.[8] For instance, AEMs have been extensively studied for their potential in fuel cell applications, where they can offer several advantages over traditional proton exchange membranes (PEMs). A typical schematic diagram of AEM fuel cell is presented in Figure 1.1.

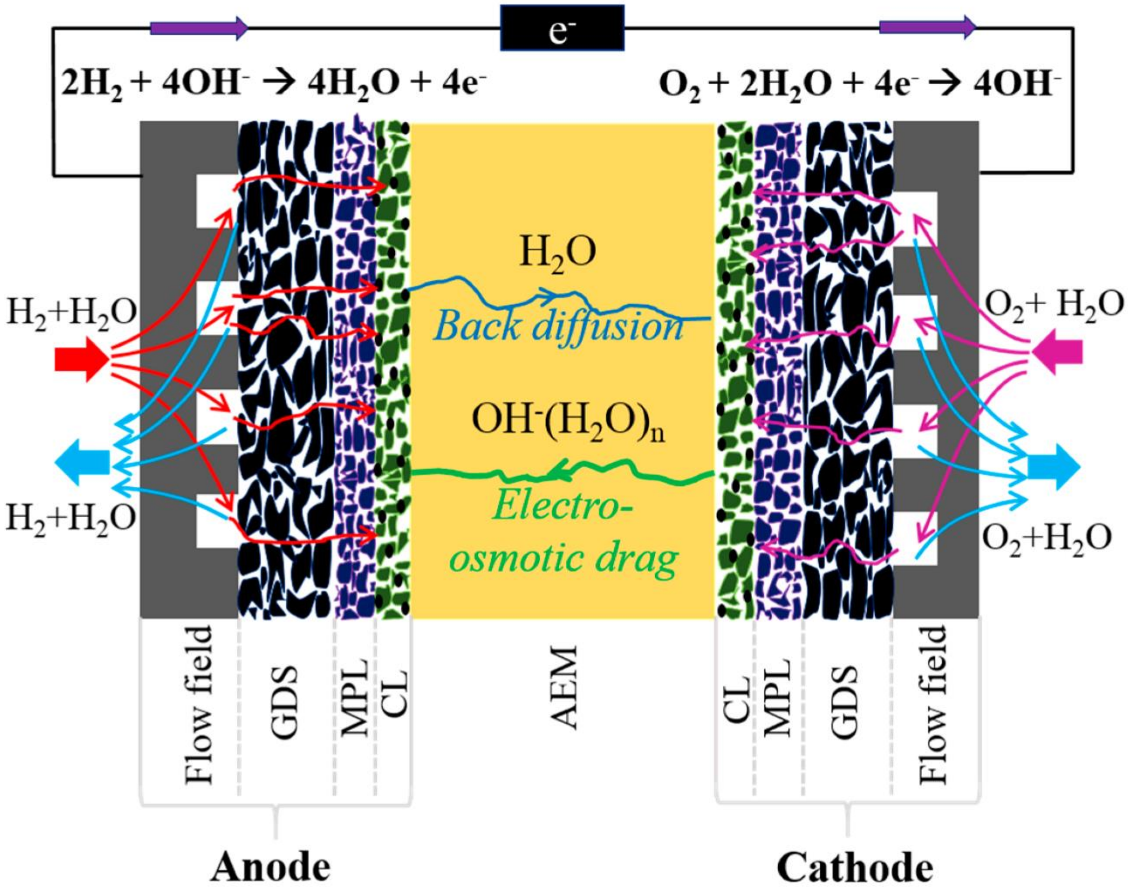

Figure 1.1 Schematic diagram of an anion exchange membrane fuel cell (AEMFC). Reproduced with permission from Truong, *et al*.[9] Copyright (2019) MDPI.

1.1.1 Advantages of anion exchange membranes

Anion exchange membranes (AEMs) have gained significant attention in recent years as an alternative to traditional proton exchange membranes (PEMs) in fuel cell applications. AEMs offer several advantages, including the use of non-precious metal catalysts, higher tolerance to impurities, and improved fuel crossover properties.[2,10] These advantages make AEMs particularly attractive for alkaline anion exchange membrane fuel cells (AEMFCs), which have the potential to provide cost-effective and efficient solutions for energy conversion and storage.[11]

A key advantage of using AEMs in fuel cells is their compatibility with non-precious metal catalysts, such as nickel and silver, which are considerably cheaper than the platinum-based catalysts required for PEMFCs.[12] The use of non-precious metal catalysts can significantly reduce the overall cost of fuel cell systems and promote their widespread adoption for various applications.[13] Another advantage of AEMs is their higher tolerance to impurities, such as carbon dioxide (CO2) and trace amounts of sulfur compounds. PEMFCs are sensitive to impurities, which can poison the catalysts and reduce the overall performance of the fuel cell system. AEMFCs, on the other hand, can better tolerate these impurities, leading to increased durability and lower maintenance requirements.[14] Improved fuel crossover properties are also an important advantage of AEMs in fuel cell applications. Fuel crossover, which occurs when fuel molecules permeate through the membrane to the opposite electrode, can cause decreased efficiency and power output in fuel cells.[15] AEMs can exhibit lower fuel crossover rates compared to PEMs, resulting in higher fuel utilization efficiency and improved performance.[15] In addition to these advantages, AEMs can facilitate the use of liquid fuels, such as alcohols, which can provide higher energy densities than gaseous fuels like hydrogen.[16] This can potentially enable the development of compact and high-energy fuel cell systems suitable for portable and mobile applications.

Overall, the advantages of AEMs in fuel cell applications underscore their importance and potential in the development of cost-effective, efficient, and durable fuel cell systems. Continued research and development of AEMs will be essential to unlocking their full potential in the fuel cell industry.

1.1.2 Challenges in the AEMs field

The development of high-performance anion exchange membranes (AEMs) is critical to advancing electrochemical energy conversion and storage technologies, as well as other applications, such as water treatment and separation processes. Despite the significant progress made in recent years, AEM research still faces several challenges that need to be addressed to optimize their performance and promote widespread adoption.

1.1.2.1 Ionic Conductivity

The ionic conductivity of anion exchange membranes (AEMs) is a critical parameter that significantly affects the performance of electrochemical devices, such as fuel cells, batteries, and electrolyzers. AEMs facilitate the transport of anions (negatively charged ions) across the membrane, and their efficiency is dependent on the rate of ion transport, which is influenced by the membrane's ionic conductivity. In comparison to proton exchange membranes (PEMs), AEMs typically exhibit lower ionic conductivity, which poses a challenge for aiming to develop high-performance AEM-based devices.[1] To enhance the ionic conductivity of AEMs, various strategies and approaches are being explored.

For example, optimization of Ion Exchange Capacity (IEC) is the most common strategy. The IEC of an AEM is defined as the number of exchangeable ions per unit mass of the membrane. Higher IEC values are typically associated with increased ionic conductivity, as more ion-conducting pathways are available for anion transport.[2] However, excessive IEC may lead to increased swelling and reduced mechanical stability, necessitating a careful balance between IEC and other properties. Researchers are working on optimizing IEC by tuning the density and distribution of cationic functional groups in AEMs, thus enhancing ionic conductivity without compromising membrane integrity.[17]

The structure of the polymer matrix also plays a significant role in determining the ionic conductivity of AEMs. Novel polymer structures have been developed, such as block copolymers, graft copolymers, and comb-shaped architectures, to facilitate efficient anion transport. These structures can promote the formation of well-defined and continuous ion-conducting pathways within the membrane, leading to improved ionic conductivity.[3] Additionally, some groups are examining the use of supramolecular assembly and self-assembly techniques to create ordered nanostructures within the AEMs, which may further enhance ionic conductivity.[18]

1.1.2.2 Mechanical strength

Mechanical strength is a critical factor for the structural integrity and durability of anion exchange membranes (AEMs) in various applications, such as fuel cells, batteries, and water treatment processes. AEMs with poor mechanical properties are susceptible to failure, which can result in reduced device performance, shortened lifetimes, and increased maintenance costs. Therefore, enhancing the mechanical strength of AEMs without compromising other properties, such as ionic conductivity and chemical stability, is a significant challenge in AEM research.

1.1.2.2 Water management

Proper water management in anion exchange membranes (AEMs) is crucial for their performance in electrochemical devices, such as fuel cells and electrolyzers. The presence of water in AEMs affects various properties, including ionic conductivity, mechanical strength, and chemical stability. An optimal water content must be maintained within the AEMs to achieve high ionic conductivity without compromising mechanical integrity and chemical stability.[1] Different aspects of water management in AEMs are necessary to be understood to better understand and control the water-related phenomena in these materials.

The water uptake of AEMs is defined as the amount of water absorbed by the membrane per unit mass or volume. Swelling refers to the dimensional change of the membrane upon water absorption. High water uptake can enhance ionic conductivity, as water facilitates anion transport within the membrane.[2] However, excessive swelling can compromise the mechanical strength and dimensional stability of the AEMs. Lots of efforts have been done to study the water uptake and swelling behavior of AEMs to develop materials with an optimal balance between ionic conductivity and mechanical properties.[10]

Novel AEM designs to achieve optimal water management are under investigation. This includes the development of materials with controlled hydrophilic-hydrophobic domains, where water is selectively distributed within the membrane, facilitating efficient anion transport without causing excessive swelling.[19] In addition, researchers are investigating the use of multifunctional polymers and nanostructured materials, which can provide a balance between water uptake, transport, and retention, resulting in improved overall performance and stability.[3]

1.2 Crosslinked Anion Exchange Membranes

Crosslinking refers to the process of forming covalent or non-covalent bonds between polymer chains to create a network structure. In the context of anion exchange membranes (AEMs), crosslinking provides a means to improve various properties, such as mechanical strength, dimensional stability, and chemical resistance.[1] As shown in Figure 1.2, N,N,N′,N′-tetramethyl-1,6-hexanediamine (TMHDA), which can be used as both ionic exchanging groups and crosslinker, was widely applied in the preparation of AEMs. The crosslinked network structure restricts the mobility of polymer chains, resulting in a more rigid and robust material. Crosslinking can be achieved through chemical reactions involving multifunctional monomers or crosslinking agents or through physical interactions, such as hydrogen bonding or self-assembly.[10]

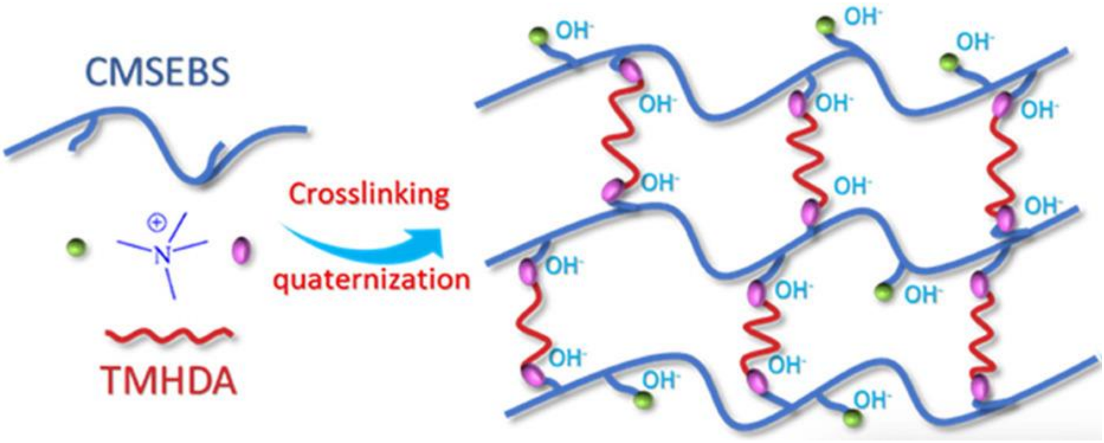

Figure 1.2 Schematic diagram of crosslinked anion exchange membrane. Reprinted with permission from Hao, *et al.*[20] Copyright (2018) Elsevier.

The incorporation of crosslinked structures in AEMs is crucial for their performance in electrochemical devices, such as fuel cells, batteries, and water treatment processes. AEMs without sufficient crosslinking may suffer from poor mechanical strength, leading to membrane failure and reduced device performance. Additionally, non-crosslinked AEMs may exhibit excessive swelling when exposed to water, causing dimensional instability and increased resistance to ion transport.[2] Crosslinking helps to address these issues by providing a more stable and robust membrane structure that can withstand the demanding operating conditions typically encountered in electrochemical applications. Furthermore, crosslinking can be used to fine-tune the ion conductivity of AEMs by controlling the density and distribution of ion-conducting channels within the membrane.[21]

1.2.1 Challenges and limitations in crosslinked AEMs

One of the major challenges in the development of crosslinked AEMs is determining the optimal crosslinking density. The crosslinking density significantly impacts the membrane's mechanical strength, ion conductivity, water uptake, and swelling behavior.[1] A higher crosslinking density can result in improved mechanical strength and reduced swelling but may also lead to lower ion conductivity due to restricted ion transport within the polymer network. On the other hand, a lower crosslinking density may provide higher ion conductivity but compromise the mechanical strength and dimensional stability.[10] Therefore, finding the optimal balance between crosslinking density and membrane properties is crucial for achieving high-performance crosslinked AEMs.

As mentioned earlier, there is often a trade-off between mechanical strength and ion conductivity in crosslinked AEMs. The challenge lies in developing membranes with both high mechanical strength and high ion conductivity. To address this issue, researchers have been investigating various crosslinking strategies, such as the use of multifunctional monomers, self-assembly techniques, and the incorporation of nanofillers or block copolymers. These strategies aim to create materials with tailored structures that facilitate efficient ion transport while maintaining mechanical integrity.

Furthermore, crosslinked AEMs often require complex synthesis and processing methods, which can hinder their scalability and commercial viability. For example, the use of chemical crosslinking agents or multifunctional monomers may involve multistep synthetic procedures and the need for precise control over reaction conditions.[22] Furthermore, some crosslinking strategies may result in materials with limited solubility or processability, making them challenging to fabricate into thin, uniform membranes.[12] Overcoming these limitations will require the development of new materials and crosslinking methods that are compatible with large-scale manufacturing processes.

1.2.2 Recent advances and future perspectives in crosslinked AEMs

In recent years, researchers have focused on devising innovative crosslinking strategies to enhance the performance of AEMs by tailoring their structures to facilitate efficient ion transport, while maintaining mechanical integrity and chemical stability. The use of multifunctional monomers in crosslinked AEMs has been extensively studied as a means to create materials with well-defined crosslinked networks, enabling greater control over the properties of the membranes.[16] For example, researchers have employed multi-armed monomers or crosslinkers containing multiple reactive groups that can react with multiple polymer chains simultaneously, resulting in a more interconnected network structure that provides enhanced mechanical strength, reduced water uptake, and improved ion conductivity.

Additionally, self-assembly techniques have emerged as a promising approach for the fabrication of crosslinked AEMs with hierarchical and ordered structures.[23] By controlling the molecular architecture and self-assembly conditions, researchers have been able to design AEMs with nanoscale ionic domains that facilitate efficient ion transport and optimize mechanical properties. The incorporation of nanofillers, such as carbon nanotubes, graphene oxide, and metal-organic frameworks, into crosslinked AEMs has also been investigated to enhance the membranes' performance. These nanofillers can improve the mechanical strength, ion conductivity, and chemical stability of the membranes through the formation of conductive pathways and reinforcement of the polymer matrix.

Lastly, block copolymer-based systems have gained attention as a platform for the development of crosslinked AEMs.[20] Block copolymers can self-assemble into various nanostructures, enabling the precise control of membrane morphology and the formation of interconnected ionic channels. By manipulating the composition, molecular weight, and crosslinking density, researchers have demonstrated the potential to optimize the performance of these membranes, achieving a balance between mechanical strength, ion conductivity, and water uptake.

The field of crosslinked AEMs has witnessed significant advancements in recent years, with the development of novel materials, crosslinking strategies, and functional properties. The future of crosslinked AEMs lies in further optimization of their structure-property relationships, the exploration of new materials and synthesis methods, and the integration of advanced functionalities, such as self-healing and bio-inspired properties. These innovations will undoubtedly contribute to the realization of high-performance, durable, and cost-effective AEMs for a wide range of electrochemical applications.

1.3 Block Copolymer Electrolytes for AEMs

The use of block copolymer electrolytes as anion exchange membranes (AEMs) has attracted considerable attention due to their unique properties and potential advantages in various electrochemical applications. Block copolymers are macromolecules composed of two or more chemically distinct polymer blocks covalently linked together. The properties of block copolymer AEMs can be tailored by adjusting the composition, molecular weight, and block ratios of the copolymer. This enables the optimization of key membrane properties, such as ion conductivity, water uptake, and mechanical strength, to meet specific application requirements.[24–27]

1.3.1 Block copolymer self-assembly

Block copolymer self-assembly is a fascinating and versatile phenomenon observed in the behavior of block copolymers, which are macromolecules composed of two or more chemically distinct polymer chains (blocks) covalently linked together.[28] This unique feature allows block copolymers to organize into various ordered nanostructures based on the interplay between the blocks' chemical nature, molecular weight, and composition. In this process, the blocks with different chemical properties tend to segregate, driven by their incompatibility, while the covalent linkage ensures the blocks remain connected.

Thermodynamics plays a crucial role in block copolymer self-assembly.[29] The driving force for self-assembly is the reduction in the Gibbs free energy of the system, which arises from the balance between enthalpy and entropy. Enthalpy is governed by the unfavorable interactions between the chemically distinct blocks, while entropy is associated with the conformational freedom of the polymer chains.[30] As the block copolymer system tries to minimize its free energy, the chemically distinct blocks segregate, leading to the formation of nanostructured domains.

The Flory-Huggins interaction parameter (χ) is a key factor in determining the self-assembly behavior of block copolymers. This parameter quantifies the energetic incompatibility between the different blocks. As the value of χ increases, the blocks tend to segregate more and form well-defined domains. However, when the value of χ is too low, the blocks may mix at the molecular level, leading to a disordered state.[31] The balance between the molecular weight of the blocks and the Flory-Huggins interaction parameter is essential in controlling the size and order of the self-assembled domains.

The morphology of the self-assembled nanostructures is dictated by the volume fraction of each block in the copolymer and the interaction between the blocks. Figure 1.3 presents a typical phase diagram that provides a comprehensive guide to understanding the self-assembly behavior and the resulting nanostructures for a given block copolymer system. the composition of the blocks changes, various morphologies can be observed, including lamellar, cylindrical, spherical, and gyroid structures. These morphologies can be predicted based on the phase diagrams of block copolymers, which are constructed by considering the volume fraction of each block and the interaction parameter.[32]

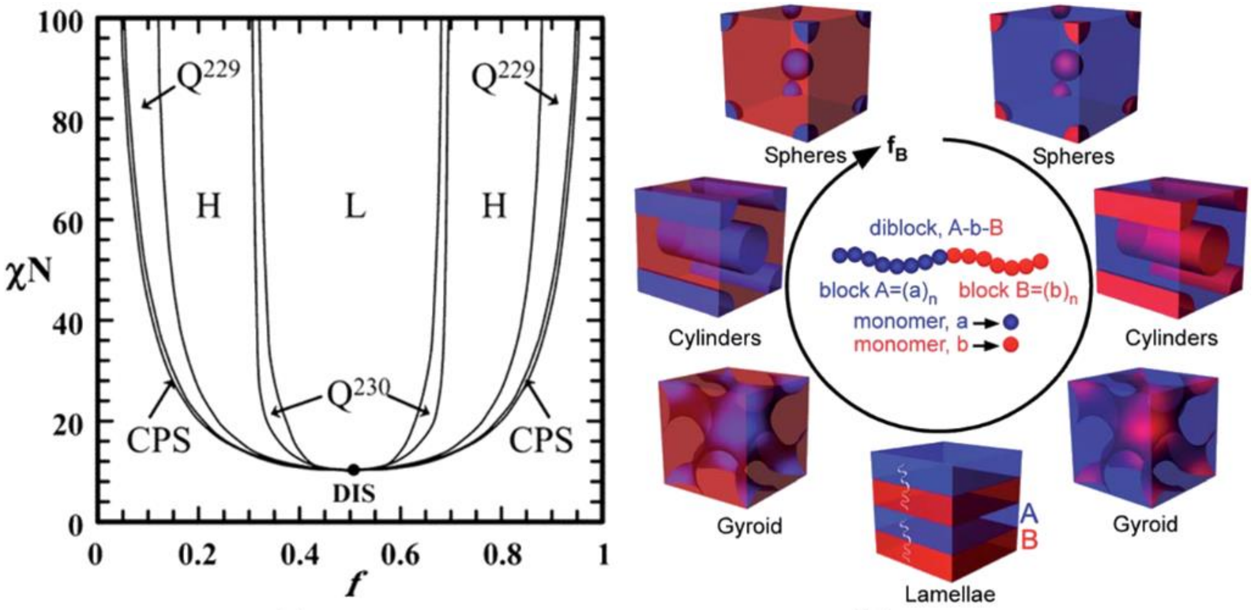

(a) (b)

Figure 1.3 (a) Phase diagram of diblock copolymer predicted by SCMF theory. Reprinted with permission from Cochran et al.33 Copyright (2006) American Chemical Society. (b) Various microdomain organization patterns of a linear AB diblock copolymers. f: volume fraction of one block; χ: Flory–Huggins interaction parameter; N: degree of polymerization; L: lamellae; H: hexagonally packed cylinders; Q230: double-gyroid phase; Q229: body centered spheres; CPS: closed-packed spheres; and DIS: disordered. Reprinted with permission from Hu *et al*.[33] Copyright (2014) The Royal Society of Chemistry.

External factors, such as temperature, solvent, and external fields, can also influence the self-assembly of block copolymers. For example, by controlling the solvent quality during the self-assembly process, one can induce a variety of ordered nanostructures. In some cases, solvent annealing or solvent vapor treatment can be employed to enhance the long-range order of the self-assembled nanostructures. Additionally, the application of external fields, such as electric or magnetic fields, can be used to direct the orientation of the self-assembled domains, providing further control over the nanostructure formation.

1.3.2 Ion transport in block copolymer anion exchange membranes

Ion transport in block copolymer anion exchange membranes (AEMs) is a complex phenomenon that is influenced by a combination of factors, including the polymer's chemical structure, morphology, and the nature of the ion-conducting pathways.[34] Anion exchange membranes typically consist of a hydrophilic phase, which facilitates the transport of anions, and a hydrophobic phase that provides mechanical stability and gas barrier properties.[35] The hydrophilic phase contains fixed cationic groups that facilitate the transport of anions through the membrane via a hopping mechanism.

An important parameter in understanding ion transport in AEMs is the ionic conductivity, which is a measure of the membrane's ability to facilitate ion transport. The ionic conductivity is determined by the number of mobile charge carriers (anions), their mobility, and the dielectric constant of the medium.[36] The overall ionic conductivity of block copolymer AEMs is a result of the combined effects of the hydrophilic and hydrophobic domains, with the hydrophilic domains acting as the primary ion-conducting pathways.

1.3.2.1 Factors affecting ion transport in block copolymer electrolytes

Several factors can influence ion transport in block copolymer AEMs, including the chemical structure of the copolymer, the volume fraction of the hydrophilic phase, the size and distribution of the ion-conducting domains, and the degree of phase separation between the hydrophilic and hydrophobic phases.[37] The chemical structure of the copolymer, including the type and density of ion exchange groups, can impact the ion transport properties by affecting the solvation of anions, ion exchange capacity, and the local environment of the ion-conducting pathways.

The volume fraction of the hydrophilic phase and the size and distribution of the ion-conducting domains are crucial factors that determine the efficiency of ion transport. Higher volume fractions of hydrophilic domains can result in improved ionic conductivity due to the increased availability of ion-conducting pathways. However, excessive swelling of the hydrophilic phase may lead to a loss of mechanical stability and reduced gas barrier properties.[38] The degree of phase separation between the hydrophilic and hydrophobic phases also plays a significant role in ion transport, as it affects the connectivity of the ion-conducting pathways and the tortuosity of the transport routes.[39]

1.3.2.2 Importance of interfaces in ion transport mechanisms

In block copolymer AEMs, the interfaces between the hydrophilic and hydrophobic phases can significantly influence the ion transport mechanisms. The interfacial regions can act as potential barriers or facilitators for ion transport, depending on the degree of compatibility between the hydrophilic and hydrophobic phases and the local environment at the interface. A well-defined interface can improve ion transport by providing continuous and efficient pathways for anions, while a poorly defined interface may lead to increased tortuosity and reduced ionic conductivity. The role of interfaces in ion transport in block copolymer AEMs is an area of ongoing research, and a deeper understanding of the interfacial effects can help guide the design of high-performance anion exchange membranes.

1.3.3 Block copolymer electrolytes thin film measurements

In the field of block copolymer electrolytes (BCEs), characteristics like ionic conductivity and film thickness have typically been evaluated using bulk film, which ranges from 10 to 1000 micrometers thick. Primarily, BCE films are cast and subsequently annealed—undergoing phase separation—before being placed between two plates for subsequent measurements. However, the nanostructure formed by the microphase separation of the block copolymer tends to be on the nanoscale (typically less than 100 nm), determined by factors such as molecular weight and interaction parameters. Consequently, it's anticipated that microphase separated grains will nucleate at disparate locations, leading to a variety of orientations within the resultant film. The presence of defects—such as grain boundaries and conducting pathway dislocations—can significantly affect ion transport properties. To truly examine the intrinsic ion transport properties of BCEs, it's essential to achieve a single-grain structure that eliminates extrinsic factors. A thin film—less than 1 micrometer thick, for example—provides a higher likelihood of achieving a single-grain structure.

The Nealey group has conducted extensive research into the self-assembly of block copolymers in thin film format. Their recent investigations into BCEs in thin films have paved the way for deeper exploration into intrinsic ion transport properties. Kambe et al., for instance, were the first to apply directed self-assembly (DSA) techniques to BCEs studies. They successfully crafted nanostructures that were perpendicularly oriented on a silicon wafer and perfectly aligned with the electric field.[40] Employing a combination of graphoepitaxy (nano trenches made of silicon dioxide) and chemoepitaxy (polymer brushes), they achieved fully connected lamellar structures of polystyrene-block-poly(2-vinlypyridine) (PS-b-P2VP) between the interdigitated electrodes, as depicted in Figure 1.4. By comparing the conductivity across pathways of varying degrees of connection, they accurately quantified the role of defects in influencing ion transport property. Their findings indicated a direct proportionality between ion conductivity, the total number of connected paths between electrodes, and the path length. This research represents a groundbreaking approach to studying structure-property relationships, introducing a novel method for measuring intrinsic properties.

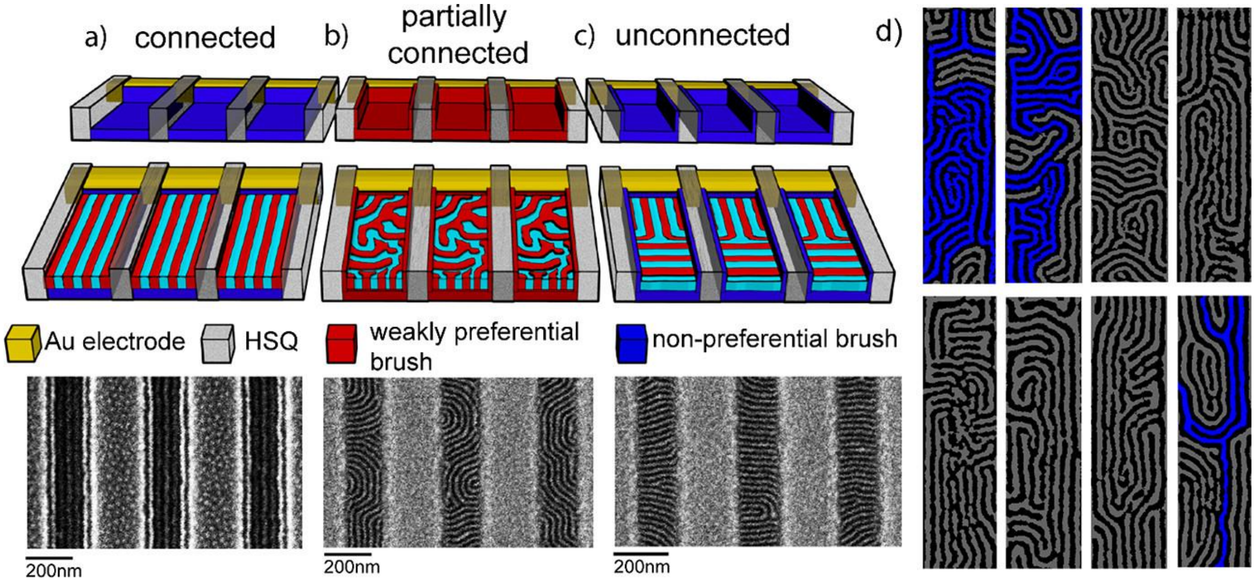

Figure 1.4 Orientation of the PS-*b*-P2VP domains relative to the HSQ guiding stripes and the electrodes that form the individual trenches. Schematic and SEM micrograph of (a) connected, (b) partially, and (c) unconnected structures. (d) Partially connected morphology SEM micrographs after image flattening and path identification where disconnected paths are labeled gray, and the connected domains are labeled blue. Reprinted with permission from Kambe *at al*.[40] Copyright (2019) American Chemical Society.

However, the process of directed self-assembly is highly complex, time-consuming, and dependent on specific materials, which necessitates a more straightforward approach. One potential solution lies in "preferential wetting." When one block of the polymer chain favors the underlying substrate, it rearranges itself during the thermal annealing process to make as much contact with the substrate as possible, thus minimizing free energy. If both blocks exhibit equal surface energy, the lamellar domains will orient perpendicularly, which, without further orientational control, would result in random orientation in the plane parallel to the substrate. Due to its potential to simplify the creation of a single-grain structure, preferential wetting is a favored approach.

Two types of preferential wetting exist: symmetric wetting, where one of the blocks prefers both the substrate and free surface, and asymmetric wetting, where one block prefers the substrate and the other favors the free surface. When the film thickness post spin coating is commensurate, a smooth film with no topography can be observed. However, if the film thickness does not match the periodicity, holes and islands with height differences equivalent to the domain spacing of the BCE will form, as clearly illustrated in Figure 1.5.[33] The Nealey group, with Daniel et al., employed a strategy of parallel lamellae of BCEs, wherein the nanostructure parallel to the substrate forms simply after spin coating and thermal annealing.[41] This methodology enables the intrinsic ionic conductivity measurement of polystyrene-block-polyethylene oxide (PS-b-PEO). By normalizing the conductivity to the volume fraction of the conducting phase and the homopolymer conductivity, they could quantitatively investigate the inactive volume fraction of the PEO block, which they attributed to the interface presence between the blocks. This experimental platform facilitates reliable and quick screening of new materials, as the highest conductivity of the conducting domain can be determined.

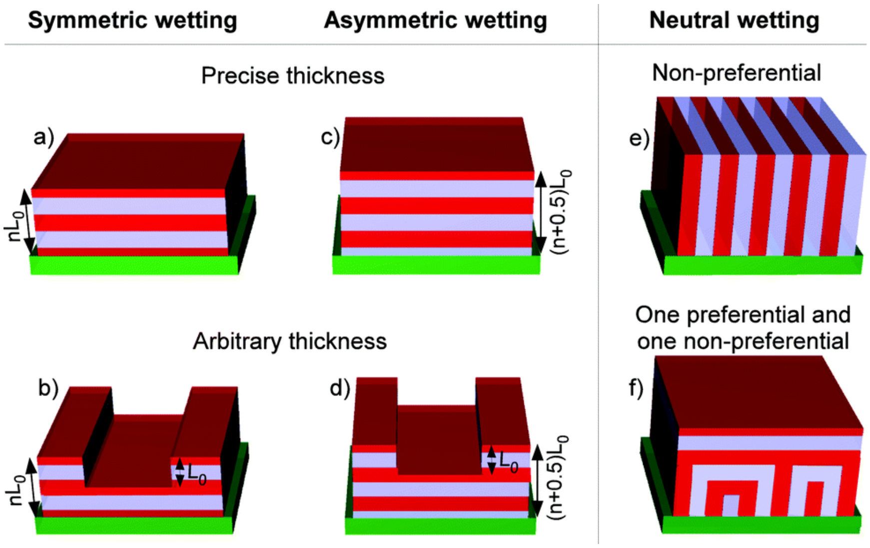

Figure 1.5 Lamellar block copolymer structures assembled onto different wetting and commensurability conditions. Parallel orientations are observed with symmetric (a and b) and asymmetric (c and d) preferential wetting conditions while perpendicular orientations are observed with neutral wetting conditions (e and f). Islands or holes form when the average film thickness is not commensurate with the natural periodicity of the BCP (b and d). Reprinted with permission from Hu *et al*.[33] Copyright (2014) The Royal Society of Chemistry.

1.4 Ion Transport Mechanisms in Hydrated AEMs

Ion transport mechanisms in AEMs are essential for understanding their performance in various applications. The efficiency of ion transport directly impacts the overall performance of these devices, making it crucial to study the factors governing the movement of ions through the membrane. AEMs are typically composed of a polymer matrix containing fixed anionic groups that promote the transport of cations, such as hydroxide ions, across the membrane. Understanding the behavior of these ions within the membrane can help optimize the material's properties and tailor its performance for specific applications.

Various factors influence the ion transport properties of AEMs, including membrane composition, morphology, hydration level, and the size and charge of the ions. These factors can interact and affect the overall efficiency of ion transport in complex ways, making it essential to study the different mechanisms by which ions move through the membrane. A detailed understanding of these mechanisms can provide insights into the structure-property relationships in AEMs and guide the development of new materials with improved ion conductivity, stability, and mechanical properties. Thus, investigating ion transport mechanisms in AEMs is critical for advancing their application in sustainable energy technologies and other related fields.

While the mechanism of anion transport through AEMs is still debated, there is a general consensus that a combination of following mechanisms dictates the ion transport properties as illustrated in Figure 1.6.[42]

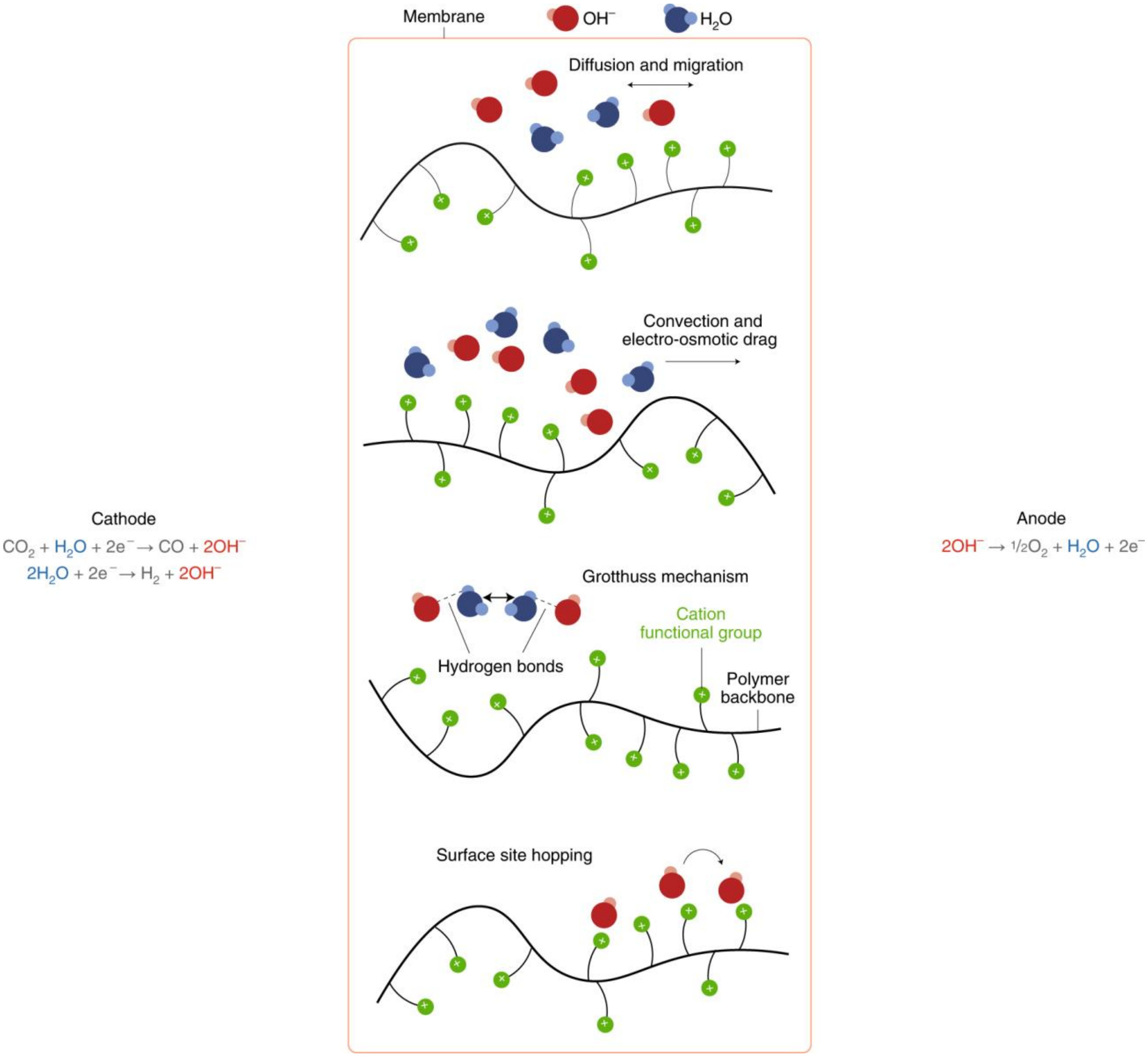

Figure 1.6 Possible combinations of transport mechanisms for anions and water in the AEM. Reprinted with permission from Salvatore *et al*.[42] Copyright (2021) Springer Nature Limited.

1.4.1 Vehicular mechanism

The vehicular mechanism, also known as the vehicle or ion-hopping mechanism, is one of the primary ion transport mechanisms in AEMs.[34] In this mechanism, ions move through the membrane by diffusing within the hydrated polymer matrix, where they are solvated by water molecules forming ion-water clusters. The vehicular mechanism is particularly relevant in AEMs with high water uptake, as the presence of water facilitates the mobility of ions and enhances their conductivity.

Ion solvation by water molecules plays a crucial role in the vehicular mechanism. As ions diffuse through the membrane, they are surrounded by water molecules that form a hydration shell around the ion.[43] This hydration shell assists the movement of the ion by reducing its interaction with the polymer matrix and providing a favorable environment for ion transport. The number of water molecules in the hydration shell and the strength of the ion-water interaction can impact the efficiency of the vehicular mechanism, with a higher hydration level typically resulting in increased ion conductivity.

Several factors influence the vehicular mechanism in AEMs, including the membrane's water uptake capacity, polymer-ion interactions, and the physicochemical properties of the ions themselves. Membranes with higher water uptake generally exhibit more efficient vehicular transport, as increased water content promotes ion solvation and mobility.[23] The chemical structure of the polymer and the presence of functional groups can also impact the vehicular mechanism by affecting the interaction between the polymer matrix and the ions. Additionally, the size and charge of the ions can influence their mobility, with smaller and less charged ions typically experiencing less resistance to movement through the polymer matrix.

1.4.2 Grotthuss hopping

Grotthuss hopping, also known as the Grotthuss mechanism or ion hopping, is another important ion transport mechanism in anion exchange membranes (AEMs). This mechanism involves the rapid transfer of charge through a hydrogen-bonded network of water molecules within the hydrated polymer matrix.[44] In the case of AEMs, the most common ions undergoing Grotthuss hopping are hydroxide ions (OH^-). Grotthuss hopping contributes significantly to the ion conductivity in AEMs, particularly at lower hydration levels, where the vehicular mechanism may be less efficient.

The Grotthuss mechanism relies on the presence of a hydrogen-bonded network of water molecules within the AEM. In this network, the charge transfer occurs via the breaking and forming of hydrogen bonds between adjacent water molecules.[43] For hydroxide ions, this process involves the transfer of a proton from one water molecule to another, resulting in the migration of the hydroxide ion through the hydrogen-bonded network. The efficiency of Grotthuss hopping depends on the continuity and connectivity of the hydrogen-bonded network, which can be influenced by the membrane's hydration level and the organization of hydrophilic and hydrophobic domains within the polymer matrix.

Several factors influence the efficiency of Grotthuss hopping in AEMs, including the membrane's hydration level, the presence of hydrophilic functional groups, and the polymer matrix's nanoscale structure. The Grotthuss mechanism is typically more effective at lower hydration levels, where the hydrogen-bonded network is more continuous and connected.[23] The presence of hydrophilic functional groups in the polymer matrix can help promote the formation and stability of the hydrogen-bonded network, which is essential for efficient Grotthuss hopping. Additionally, the nanoscale structure of the polymer matrix, such as the phase separation between hydrophilic and hydrophobic domains, can impact the connectivity of the hydrogen-bonded network and, consequently, the efficiency of the Grotthuss mechanism.

1.4.3 Surface site hopping

Surface site hopping is also an important ion transport mechanism in AEMs that involves the migration of ions from one site on the polymer to another, typically via the coordination and dissociation of ionic pairs.[42] The polymer chain segmental flexibility plays a crucial role in this process, as it can greatly influence the ability of ions to move between different sites on the polymer matrix. This type of transport mechanism is very similar to that of lithium ions transport in PEO, which is facilitated by segmental motion of the polymer chains. When the hydration level is high, the polymer chain is more flexible due to plasticizing effect, which enables faster ionic hopping between different sites and higher conductivity. On the contrary, ionic transport efficiency would be low if the chain flexibility is low when the hydration level is low. Different from vehicular and Grotthuss mechanism that have been investigated extensively, surface site hopping mechanism in AEMs is far less studied.

1.5 Dissertation Outline

The objective of this dissertation is to explore the ion transport mechanism in anion exchange membranes. The need for materials that are both mechanically robust and ionically conductive has led to the strategy of crosslinking and using block copolymers.

Chapter 2 presents several key experimental techniques that deviate from those conventionally used in the AEM research community, along with a discussion of their fundamentals. Since all the work in this dissertation was conducted in thin film format, different characterization tools were required. The film thickness as a function of relative humidity was measured within a liquid cell on an ellipsometer under controlled relative humidity. The water uptake of the functionalized thin film was assessed using a quartz crystal microbalance (QCM). Most significantly, we used the customized interdigitated electrodes (IDEs) to measure thin film conductivity in a nanofabrication facility. This combination of techniques offers the AEM community further opportunities to investigate material properties.

Chapter 3 presents a study on ion transport behavior in crosslinked anion exchange polymer electrolytes. By systematically controlling the degree of crosslinking through manipulating the molar percentage of 4-vinylbenzocyclobutene (BCB) in P(2VP-co-BCB), we elucidate the relationship between water content, segmental dynamics of the polymer chain, and ionic conductivity. The combination of thin film characterization tools we developed provides a fresh perspective for understanding ion transport phenomena.

In Chapter 4, we delve into the ion transport mechanism in block copolymer electrolytes, specifically poly(styrene-block-2 vinyl pyridine) (PS-b-P2VP). Engineering the substrate with a coating of crosslinked PS mat allowed us to achieve parallel lamellae. Measuring the conductivity in the single-grain structure helped isolate extrinsic factors like defects and grain boundaries. We further revealed the role of the interface in affecting ion transport. Hard x-ray reflectivity was employed to probe the presence and thickness of the interface. Additionally, Molecular Dynamic simulations were conducted to help explain the differential water absorption behavior among various block copolymer electrolytes.

Chapter 5 concludes the results of this work and discusses potential future directions following this research.

1.6 References

1. Merle, G., Wessling, M. & Nijmeijer, K. Anion exchange membranes for alkaline fuel cells: A review. *J. Memb. Sci.* **377**, 1–35 (2011).

2. Varcoe, J. R. *et al.* Anion-exchange membranes in electrochemical energy systems. *Energy Environ. Sci.* **7**, 3135–3191 (2014).

3. Li, N., Leng, Y., Hickner, M. A. & Wang, C.-Y. Highly Stable, Anion Conductive, Comb-Shaped Copolymers for Alkaline Fuel Cells. *J. Am. Chem. Soc.* **135**, 10124–10133 (2013).

4. Maurya, S., Shin, S.-H., Kim, Y. & Moon, S.-H. A review on recent developments of anion exchange membranes for fuel cells and redox flow batteries. *RSC Adv.* **5**, 37206–37230 (2015).

5. Porada, S., Zhao, R., van der Wal, A., Presser, V. & Biesheuvel, P. M. Review on the science and technology of water desalination by capacitive deionization. *Prog. Mater. Sci.* **58**, 1388–1442 (2013).

6. Weber, A. Z. *et al.* Redox flow batteries: a review. *J. Appl. Electrochem.* **41**, 1137–1164 (2011).

7. Carmo, M., Fritz, D. L., Mergel, J. & Stolten, D. A comprehensive review on PEM water electrolysis. *Int. J. Hydrogen Energy* **38**, 4901–4934 (2013).

8. Lewis, N. S. & Nocera, D. G. Powering the planet: Chemical challenges in solar energy utilization. *Proc. Natl. Acad. Sci.* **103**, 15729–15735 (2006).

9. Truong, V. M., Duong, N. B., Wang, C.-L. & Yang, H. Effects of Cell Temperature and Reactant Humidification on Anion Exchange Membrane Fuel Cells. *Materials* **12**, (2019).

10. Hickner, M. A., Herring, A. M. & Coughlin, E. B. Anion exchange membranes: Current status and moving forward. *J. Polym. Sci. Part B Polym. Phys.* **51**, 1727–1735 (2013).

11. Dekel, D. R. Review of cell performance in anion exchange membrane fuel cells. *J. Power Sources* **375**, 158–169 (2018).

12. Gottesfeld, S. *et al.* Anion exchange membrane fuel cells: Current status and remaining challenges. *J. Power Sources* **375**, 170–184 (2018).

13. Sui, S. *et al.* A comprehensive review of Pt electrocatalysts for the oxygen reduction reaction: Nanostructure{,} activity{,} mechanism and carbon support in PEM fuel cells. *J. Mater. Chem. A* **5**, 1808–1825 (2017).

14. Omasta, T. J. *et al.* Importance of balancing membrane and electrode water in anion exchange membrane fuel cells. *J. Power Sources* **375**, 205–213 (2018).

15. Ahmed, M. & Dincer, I. A review on methanol crossover in direct methanol fuel cells: challenges and achievements. *Int. J. Energy Res.* **35**, 1213–1228 (2011).

16. Kwon, S., Rao, A. H. N. & Kim, T.-H. Anion exchange membranes based on terminally crosslinked methyl morpholinium-functionalized poly(arylene ether sulfone)s. *J. Power Sources* **375**, 421–432 (2018).

17. Ren, X., Price, S. C., Jackson, A. C., Pomerantz, N. & Beyer, F. L. Highly Conductive Anion Exchange Membrane for High Power Density Fuel-Cell Performance. *ACS Appl. Mater. Interfaces* **6**, 13330–13333 (2014).

18. Xue, J., Liu, L., Liao, J., Shen, Y. & Li, N. Semi-interpenetrating polymer networks by azide–alkyne cycloaddition as novel anion exchange membranes. *J. Mater. Chem. A* **6**, 11317–11326 (2018).

19. Xu, F., Su, Y. & Lin, B. Progress of Alkaline Anion Exchange Membranes for Fuel Cells: The Effects of Micro-Phase Separation. *Front. Mater.* **7**, (2020).

20. Hao, J. *et al.* Crosslinked high-performance anion exchange membranes based on poly(styrene-b-(ethylene-co-butylene)-b-styrene). *J. Memb. Sci.* **551**, 66–75 (2018).

21. Yang, Y. *et al.* Anion-exchange membrane water electrolyzers and fuel cells. *Chem. Soc. Rev.* **51**, 9620–9693 (2022).

22. Hu, C. *et al.* Multi-cation crosslinked anion exchange membranes from microporous Tröger's base copolymers. *J. Mater. Chem. A* **6**, 13302–13311 (2018).

23. Park, C. H., Lee, C. H., Guiver, M. D. & Lee, Y. M. Sulfonated hydrocarbon membranes for medium-temperature and low-humidity proton exchange membrane fuel cells (PEMFCs). *Prog. Polym. Sci.* **36**, 1443–1498 (2011).

24. Zhang, K. *et al.* Bent-twisted block copolymer anion exchange membrane with improved conductivity. *J. Memb. Sci.* **550**, 59–71 (2018).

25. Li, Y. *et al.* Polyethylene-Based Block Copolymers for Anion Exchange Membranes. *Macromolecules* **48**, 6523–6533 (2015).

26. Selhorst, R. *et al.* Multiblock Copolymer Anion-Exchange Membranes Derived from Vinyl Addition Polynorbornenes. *ACS Appl. Energy Mater.* **4**, 10273–10279 (2021).

27. Trant, C., Hwang, S., Bae, C. & Lee, S. Synthesis and Characterization of Anion-Exchange Membranes Using Semicrystalline Triblock Copolymers in Ordered and Disordered States. *Macromolecules* **53**, 8548–8561 (2020).

28. Bates, F. S. & Fredrickson, G. H. Block Copolymers—Designer Soft Materials. *Phys. Today* **52**, 32–38 (1999).

29. Leibler, L. Theory of Microphase Separation in Block Copolymers. *Macromolecules* **13**, 1602–1617 (1980).

30. Matsen, M. W. & Bates, F. S. Unifying Weak- and Strong-Segregation Block Copolymer Theories. *Macromolecules* **29**, 1091–1098 (1996).

31. Huggins, M. L. Some Properties of Solutions of Long-chain Compounds. *J. Phys. Chem.* **46**, 151–158 (1942).

32. Fredrickson, G. H. & Bates, F. S. Dynamics of Block Copolymers: Theory and Experiment. *Annu. Rev. Mater. Sci.* **26**, 501–550 (1996).

33. Hu, H., Gopinadhan, M. & Osuji, C. O. Directed self-assembly of block copolymers: a tutorial review of strategies for enabling nanotechnology with soft matter. *Soft Matter* **10**, 3867–3889 (2014).

34. Hickner, M. A., Ghassemi, H., Kim, Y. S., Einsla, B. R. & McGrath, J. E. Alternative Polymer Systems for Proton Exchange Membranes (PEMs). *Chem. Rev.* **104**, 4587–4612 (2004).

35. Varcoe, J. R. & Slade, R. C. T. Prospects for Alkaline Anion-Exchange Membranes in Low Temperature Fuel Cells. *Fuel Cells* **5**, 187–200 (2005).

36. Geise, G. M., Hickner, M. A. & Logan, B. E. Ionic Resistance and Permselectivity Tradeoffs in Anion Exchange Membranes. *ACS Appl. Mater. Interfaces* **5**, 10294–10301 (2013).

37. Young, W.-S., Kuan, W.-F. & Epps Thomas H., I. I. I. Block copolymer electrolytes for rechargeable lithium batteries. *J. Polym. Sci. Part B Polym. Phys.* **52**, 1–16 (2014).

38. Li, N. & Guiver, M. D. Ion Transport by Nanochannels in Ion-Containing Aromatic Copolymers. *Macromolecules* **47**, 2175–2198 (2014).

39. Chen, H., Tao, R., Bang, K.-T., Shao, M. & Kim, Y. Anion Exchange Membranes for Fuel Cells: State-of-the-Art and Perspectives. *Adv. Energy Mater.* **12**, 2200934 (2022).

40. Kambe, Y. *et al.* Role of Defects in Ion Transport in Block Copolymer Electrolytes. *Nano Lett.* **19**, 4684–4691 (2019).

41. Sharon, D. *et al.* Intrinsic Ion Transport Properties of Block Copolymer Electrolytes. *ACS Nano* **14**, 8902–8914 (2020).

42. Salvatore, D. A. *et al.* Designing anion exchange membranes for CO2 electrolysers. *Nat. Energy* **6**, 339–348 (2021).

43. Kreuer, K.-D. Proton Conductivity: Materials and Applications. *Chem. Mater.* **8**, 610–641 (1996).

44. Agmon, N. The Grotthuss mechanism. *Chem. Phys. Lett.* **244**, 456–462 (1995).

CHAPTER 2

EXPERIMENTAL TECHNIQUES AND FUNDAMENTALS

2.1 AC Electrochemical Impedance Spectroscopy

Electrochemical impedance spectroscopy, or EIS, is an invaluable and non-invasive method used to examine the properties and behavior of numerous electrochemical systems, encompassing areas such as batteries, fuel cells, corrosion studies, sensors, and electrochemical materials. By applying a minor sinusoidal voltage or current perturbation to the system and analyzing the resulting response in terms of frequency, EIS offers insights into the kinetics and transport processes involved in electrochemical reactions. This knowledge, in turn, enables the evaluation and enhancement of the performance of various electrochemical devices and materials.

EIS plays a pivotal role in our understanding of electrochemical systems as it offers intricate details about the different processes that occur at the electrode-electrolyte interface, as well as within the materials themselves. By exploring the frequency-dependent response of an electrochemical system, EIS allows for the isolation and examination of individual processes, such as charge transfer, mass transport, and adsorption/desorption. This information proves essential for the development of new materials, optimization of electrochemical devices, and the identification of performance-related issues in existing systems. Moreover, the applicability of EIS across a broad range of electrochemical systems and under various experimental conditions renders it a highly versatile tool in the field of electrochemistry.

2.1.1 Basics of impedance

2.1.1.1 Definition and properties

Impedance (Z) is a fundamental concept in electrical and electrochemical systems. It is a complex quantity that quantifies the opposition a circuit element presents to the flow of alternating current (AC). Impedance is a generalization of the concept of resistance (R) to include the effects of capacitance (C) and inductance (L). The impedance of a circuit element can be represented as a complex number:

$$Z = R + jX \tag{2.1}$$

where R is the real part, known as the resistance, and X is the imaginary part, known as the reactance. The reactance term (jX) can be either positive or negative, depending on whether the circuit element is inductive (positive) or capacitive (negative). The unit of impedance is ohms (Ω).

2.1.1.2 Complex impedance

The complex impedance can be further analyzed in terms of its magnitude (|Z|) and phase angle (θ). The magnitude of the impedance represents the total opposition to the flow of AC, while the phase angle indicates the phase shift between the voltage and current waveforms as shown in Figure 2.1. These quantities can be calculated as follows:

$$|Z| = \surd(R^2 + X^2) \tag{2.2}$$

$$\theta = \arctan\,(X/R) \tag{2.3}$$

In the context of EIS, the impedance of an electrochemical system is frequency dependent. At a specific frequency (ω), the impedance of a resistor, capacitor, and inductor can be expressed as:

$Z_R = R$ (resistor)

$Z_C = -j/(\omega\ C)$ (capacitor)

$Z_L = j\ \omega\ L$ (inductor)

where ω is the angular frequency (ω = 2πf) and f is the frequency in hertz (Hz).

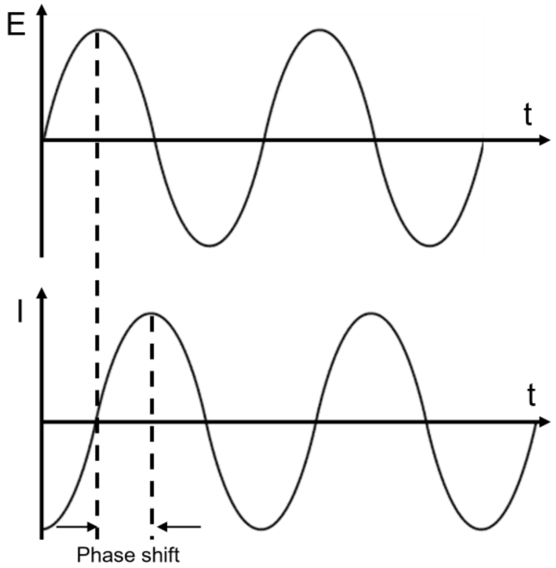

Figure 2.1 Sinusoidal Current Response in a Linear System

2.1.1.3 Impedance in electrical circuits

In electrical circuits, the impedance of individual components such as resistors, capacitors, and inductors can be combined to find the overall impedance of the circuit. The method of combination depends on the arrangement of the components in the circuit, which can be either in series or parallel. When circuit elements are connected in series, their impedances are added directly. For example, if a resistor (Z_R), capacitor (Z_C), and inductor (Z_L) are connected in series, the total impedance (Z_{total}) of the circuit would be:

$$Z_{total} = Z_R + Z_C + Z_L \tag{2.4}$$

In the case of parallel connections, the reciprocal of the total impedance is equal to the sum of the reciprocals of the individual impedances. For a resistor (Z_R), capacitor (Z_C), and inductor(Z_L) connected in parallel, the total impedance (Z_{total}) would be:

$$1/Z_{total} = 1/Z_R + 1/Z_C + 1/Z_L \tag{2.5}$$

In some cases, circuits may have more complex arrangements of components, such as combinations of series and parallel connections or even more complicated network topologies. In these situations, techniques such as Kirchhoff's laws, mesh analysis, or nodal analysis can be employed to find the overall impedance of the circuit.

2.1.2 AC electrochemical impedance spectroscopy principles

2.1.2.1 AC voltage and current in electrochemical systems

In AC electrochemical impedance spectroscopy, a small sinusoidal voltage (V) or current (I) perturbation is applied to the electrochemical system, and the resulting current or voltage response is measured. The perturbation can be expressed mathematically as:

$$V(t) = V_0 * \sin{(\omega t + \varphi_V)} \tag{2.6}$$

or

$$I(t) = I_0 * \sin{(\omega t + \varphi_I)} \tag{2.7}$$

where V_0 and I_0 are the amplitudes of the voltage and current perturbations, respectively, ω is the angular frequency ($\omega = 2\pi f$), t is time, and φ_V and φ_I are the phase shifts of the voltage and current waveforms, respectively.

The impedance of the electrochemical system can be calculated by relating the applied perturbation (voltage or current) to the measured response (current or voltage) and considering the phase shift between the two signals. The complex impedance (Z) is given by the ratio of the complex voltage (V) to the complex current (I):

$$Z = V / I \tag{2.8}$$

2.1.2.2 Frequency response

One of the key aspects of electrochemical impedance spectroscopy is its frequency-dependent nature. By sweeping through a range of frequencies, EIS can provide detailed information about the various processes occurring within the electrochemical system. Typically, high frequencies are associated with processes that occur on short time scales, such as double-layer charging, while low frequencies correspond to processes with longer time scales, such as diffusion and mass transport.

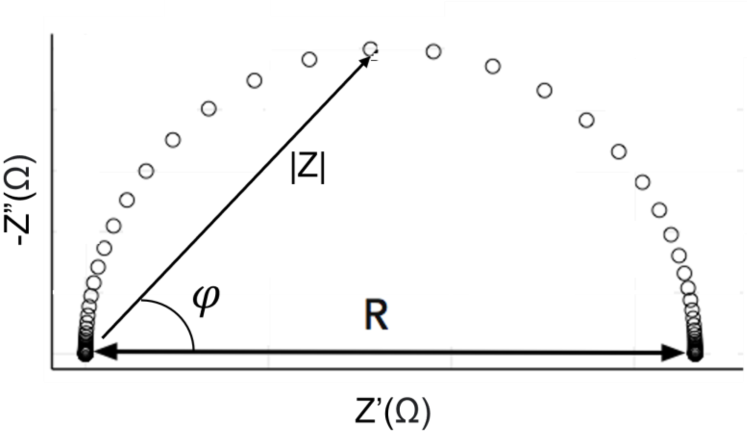

Figure 2.2 Example of Nyquist plot

The frequency response of an electrochemical system is often represented using complex plane plots (Nyquist plots) and Bode plots as illustrated in Figure 2.2 and Figure 2.3, respectively. These graphical representations help to visualize the impedance characteristics of the system at different frequencies and can be used to identify and analyze the contributions of individual electrochemical processes. In Figure 2.2, each point is collected at different frequencies, going up from right to left and impedance can be represented as a vector with a magnitude of |Z| . The degree of phase shift can be derived from the angle between the vector and the X-axis. In Figure 2.3, both the magnitude of impedance and phase shift angle as a function of frequency are presented. This is just a different way of expressing the same information as Nyquist plot. When the frequency of the current decreases from a very high number, the observed impedance firstly remains constantly low and phase shift angle remains 90-degree. During this period, the material is more capacitor-like. At certain frequency, impedance starts to increase, with phase shift angle decreasing, indicating a combination of capacitor and resistor. Finally, when the frequency decreases to a certain point, where both the impedance and phase shift angle would remain constant, a resistor-like state of the material is achieved. The resistance of the material can thus be obtained from the Bode plot.

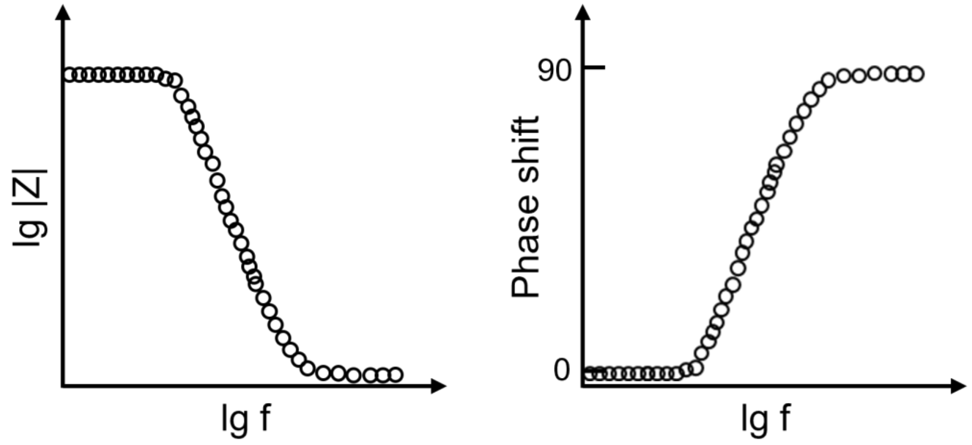

Figure 2.3 Bode plot corresponding to the Nyquist plot in Figure 2.2

2.1.2.3 Linear response theory

The linear response theory is a fundamental assumption in electrochemical impedance spectroscopy. This theory asserts that the response of an electrochemical system to a small perturbation is linearly proportional to the perturbation itself. In other words, the response of the system should be linear with respect to the amplitude of the applied voltage or current. This is crucial for the validity of EIS measurements and the interpretation of the resulting data.

To ensure that the system operates within the linear regime, it is important to use small perturbation amplitudes (typically in the range of 5-10 mV for voltage perturbations and a corresponding range for current perturbations). Figure 2.4 shows the linear response of current to voltage when the perturbation amplitude is small. For all the EIS measurements in this work, we chose 10 mV, which gives decent single to noise ratio. Larger perturbations may lead to non-linear behavior, which can result in inaccurate or misleading impedance data.

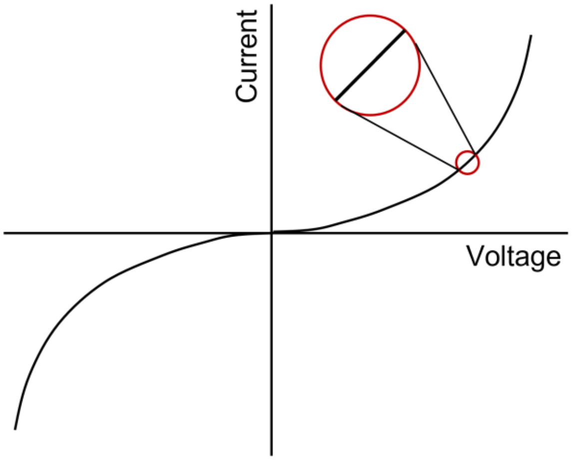

Figure 2.4 Current-voltage relationship in electrochemical system. Inset shows the linearity of a small voltage range.

2.1.2.4 Kramers-Kronig relations

The Kramers-Kronig (KK) relations are a set of mathematical transformations that link the real and imaginary parts of a complex function, such as the impedance in electrochemical impedance spectroscopy. These relations are derived from the principle of causality, which states that the response of a system at a given time cannot be influenced by events occurring in the future. In the context of EIS, this means that the impedance at a specific frequency must be related to the impedance at all other frequencies in a causal manner.

The KK relations can be used to verify the validity and consistency of EIS data. By calculating the expected imaginary part of the impedance from the measured real part (or vice versa) using the KK relations, it is possible to check if the EIS data satisfy the principle of causality. If the measured and calculated imaginary parts match within a reasonable degree of accuracy, it can be concluded that the EIS data are valid and consistent. However, if significant discrepancies are observed, it may indicate issues with the experimental setup, the presence of artifacts, or the violation of the linear response theory.

It is important to note that while the KK relations can be used to validate EIS data, they cannot be used to determine the specific processes or mechanisms occurring within the electrochemical system. To extract this information, EIS data must be analyzed using equivalent circuit models, mathematical fitting techniques, and other complementary electrochemical methods.

2.1.3 Data analysis and interpretation

Equivalent circuit modeling is a widely used method for analyzing and interpreting electrochemical impedance spectroscopy data. This approach involves fitting the experimental impedance data to an electrical circuit model that represents the electrochemical processes occurring within the system. The circuit model is composed of electrical components such as resistors, capacitors, and inductors, which are arranged in a manner that mimics the behavior of the electrochemical system under investigation.

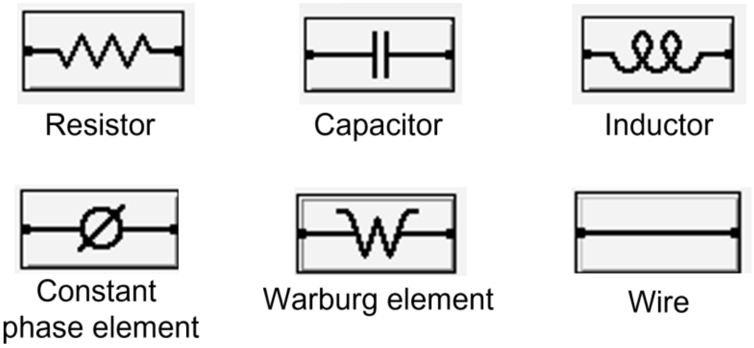

Figure 2.5 Symbols of general circuit elements used in electrochemical systems

The selection of an appropriate equivalent circuit model is crucial for obtaining accurate and meaningful information about the electrochemical system. This process often requires a combination of theoretical understanding of the system, experimental observations, and trial-and-error fitting. Some common equivalent circuit elements used in electrochemical systems include: *Resistors (R)*: Representing ohmic resistances, charge transfer resistances, or other resistive processes. *Capacitors (C)*: Representing double-layer capacitance or other capacitive behavior. *Constant phase elements (CPE)*: Representing non-ideal capacitive behavior often observed in real electrochemical systems due to surface roughness, inhomogeneity, or other factors. *Inductors (L)*: Representing inductive behavior, which may be present in some electrochemical systems, although less common than resistive and capacitive elements. *Warburg impedance (W)*: Representing semi-infinite linear diffusion in electrochemical systems.

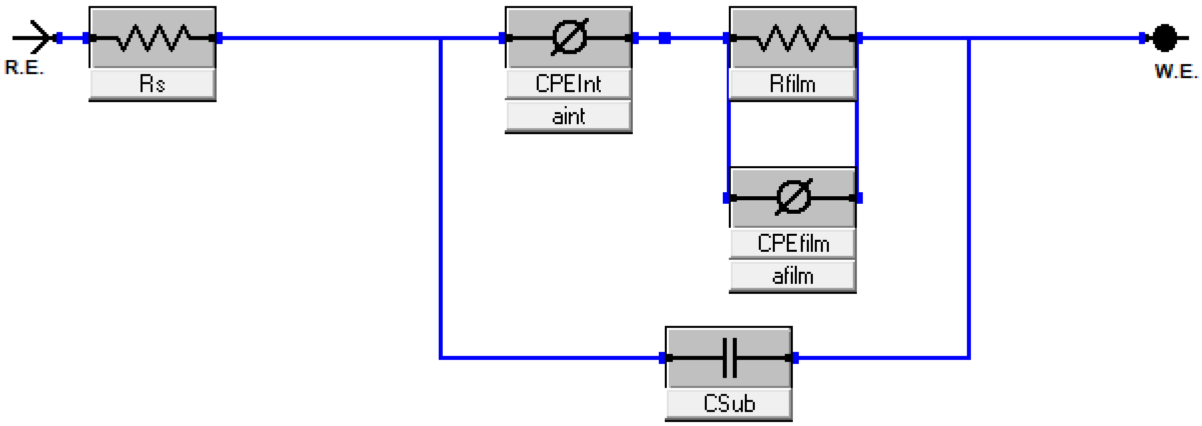

Figure 2.6 Equivalent circuit model used for the electrochemical system in this work

By fitting the experimental data to the selected equivalent circuit model, it is possible to extract quantitative information about the various processes occurring within the system, such as charge transfer resistances, double-layer capacitances, and diffusion coefficients. Figure 2.6 displays the equivalent circuit model that is used for the electrochemical system in this work.

2.2 Interdigitated Electrodes (IDEs) for Thin Film Impedance Measurements

Conventionally, the impedance of a polymer electrolyte membrane is measured in a bulk membrane format (10-1000 μm in thickness) clamped between two electrodes. However, in this work, we predominantly measure material properties such as water uptake and volume expansion in a thin film format. Consequently, a platform for thin film impedance measurement is necessary. The Nealey group has exerted considerable effort to optimize the fabrication process and geometry of interdigitated electrodes (IDEs), emerging as a robust tool to investigate the ion transport properties of thin film polymer electrolytes. In this section, we will detail the fabrication process of the IDEs and discuss some fundamental aspects.

2.2.1 Microfabrication processes of IDEs

The fabrication of IDEs employs various tools from the semiconductor industry, including photolithography, metal deposition, thin film growth, and more. The Pritzker Nanofabrication Facility (PNF) at UChicago enables us to fabricate these customized IDEs. The fabrication process, illustrated briefly in Figure 2.7, entails several steps:

1. *HMDS prime on the wafer*

A fresh wafer with 1 μm thermal oxide on the surface was cleaned using a nitrogen gun to remove any particles. The wafer was then placed on a glass holder and transferred into the HMDS (hexamethyldisilazane) oven chamber. Here, a thin layer of HMDS is coated on the wafer surface following a programmed sequence. This step enhances the adhesion of the photoresist to the substrate and is vital for successful pattern writing.

2. *Photoresist preparation on the substrate*

Approximately 8 µL of photoresist (stored at room temperature for 30 minutes after refrigeration) was gently dropped onto the wafer to minimize bubble formation. The stage was then programmed to run at 4000 rpm with an acceleration of 4000 rpm/s for 1 minute, yielding a uniform resist film of about 1.7 µm. The coated wafer was subsequently transferred to a hotplate set at 110 °C for 1 minute to solidify the resist layer by evaporating solvent residue, a crucial step for the subsequent lithography.

3. *Photolithography*

The lithography step was performed on the Heidelberg MLA150 Direct Write Lithographer tools in the PNF. The direct writing capability of the tool provides great flexibility in creating IDE patterns to meet specific needs. The baked substrate was placed under the writing head and secured by a moderate vacuum. A laser with a wavelength of 375 nm was selected, with a 290 µC/cm2 dose for optimal resolution. The resist is a negative resist, so the exposed area crosslinks and becomes insoluble. The exposure consists of approximately 700 writing steps over a total time of roughly 15 minutes. The exposed substrate was then baked again on a hotplate to assist the crosslinking of the exposed area, which is crucial for pattern transfer.

4. *Development of the pattern*

The baked substrate was transferred to a dish filled with approximately 200 mL of aqueous developer (AZ MIF 300). The solution was slightly agitated every 20 seconds to ensure no resist residue remained on the surface. This process takes about 1 minute. Development was halted by rinsing with DI water for another 90 seconds. A clean, intact pattern is critical for the subsequent metal deposition, which creates the IDEs.

5. *Metal deposition*

All metal deposition for IDEs in this work was done using an e-beam evaporation tool in the PNF. We chose platinum as the electrode material for its inertness to the iodide ions in the polymer electrolytes and its overall stability. Before depositing the desired materials onto the substrate, a thin adhesion layer (5 nm, typically titanium) was deposited for better quality, followed by 45 nm of metal deposition. The steps can be programmed to control the materials, deposition rate, time, and recipe for the deposition. The deposition occurs in a high vacuum environment with a maximum pressure of 1 ×10−6 torr.

6. Lift off

In this step, the unwanted parts - the photoresist and the metal deposited on top - are removed. A clean and efficient process in this step ensures the good quality of the final IDEs. The wafer was placed face-down in a dish filled with sufficient NMP at 80 °C. It was left in the hot bath for at least 6 hours to allow complete removal of the resist on the substrate. It's important to note that NMP does not dissolve the resist as it is crosslinked. The entire resist film is actually delaminated from the substrate. After several hours of soaking in NMP, the wafer was removed and rinsed with fresh NMP, followed by acetone, IPA, and DI water to fully remove any residues. The resulting wafer was then checked under an optical microscope to ensure each device was perfect. Finally, the devices were cleaned with oxygen plasma to ensure a hydrophilic surface.

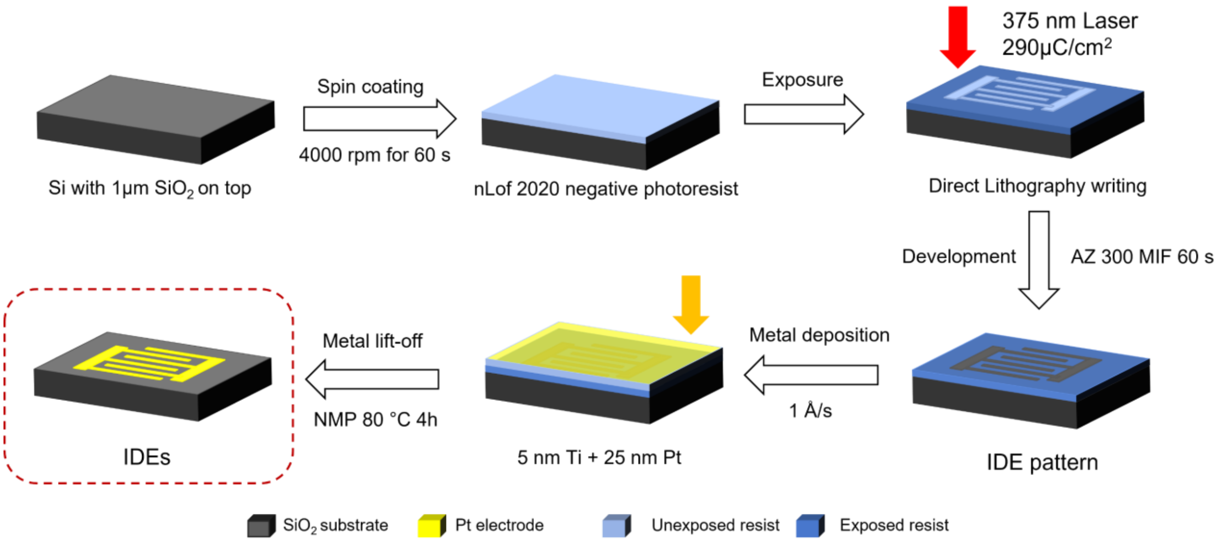

Figure 2.7 Process flow diagram for the fabrication of interdigitated electrodes

2.2.2 Impedance measurement using IDEs

The conductivity of polymer electrolytes throughout this work is derived from resistance measurements via Electrochemical Impedance Spectroscopy (EIS). Thus, understanding the relationship between these two parameters is crucial. Our group has conducted extensive research to determine the cell constant of IDEs. In Figure 2.8, various parameters of thin films deposited on IDEs are shown: 'l' represents the overlapping length of the teeth, 'd' is the separation distance between teeth, 'w' denotes the width of the teeth, 'h' is the height of the thin film, and 'N' is the total number of teeth. The conductivity can be simply calculated using the following equation:

$$\sigma = \frac{d}{R(N-1)lh} \tag{2.9}$$

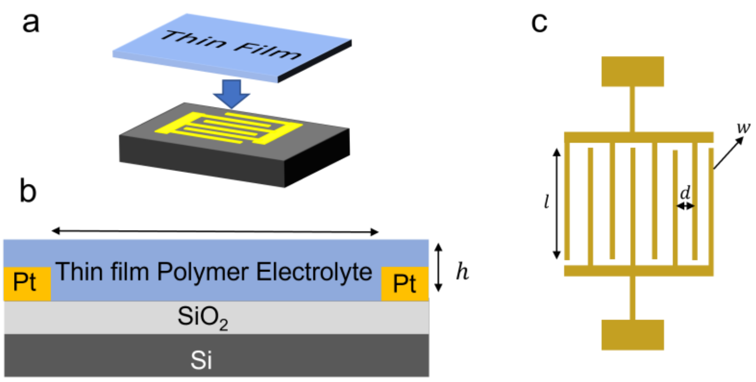

Figure 2.8 (a) Deposition of thin film polymer electrolytes on top of IDEs. (b) Diagram for the cross-section of polymer electrolytes coated IDEs. (c) Top-down view of the IDEs geometry.

The conductivity value derived from IDEs was compared to values obtained from bulk membrane measurements using conventional methods, and the results were found to be very similar. Additionally, the high reproducibility of the measurements boosts our confidence in using this new platform to probe thin film conductivity. As shown in Figure 2.9, the Nyquist plot and Bode plot from the EIS measurement demonstrate a high signal-to-noise ratio, with the resistance readily derived from the extrapolation of the right side of the semicircle to the X-axis in the Nyquist plot.

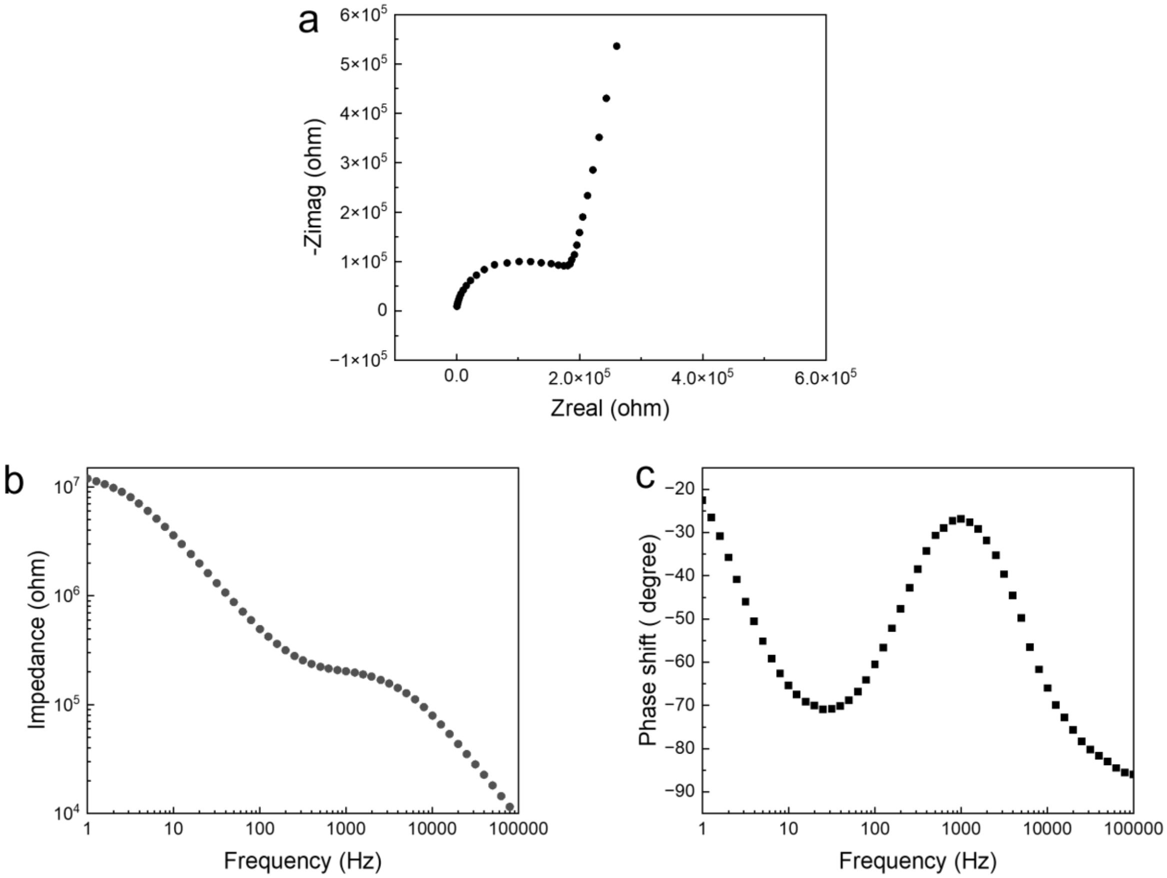

Figure 2.9 Example of EIS measurement curve of polymer electrolytes on IDEs: (a) Nyquist plot, (b)(c) Bode plot regarding impedance and phase shift as a function of frequency, respectively.

2.3 Ellipsometer Coupled with Controlled Relative Humidity

The thickness variation of polymer electrolytes, such as AEMs, is a significant parameter that can influence the overall performance of fuel cell devices. Conventionally, the thickness of bulk AEMs is measured using a micrometer, a method not suitable for thin film measurements. Traditional approaches for measuring the thickness of polymer thin films, like profilometry and atomic force microscopy (AFM), can be invasive or may lack the sensitivity required for real-time, in situ monitoring. To address this, we have developed a sophisticated experimental setup that integrates ellipsometry with a liquid cell and a relative humidity generator. This combination presents several benefits for the precise measurement of polymer thin film thickness as a function of relative humidity:

1. *Non-destructive and non-invasive*: Ellipsometry is an optical technique that measures the change in polarization state of light reflected from a thin film surface. This allows for non-destructive and non-invasive measurements, preserving the integrity of the film and avoiding potential damage or contamination.
2. *Real-time, in situ monitoring*: The use of a liquid cell and relative humidity generator enables real-time control and monitoring of the humidity environment. This makes it possible to study the dynamic response of the polymer thin film to changes in relative humidity.
3. *High sensitivity and accuracy*: Ellipsometry is known for its high sensitivity, capable of detecting sub-nanometer changes in film thickness. This allows for precise measurement of polymer thin film swelling or shrinking in response to variations in relative humidity.
4. *Versatility*: The setup can be adapted to study a wide range of polymer thin films, offering flexibility in terms of sample type and environmental conditions.

2.3.1 Main components of the setup

The experimental setup consists of the following main components: an ellipsometer, a liquid cell, and a relative humidity generator as illustrated in Figure 2.10.

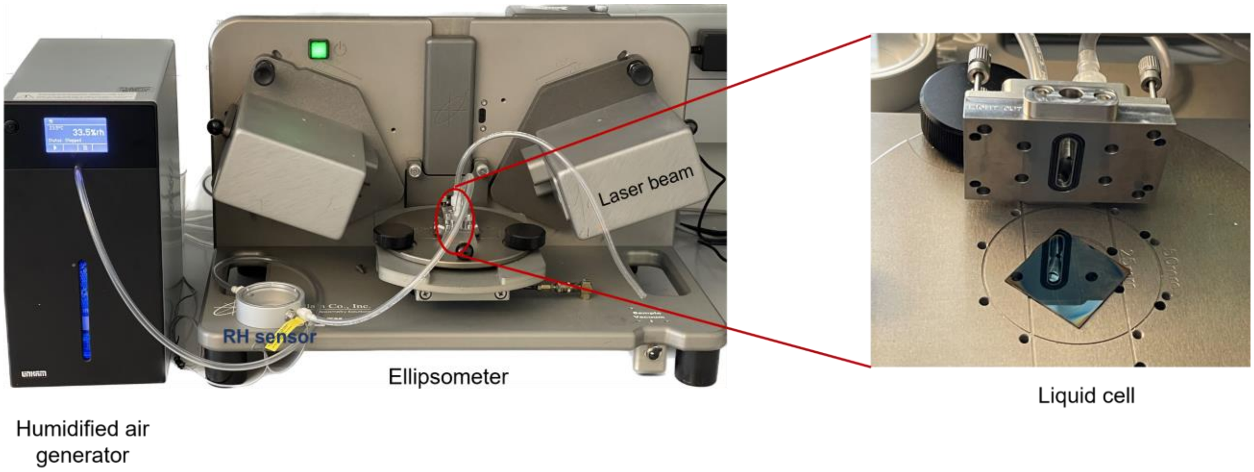

Figure 2.10 Experimental apparatus of thin film thickness measurement in controlled humidity environment via ellipsometry coupled with liquid cell and relative humidity generator.

Ellipsometer: A spectroscopic ellipsometer is employed to measure the thickness of the polymer thin film. It operates by sending polarized light towards the sample and analyzing the change in polarization state upon reflection. The acquired data is then fitted to a suitable optical model, which provides the thickness and optical properties of the film.

Liquid Cell: The liquid cell is designed to hold the polymer thin film sample while allowing for controlled exposure to different humidity environments. It features a transparent window, which enables the ellipsometer to access the sample and perform measurements. The cell is connected to the relative humidity generator via inlet and outlet tubes.

Relative Humidity Generator: The relative humidity generator is responsible for controlling the humidity conditions within the liquid cell. It produces a gas mixture containing a known ratio of water vapor and dry gas, typically nitrogen or air. The gas mixture is then directed into the liquid cell to establish the desired humidity environment. Humidity levels can be adjusted by varying the flow rates of water vapor and dry gas, enabling the study of a wide range of humidity conditions.

2.3.2 Steps for measurements

1. Calibration and baseline measurements are performed on the ellipsometer to ensure accurate and reproducible results.
2. The polymer thin film sample is prepared and placed within the liquid cell. The cell is then sealed, and the inlet and outlet tubes are connected to the relative humidity generator.
3. The desired humidity conditions are established within the liquid cell by adjusting the flow rates of water vapor and dry gas.
4. In situ ellipsometry measurements are carried out as the relative humidity is varied. The acquired data is analyzed to extract the thickness of the polymer thin film.
5. The experiment is repeated for different humidity conditions to generate a complete profile of the polymer thin film thickness as a function of relative humidity

2.4 Thin Film Water Uptake Measurement Using Quartz Crystal Microbalance (QCM)

Traditionally, the water uptake of polymer electrolytes is measured by dynamic vapor sorption (DVS) under varying relative humidity conditions. This technique provides good resolution in detecting the weight of water absorbed by the materials. However, its application is limited to bulk samples, ideally weighing a few grams. As previously mentioned, the thin film format utilized in this work necessitates a new technique that can precisely measure water uptake in significantly smaller quantities. Hence, we utilized a quartz crystal microbalance (QCM) to measure water uptake at the nanogram scale in thin films. To obtain information about water uptake at different relative humidity levels, a relative humidity generator that delivers tunable humidified gas is integrated into the system.

The QCM is a highly sensitive weighing technique that allows for the detection of minute mass changes on the order of nanograms or even picograms. This method is based on the piezoelectric properties of quartz crystals and their ability to oscillate at a specific resonant frequency. QCM has been widely used in various research fields, including materials science, surface chemistry, biology, and environmental science.

2.4.1 Principles of QCM

1. Piezoelectric effect

The piezoelectric effect is a property of certain materials, such as quartz, to generate an electric charge when subjected to mechanical stress. This effect is reversible, meaning that applying an electric field to a piezoelectric material will cause it to change shape or vibrate. The piezoelectric effect in quartz is primarily due to the asymmetric arrangement of its crystal lattice, which causes a net electric polarization when the crystal is deformed.

2. Resonant frequency and mass sensitivity

When an alternating electric field is applied to a piezoelectric quartz crystal, it vibrates at its resonant frequency, which is determined by the crystal's size, shape, and material properties. The resonant frequency of a QCM sensor is highly sensitive to mass changes on the crystal surface. As mass is added or removed, the frequency shifts proportionally. This phenomenon is described by the Sauerbrey equation:

$$\Delta f = -\frac{2f_0^2}{A*\rho*\mu}\Delta m \tag{2.10}$$

where Δf is the change in resonant frequency, f_0 is the fundamental resonant frequency, Δm is the change in mass, A is the active area of the crystal, ρ is the density of the quartz, and μ is the shear modulus of the quartz. The negative sign indicates that an increase in mass causes a decrease in frequency. The mass sensitivity of a QCM sensor depends on its resonant frequency, with higher frequencies generally providing higher sensitivity.

3. Limitations of the Sauerbrey equation

The Sauerbrey equation assumes that the added mass forms a rigid, uniform, and thin layer on the crystal surface. This assumption might not always hold, especially when dealing with soft materials, viscoelastic layers, or heterogeneous surfaces. In such cases, the frequency response of the QCM sensor can be more complex, and additional models or techniques, such as the Voigt model or the use of multiple harmonics, might be needed to accurately interpret the data.

2.4.2 QCM components and setup

The core component of a QCM sensor is a thin quartz crystal disk, typically ranging from a few hundred micrometers to over a millimeter in thickness. The crystal is often cut in a specific orientation, known as the AT-cut, which minimizes the effects of temperature on the resonant frequency. The quartz disk is coated on both sides with thin metal electrodes, usually made of gold or silver. These electrodes serve to apply an electric field across the crystal and to detect the resulting vibrations. The active area of the crystal, where mass changes are measured, is defined by the electrode geometry.

The quartz crystal is connected to an electronic oscillator circuit, which drives the crystal to vibrate at its resonant frequency. The oscillator circuit continuously monitors the resonant frequency and adjusts the applied electric field to maintain resonance. As mass is added or removed from the crystal surface, the resonant frequency shifts, and these shifts are detected by the oscillator circuit in real-time. A typical schematic diagram of QCM sensor and oscillator circuit is displayed in Figure 2.11.

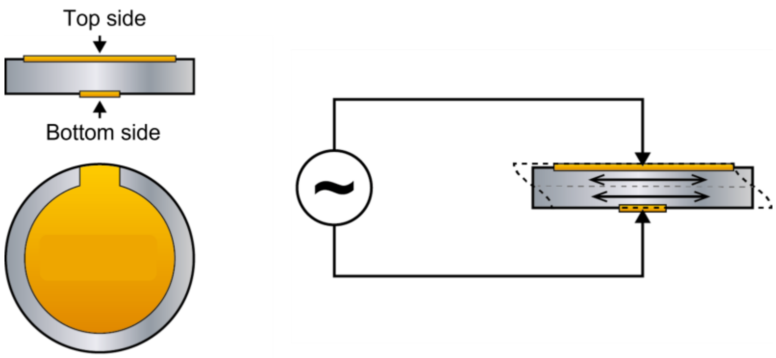

Figure 2.11 Schematic diagram and QCM sensor and QCM sensor connected to oscillator circuit

We employed QCM system bought from Gamry Instruments. The quartz crystal, with a central frequency of 5 MHz, is placed inside the chamber with rubber O-ring for sealing. The relative humidity inside the chamber is controlled by connecting to humidified air and the temperature is hold constant at room temperature by connecting to water circulator. A full experimental apparatus is displayed in Figure 2.12.

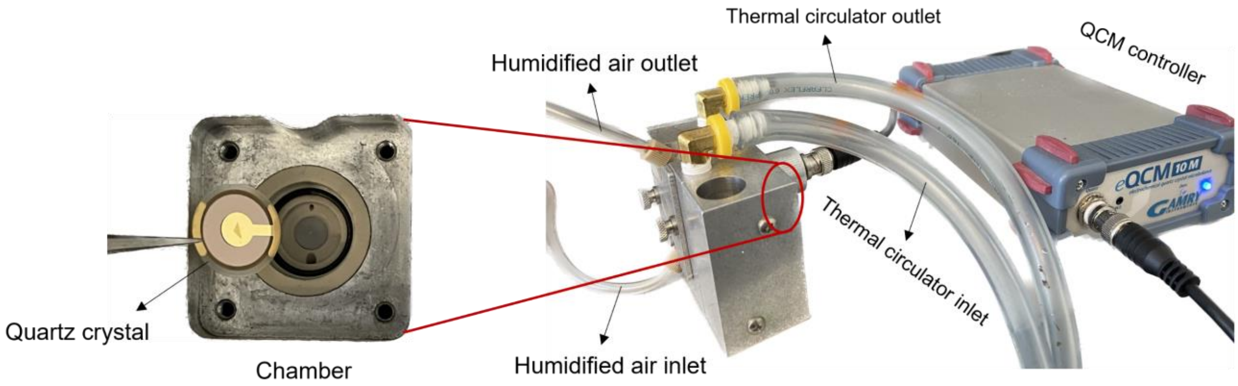

Figure 2.12 Experimental setup for thin film measurement using QCM. The temperature of the chamber is held constant by connecting to a thermal circulator. A small piece of tape is attached to the back side of the electrode to resist ringing effect.

The QCM system provides a powerful tool for studying the water uptake behavior of thin film polymer electrolytes. The ability to accurately measure water uptake at the nanogram scale allows for a more precise understanding of the relationship between hydration and ionic conductivity in these materials. Furthermore, the use of a relative humidity generator allows for the study of water uptake behavior under a wide range of relative humidity conditions, providing valuable insight into the performance of these materials under various operating conditions.

2.4.3 Factors affecting QCM measurements

During the measurements, the relative humidity was changed for roughly every 10 min. As the polymer electrolytes coated on the sensor is hydrophilic, higher relative humidity level leads to higher water absorption, resulting in decrease of the sensor's resonant frequency. Figure 2.13 is an example of frequency response of QCM sensor to different relative humidity levels.

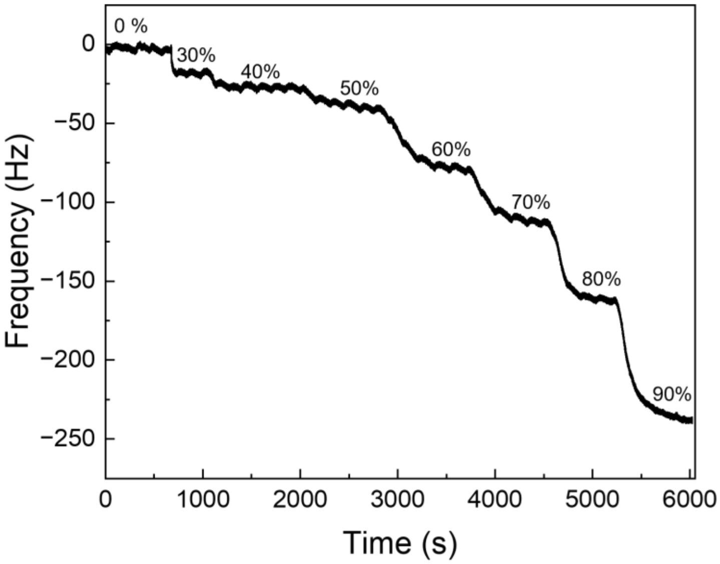

Figure 2.13 Frequency response to the change of relative humidity of polymer electrolytes coated QCM crystal sensor

There are a few factors that can affect the quality of the measurements, which need to be considered before doing the experiment:

1. *Temperature*

Temperature can influence the resonant frequency of a quartz crystal, leading to potential errors in mass measurement. The AT-cut crystal orientation is commonly used in QCM sensors to minimize the temperature-induced frequency shifts. However, even with an AT-cut crystal, maintaining a stable and well-controlled temperature during QCM experiments is crucial for accurate measurements. Temperature fluctuations can be minimized using temperature-controlled chambers, ovens, or other thermal management systems.

2. *Surface properties*

The surface properties of the QCM sensor, such as roughness, chemical composition, or the presence of a functionalized coating, can influence the sensitivity and specificity of the measurements. Surface roughness can affect the mass sensitivity of the sensor and introduce uncertainties in the measurement. The chemical composition of the surface can affect the adsorption or desorption processes, leading to changes in the frequency response or the reversibility of the measurements. Functionalized coatings can be used to enhance the specificity of the sensor by selectively binding to target molecules, but they may also introduce additional complexities in the data interpretation due to the viscoelastic properties of the coating.

3. *Frequency noise and stability*

The stability and noise level of the oscillator circuit can also influence the accuracy and resolution of QCM measurements. Factors that can affect the frequency stability include temperature fluctuations, mechanical vibrations, or electrical noise in the oscillator circuit. Various techniques can be employed to minimize these effects, such as using high-quality oscillators, temperature control systems, or vibration isolation platforms.

2.5 X-ray Scattering Techniques

X-ray scattering techniques are a powerful set of methods used to investigate the structural properties of materials on the atomic and molecular scale. These techniques make use of the interaction between X-rays and matter, where X-rays are scattered by the electron cloud surrounding the atoms in a sample. By measuring the scattered X-ray intensities at different angles, it is possible to extract valuable information about the structure, composition, and properties of the material under investigation. There are several X-ray scattering techniques, each offering unique insights into the material's properties. In this work, we will focus on the principles and applications two X-ray scattering techniques that were employed in my research.

2.5.1 Small Angle X-ray Scattering (SAXS)

Small Angle X-ray Scattering (SAXS) is a powerful technique to investigate the self-assembled nanostructures formed by these materials. Block copolymers tend to self-assemble into various nanostructures, such as spheres, cylinders, lamellae, and gyroids. SAXS can be employed to study the size, shape, and distribution of these self-assembled structures, as well as the long-range order and domain spacing in block copolymer systems. Figure 2.14 depicts a SAXS pattern for lamellar BCP, from which important information can be derived.

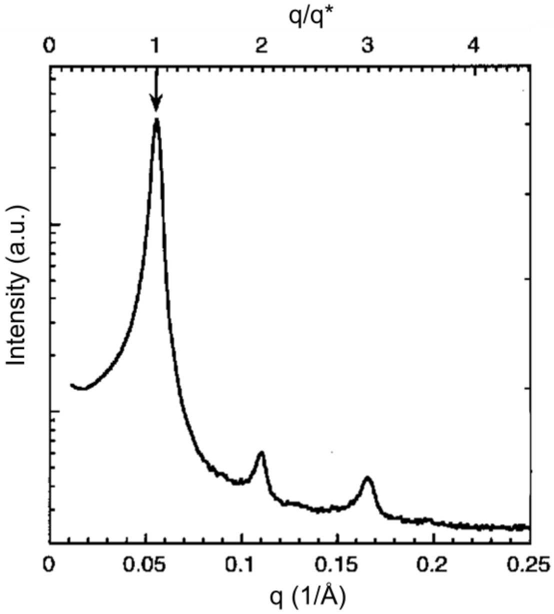

Figure 2.14 SAXS diffraction pattern obtained from BCP with lamellar morphology

1. *Morphology determination*

When X-rays interact with a block copolymer sample, they scatter due to the electron density fluctuations within the material. The scattered X-rays interfere with each other, resulting in a characteristic scattering pattern. This pattern can be analyzed to obtain information about the size, shape, and distribution of the self-assembled structures in the block copolymer.

The SAXS intensity profile (I(q) vs. q) provides information about the morphology of the block copolymer. Specific features in the scattering pattern, such as peaks and their positions, are related to the type of nanostructure formed. For example, lamellar, cylindrical, and spherical morphologies will produce different characteristic peaks in the SAXS profile. By fitting the scattering data to appropriate models or comparing the experimental data with simulated SAXS profiles for known morphologies, we can determine the morphology of the self-assembled nanostructures formed by the block copolymer.

Table 2.1 Peak position of x-Ray scattering for BCP of different morphologies

Morphology	q/q^*
LAM	$1, 2, 3, 4, 5, \ldots$
HEX	$1, \sqrt{3}, \sqrt{4}, \sqrt{7}, \sqrt{9}, \ldots$
GYR	$1, \sqrt{4}/3, \sqrt{7}/3, \sqrt{8}/3, \sqrt{10}/3, \ldots$
BCC	$1, \sqrt{2}, \sqrt{3}, \sqrt{4}, \sqrt{5}, \ldots$

2. *Domain spacing determination:*

The position of the peaks in the SAXS profile is related to the domain spacing (d) between the self-assembled structures. The domain spacing is the center-to-center distance between the nanostructures in a block copolymer system. This distance can be calculated using Bragg's law:

$$d = 2\pi/q^* \qquad (2.11)$$

where q* is the position of the peak in the scattering vector q. The presence of well-defined peaks in the SAXS profile indicates the degree of long-range order in the self-assembled nanostructures, with sharp peaks corresponding to highly ordered systems. By analyzing the position of the peaks in the SAXS profile and using Bragg's law, we can determine the domain spacing of the block copolymer system. This information is crucial for understanding the structure-property relationships in block copolymers and guiding the design of materials with tailored properties for specific applications.

2.5.2 X-ray Reflectivity (XRR)

X-ray Reflectivity (XRR) is a valuable technique for studying block copolymers, particularly when they form thin films or multilayers. XR can provide important information about the interface width between blocks and the layer thickness of the self-assembled structures, which is crucial for understanding the structure-property relationships in these materials and guiding the design of materials with tailored properties for specific applications. A typical XRR intensity spectrum is present as Figure 2.15 shows.

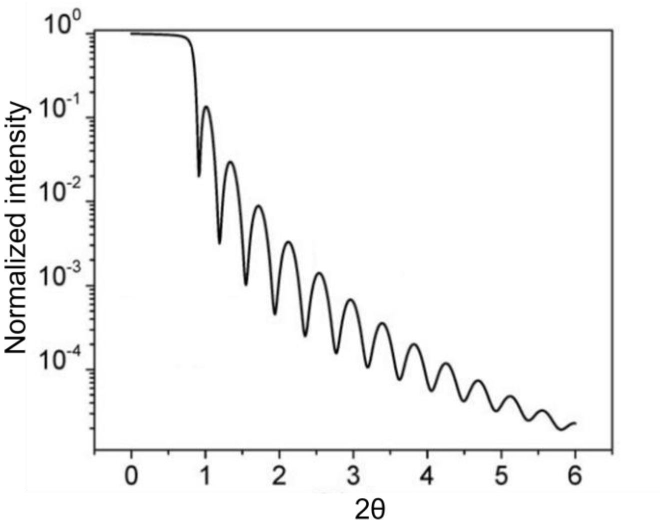

Figure 2.15 Schematic XRR reflectivity pattern of thin film

1. *Basic principles of X-ray Reflectivity*

XRR measures the intensity of X-rays reflected from a sample surface as a function of the incident angle (θ). When X-rays interact with a thin film or multilayer structure, they undergo multiple reflections at the interfaces between different layers or blocks. These reflections interfere with each other, resulting in an oscillating reflectivity pattern (Kiessig fringes) depending on the structural periodicity. By analyzing this pattern, information about the film thickness, interface width, and electron density profile of the block copolymer system can be obtained.

2. *Probing interface width between blocks*

The interface width between blocks in a block copolymer system can be determined from the shape and width of the reflectivity peaks in the XRR profile. A sharp peak indicates a well-defined interface with low roughness or intermixing between blocks, while a broad peak suggests a larger interface width due to roughness or interdiffusion between blocks.

To quantify the interface width, one can fit the experimental XRR data to appropriate models These approaches consider the electron density profile, layer thickness, and interface roughness, allowing for the extraction of the interface width between blocks in the block copolymer system.

3. *Probing layer thickness*

The layer thickness of the self-assembled structures in a block copolymer system can be determined from the position and periodicity of the reflectivity peaks in the XRR profile. For a periodic multilayer structure, the distance between adjacent peaks (Δq) in the scattering vector q is inversely proportional to the total thickness of the repeating unit (D):

$$\Delta q = 2\pi / D \tag{2.12}$$

By analyzing the position and periodicity of the peaks in the XRR profile, one can determine the layer thickness of the self-assembled structures in the block copolymer system.

CHAPTER 3

EFFECTS OF SEGMENTAL DYNAMICS AND WATER CONCENTRATION ON ION TRANSPORT IN HYDRATED POLYMER ELECTROLYTES

Abstract

Structure-property relationship of ion transport in hydrated polymer electrolytes is essential for the design and optimization of advanced polymer electrolytes. The study on the role of chain dynamics is relatively unexplored. In this work, we synthesized a series of crosslinked poly(2-vinylpyridine) (P2VP)-based polymers with different degree of crosslinking to control the chain dynamics with the minimal changed in the chemical structure. The chain dynamics is largely reduced by the crosslinking with higher glass transition temperature. However, the ionic conductivity of crosslinked materials is the same as un-crosslinked counterpart when the water concentration is hold constant. Therefore, the ionic transport is not dictated by the segmental dynamics of the chain, rather by the water concentration in the system. These findings enrich our understanding of ion transport mechanism and offer valuable insights for the design and development of materials with enhanced performance.

3.1 Introduction

Solid polymer electrolytes (SPEs) have gained prominence for their potential in fuel cell performance.[1,2] Nafion, a perfluorinated sulfonic acid (PFSA)-based membrane, is considered a standard in proton exchange membrane fuel cells (PEMFCs) due to its superior conductivity, chemical stability, and mechanical properties.[3–5] However, the acidic environment in which PEMs operate limits the choice of catalysts to precious metals such as platinum.[6,7] As an alternative, anion exchange membrane fuel cells (AEMFCs) operate in an alkaline environment, facilitating oxygen reduction and fuel oxidation reactions and permitting the use of low-cost, non-noble metal catalysts.[8,9] Despite this, AEMs typically exhibit lower ionic conductivity than PEMs due to the intrinsically lower mobility of OH^-.[8]

The molecular structure of the polymer electrolytes can largely affect the properties and performance of the devices. Various properties are required to meet the standard of real-world applications: high conductivity, reasonable water uptake, low dimensional swelling, good chemical stability etc. Therefore, researchers have put efforts on tuning the molecular structure of the electrolytes to construct the structure-property relationships. For example, Yan group found that with increasing number of cations on the side chain while maintaining the same IEC, the hydrophilic-hydrophobic phase separation is enhanced, which lead to increased ionic conductivity and suppressed water uptake.[10] The Bae group changed the backbone structure from para- to meta-position on the benzyl ring, where in the latter case the hydrophilic side chains are more easily to fold back, largely increasing the microphase separation behavior. Thus, the ionic conductivity is highly enhanced due to the formation of ionic clusters and percolated conducting pathways.[11]

These previous studies have contributed a lot to the understanding of structure-property relationship for ion transport in the anion exchange membrane. However, the role of the backbone chain dynamics on the ion transport is rarely touched. In the dry poly(ethylene oxide)-based polymer electrolytes, where the lithium ions transport via intrachain hopping and interchain hopping by the coordination of the ether oxygen atoms on a segmental PEO chain.[12] When the temperature is below the melting point of the semicrystalline structure of PEO, the conductivity is very low due to restricted segmental mobility of the PEO chain. Once the temperature goes above the melting point, the ionic conductivity will be largely increased.[13] The temperature-dependent conductivity can usually be plotted to Vogel–Tammann–Fulcher (VTF) model, which indicated the ion transport relies on the segmental dynamics. And the conductivity of materials with different molar fraction of PEO can collapses after the correction to the respective glass transition temperature.[14] Chu et al. has done a pioneering work revealing how the increased water uptake affect the chain dynamics by a combination of experimental and molecular dynamic simulation tools. They found the glass transition temperature of the hydrated polymer electrolytes were significantly decreased when the presence of water increased and the relaxation time for the chain at higher water uptake is remarkably lower, indicating faster chain dynamics.[15] However, the relationship between the chain dynamics and the ion transport properties still remains unclear.

In this study, we delve into the impact of segmental dynamics on the ion transport properties of hydrated polymer electrolytes. We have systematically varied the degree of crosslinking by adjusting the molar percentage of the crosslinker. We utilized a thermal crosslinking strategy that involves the incorporation of the crosslinker into the polymer backbone. This approach boasts significant advantages over introducing the crosslinker into the polymer solution, such as enhanced solvent processability and precise control over the degree of crosslinking.[9,16,17] The polymer electrolytes were prepared in a thin film format for the property measurements. This facilitated the quantitative analysis of water uptake, swelling ratio, water concentration, and ionic conductivity, and revealed the complex interrelationships between these factors. We also opted for monovalent iodide ion (I^-) conductivity measurement over hydroxide ion (OH^-), to circumvent the ambient carbonation issue associated with hydroxide ions.[18,19] Our findings indicate that ion transport is largely dependent on the water concentration in the materials instead of segmental dynamics of the polymer chain. Through this research, we have gained a deeper understanding of the structure-transport relationship. Our findings lay a robust foundation for the future design and optimization of materials intended for sustainable energy devices.

3.2 Results and Discussion

3.2.1 Synthesis and characterization of crosslinkable polymers

We synthesized a series of five poly(2-vinylpyridine) (P2VP)-based polymers, each containing varying amounts of crosslinkable 4-vinylbenzocyclobutene (BCB) units, using nitroxide-mediated polymerization (NMP) (Figure 3.1a). Post-synthesis, these polymers underwent thermal crosslinking at 240 °C for 15 min, followed by methylation in a methyl iodide (MeI) vapor environment for 24 hours (Figure 3.1b).

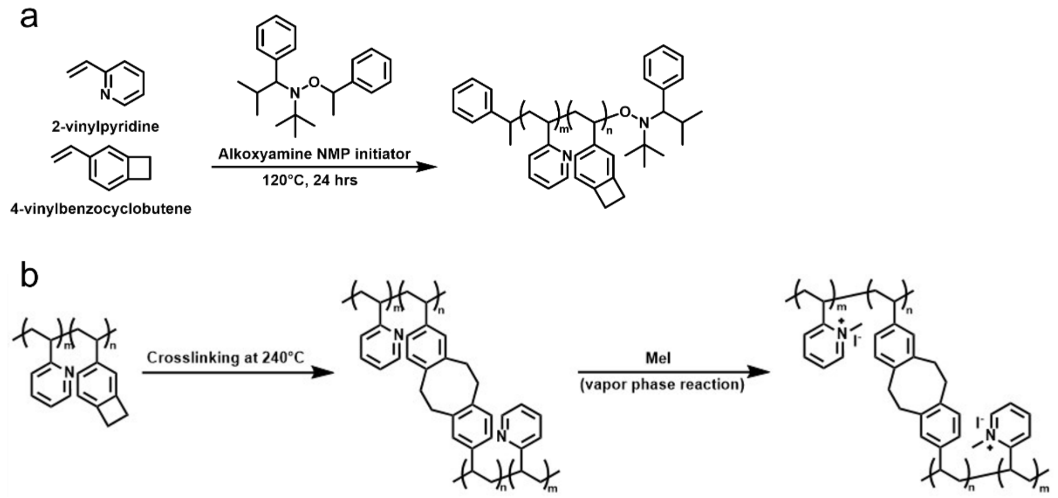

Figure 3.1. (a) Synthesis of random copolymer P(2VP-*co*-BCB). (b) Crosslinking and subsequent vapor phase methylation (end groups omitted for simplicity).

This sequence was selected based on thermogravimetric analysis (TGA) data, as the crosslinking temperature sits between the degradation temperature of functionalized quaternary ammonium groups (200 °C) and the unfunctionalized P2VP backbone (400 °C) (Figure 3.2).

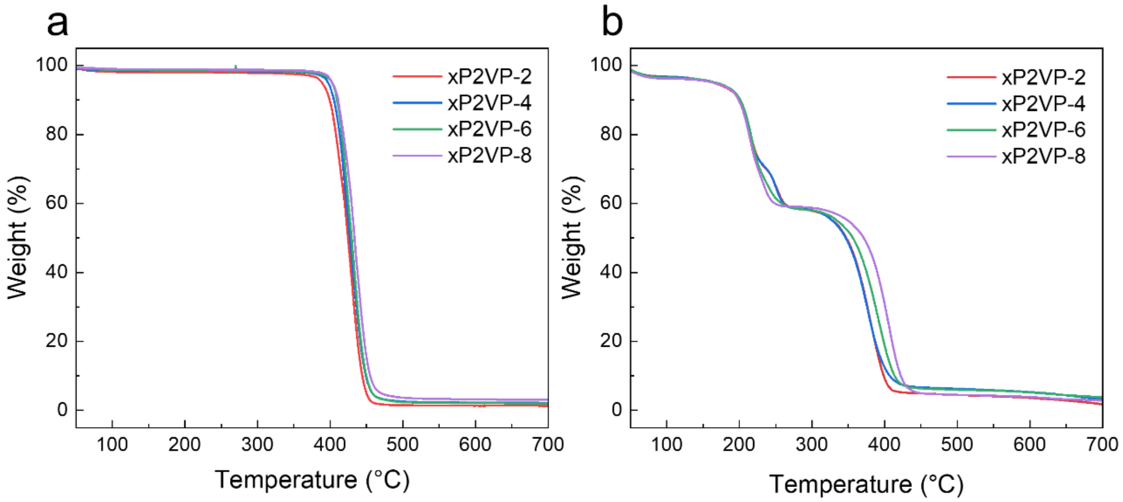

Figure 3.2. Thermogravimetric analysis (TGA) of cross-linkable polymers: (a) unfunctionalized polymers, and (b) methyl iodide-functionalized polymers. All samples were only cross-linked during the TGA scanning measurement.

Absolute molecular weights of the synthesized polymers were determined *via* size-exclusion chromatography with multi-angle light scattering (SEC-MALS), yielding the dn/dc values for each polymer (Figure 3.3).

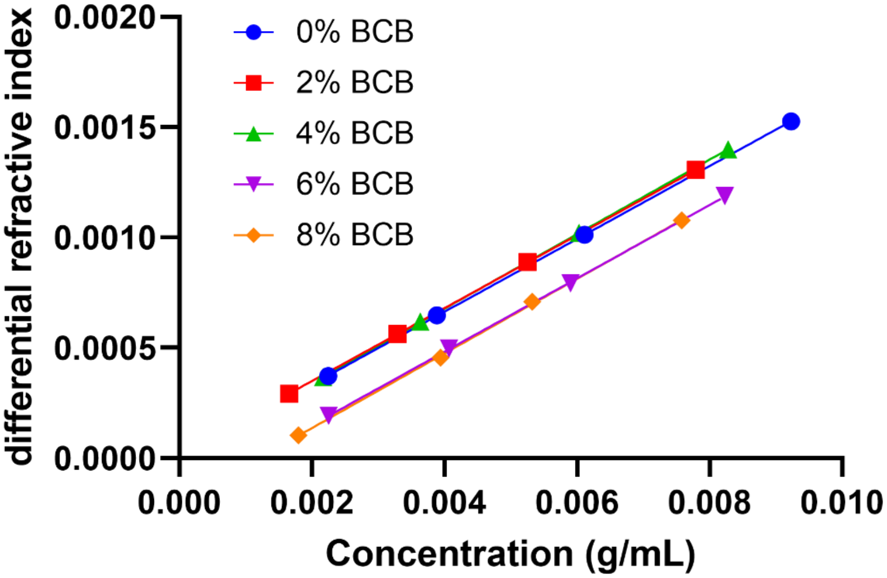

Figure 3.3. Differential refractive index as a function of differential concentration for five polymers of different percentage of crosslinker BCB.

Additionally, polymerization progression was monitored by assessing molecular weight and dispersity changes at different timepoints (Figure 3.4,3.5).

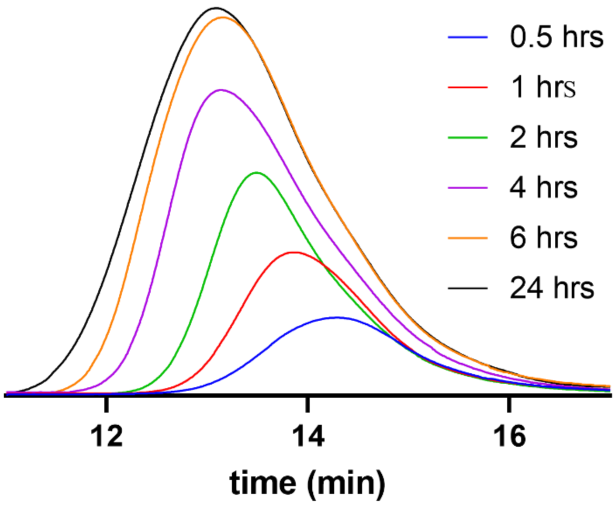

Figure 3.4. SEC traces of x-P2VP8 at different timepoints during the polymerization.

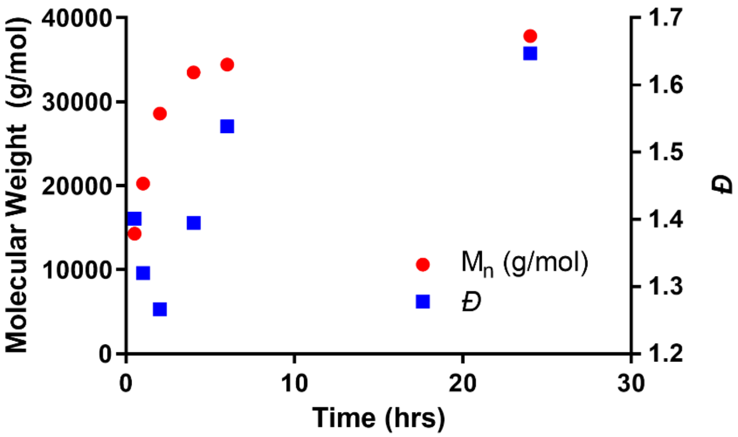

Figure 3.5. Molecular weight (left) and dispersity (right) of x-P2VP8 at different timepoints during the polymerization.

Despite the kinetic behavior surpassing the linear regime of controlled polymerization, the final polymers were isolated late in the process to ensure maximum BCB incorporation. The resulting polymers, denoted as xP2VP-y (where y represents the molar feed percentage of BCB), exhibited typical Mn values of ~38 kDa and Đ values of 1.66, with xP2VP-4 being an exception (Figure

3.6a). The feed ratio (f_{BCB}) and the final copolymer composition (F_{BCB}) of BCB in the polymers were compared (Figure 3.6b), as determined by ^{1}H NMR (Figure 3.6c). As expected, F_{BCB} was consistently lower than f_{BCB}, indicating an initial 2VP predominance, with increased BCB incorporation over time. Notably, a linear relationship was observed between F_{BCB} and f_{BCB}, suggesting a predictable trend for BCB incorporation relative to the feed ratio.

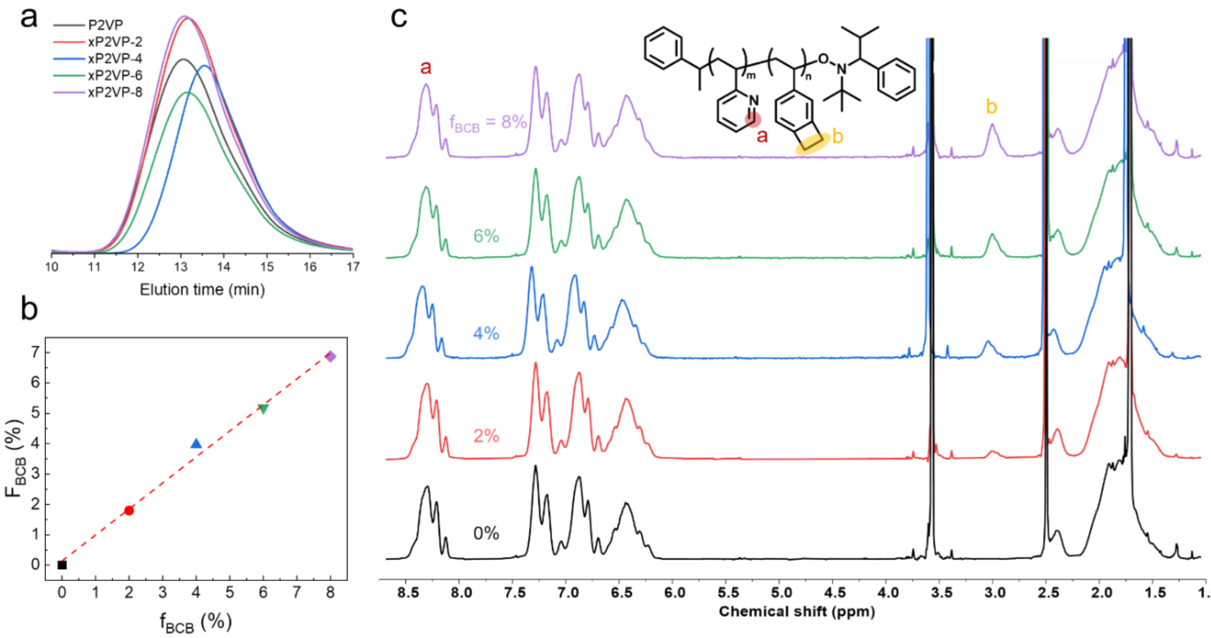

Figure 3.6. (a) SEC traces of five P2VP-based polymers containing various mol% of BCB. (b) Molar percentage of BCB in final polymer vs. feed ratio. (c) ^{1}H NMR spectra of P2VPs with different mol% of BCB unit.

3.2.2 Materials properties characterization of the crosslinked polymer network

The crosslinked and methylated polymers were prepared as thin films (~100 nm) for characterization. All materials exhibited the same degree of methylation (ca. 50%), as determined from the integral area percentage of C-N$^+$ and C-N peaks from FTIR spectra (Figure 3.7), with an IEC of 2.84 meq g^{-1}. The uniformity of methylation is further corroborated by the consistency in the weight percentage degradation of quaternary ammonium groups, as determined through TGA (Figure 3.2).

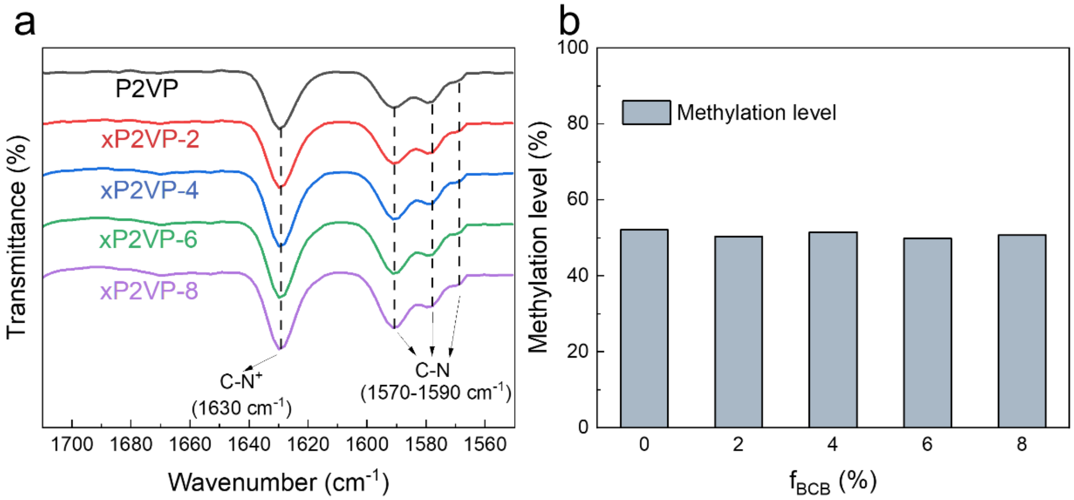

Figure 3.7. (a) FTIR spectra of MeI-functionalized polymers. Spectra was shifted vertically for clarity. (b) Methylation level of different polymers, calculated from the integrated area percentage of C-N^+ peak.

We used differential scanning calorimetry (DSC) to measure the glass transition temperature (Tg) of the crosslinked network. Prior to methylation, polymers with varying DCs displayed about a 30 °C difference in Tg, with a higher DC leading to a higher Tg (Figure 3.8a). The increased introduction of crosslinks restricts segmental mobility, thus raising the Tg.[20] Post-methylation, the Tg of each polymer remained relatively unchanged in the dry state (Figure 3.8b). However, when we measured the Tg of methylated polymers equilibrated at 80% RH (Figure 3.8c), the Tg of the hydrated polymers electrolytes matches what is predicted by Fox equation[21] (Figure 3.8d) and a dramatic decrease was observed due to the water plasticization effect. For instance, P2VP's Tg declined by over 84 °C (from 90.9 °C to 6.7 °C). Importantly, at 80% RH, the Tg of low DC polymers (P2VP, xP2VP-2, and xP2VP-4) is below 25 °C - the temperature at which the following conductivity measurement in Figure 3.12a was performed - while high DC polymers (xP2VP-6 and xP2VP-8) maintain a Tg above this temperature.

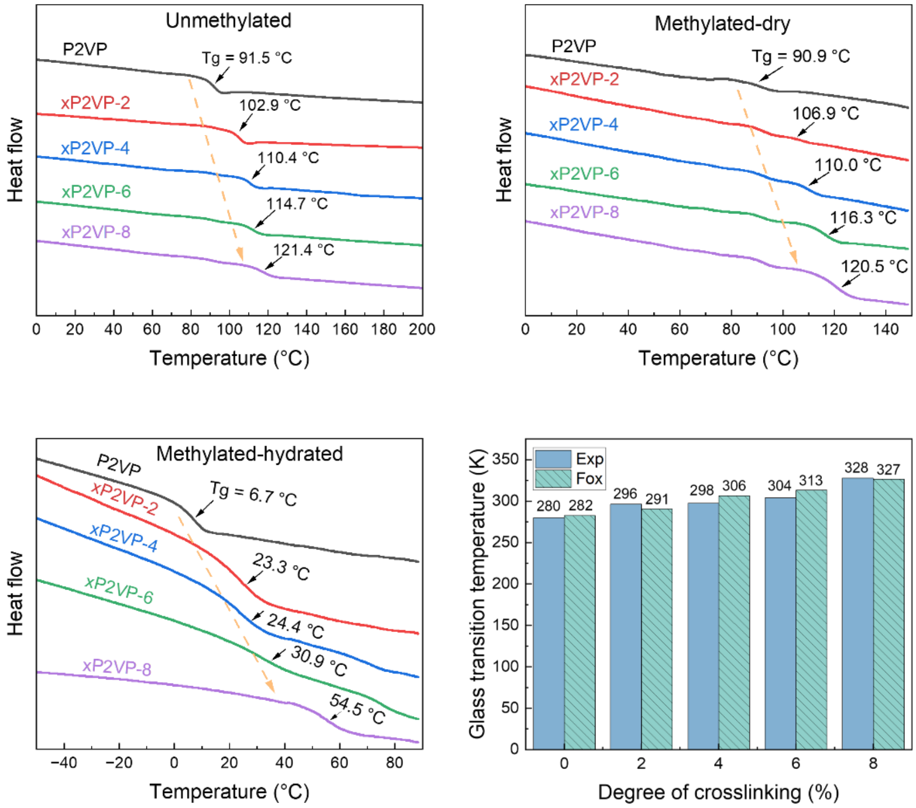

Figure 3.8. DSC heating curves of (a) unmethylated P2VP, (b) dry methylated P2VP, and (c) hydrated methylated P2VP of different degree of crosslinking. T_g was measured on the second heating cycle and determined from the inflection point for all samples. (d) Comparison between predicted Tg by Fox equation and experimentally determined values.

Figure 3.9a presents the typical frequency response when water is absorbed in the thin film, with the frequency decrease as higher RH levels are applied. We calculated weight of water for each thin film as shown in Figure 3.9b. Hydration number λ (average number of water molecules solvating each ionic group) and water uptake for methylated P2VP at different DC as a function of relative humidity (RH) are shown in Figure 3.9c. At 30% RH, all materials demonstrated λ values below 1, indicating low water content. However, at 90% RH, water absorption and λ values significantly increased. Importantly, materials with lower DC consistently showed higher λ values, indicating restricted water absorption in high DC polymers. For instance, λ for P2VP is nearly double that of xP2VP-8 at 90% RH (7.4 vs. 4.1, respectively).

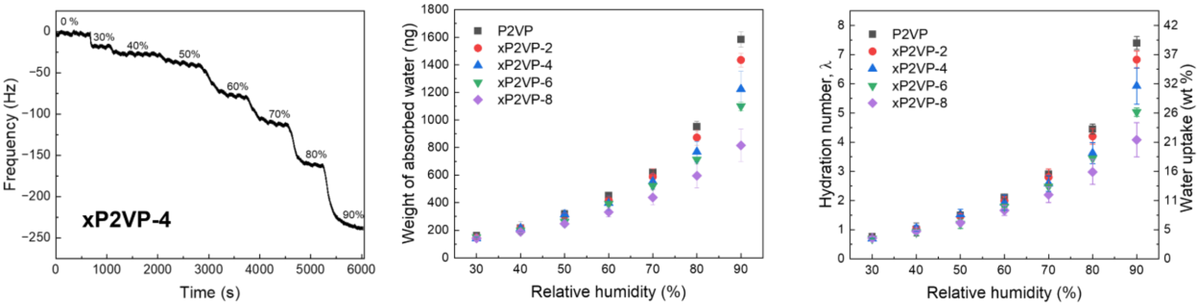

Figure 3.9. (a) QCM quartz crystal frequency response with the changes of RH levels, (b) Calculated weight of absorbed water in the thin film as a function of RH (c) Hydration number (left) and water uptake (right) as a function of RH. Measurements were performed at 25 °C.

The correlation between water uptake and thickness changes became evident as we further analyzed these polymers. Figure 3.10a illustrates the thickness expansion of thin films as a function of RH. Then swelling ratio was calculated in Figure 3.10b. The swelling ratio increased with RH, with lower DC polymers exhibiting higher swelling ratios. A significant variance in the swelling ratios of different DC polymers was noted at high RH. For example, at 90% RH, the swelling ratio of P2VP is 27.6%, while that of xP2VP-8 is only 19.1%. These findings align with other reported work,[22,23] demonstrating that higher DC restricts chain movement, thereby suppressing volume expansion and reducing water absorption.

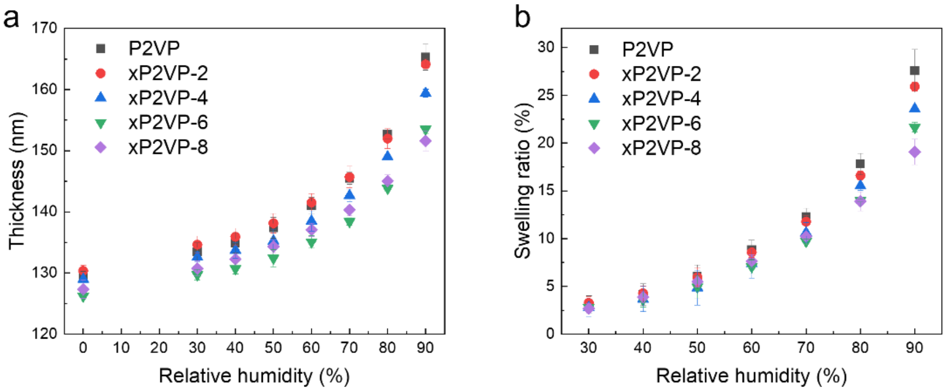

Figure 3.10. (a) QCM quartz crystal frequency response with the changes of RH levels, (b) Calculated weight of absorbed water in the thin film as a function of RH (c) Hydration number (left) and water uptake (right) as a function of RH. Measurements were performed at 25 °C.

To delve deeper into the water absorption behavior, we compared water uptake and thickness expansion between P2VP and xP2VP-8 at 90% RH. Despite the hydration number increasing 1.81-fold from xP2VP-8 to P2VP, thickness expansion in P2VP was only 1.47-fold higher. This discrepancy suggests a non-ideal mixture between the polymer electrolytes and water, potentially attributable to strong intermolecular interactions causing mixture volume contraction.[24,25]

Water absorption in these polymers is pivotal for efficient ion transport. From the aforementioned comparison, we speculate that not only the number of water molecules but also their spatial arrangement within the system is critical for the efficiency of water-solvated ion transport. Thus, we examined both the water uptake and thickness change, calculating the water concentration (g/cm^3) for all the polymer electrolytes as a function of RH (Figure 3.11). This was derived from the weight of absorbed water measured by QCM and the corresponding volume of the hydrated polymer thin film. At 30% RH, the water concentration was low (ca. 0.05 g/cm^3), substantially increasing at 90% RH (to 0.40 g/cm^3 and 0.22 g/cm^3 for P2VP and xP2VP-8, respectively). A decrease in water concentration with increasing degree of crosslinking was observed at each RH level. It's important to note that we opted not to calculate the ionic group concentration in the polymer electrolyte-water mixture since water, despite being a minor component, plays a more pivotal role in determining ionic conductivity given the relatively low water uptake across all materials.

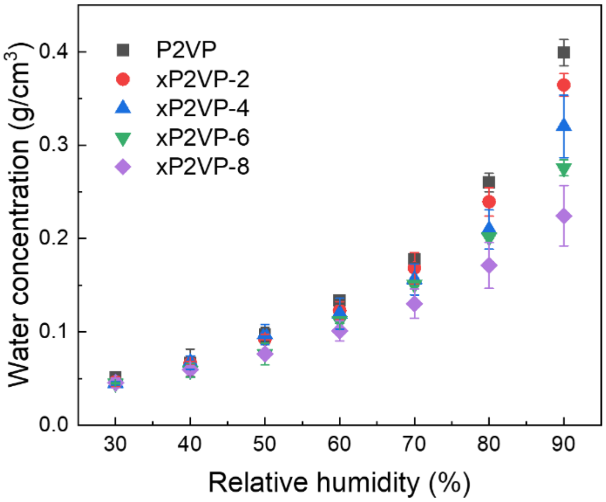

Figure 3.11. Calculated water concentration of P2VP with different degree of crosslinking as a function of RH.

3.2.3 Effect of segmental dynamics and water concentration on ion transport

We investigated the iodide ion conductivity of all materials, measuring this property in a thin-film format on interdigitated electrodes (IDEs).[26–29] Figure 3.12a illustrates the conductivity of methylated P2VP with different DC as a function of RH at 25 °C. From 30% to 90% RH, all polymer electrolytes manifested a substantial increase in conductivity - over three orders of magnitude. Moreover, the conductivity at a given RH level was higher for polymers with a lower DC. For clarity, we normalized the conductivity of crosslinked samples to that of the non-crosslinked P2VP, as shown in Figure 3.12b. Across all RH levels, conductivity waned with increasing DC. For instance, despite an identical IEC, the conductivity of xP2VP-8 was as low as 20% of that for P2VP. Intriguingly, the normalized conductivity of these crosslinked materials remained a relatively constant fraction of that for P2VP across different RH levels. The most important finding is that the normalized conductivity of higher degree of crosslinking polymers does not decrease at 80% when the Tg is still above the measuring temperature (25 °C) while that of lower degree of crosslinking is already below 25 °C. This indicates that the flexible chain has negligible role in affecting the ion transport compared to frozen chains.

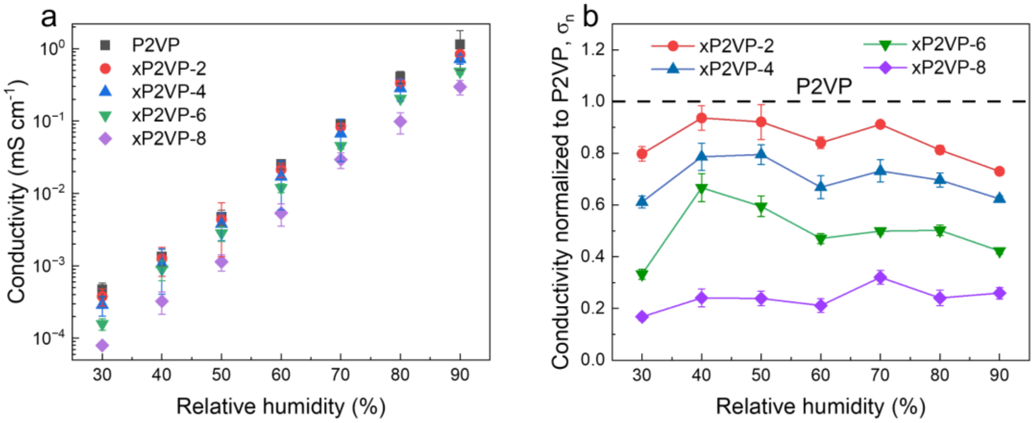

Figure 3.12. (a) Conductivity of methylated P2VP with different degree of crosslinking as a function of RH measured at 25 °C. (b) Conductivity of various methylated crosslinked P2VP normalized to non-crosslinked P2VP.

Instead, we plot the conductivity for all polymers against water concentration as shown in Figure 3.13a. The data points fit well to the power-law relationship $\sigma = \sigma_0 * (c - c_0)^p$, where σ_0 = 31.2, c_0=0.03, and p = 3.1, as indicated by the solid red line. It is important to note that when the value of water concentration is low, water concentration is similar to the volume fraction of water in the materials, where usually percolation theory is used to analyze the conductivity.[30] Our results revealed a consistent increase in ionic conductivity, independent of DC, with rising water concentration. Elevated water concentration suggests the likely presence of free or unbound water present within the polymer electrolytes, a prerequisite for initiating the vehicular transport mechanism,[31,32] after water solvates the ionic groups as bound water. Moreover, as the water concentration increases, the shorter distance between water and solvated ions further facilitates the formation of connected ion-conducting pathways.

Table 3.1. Arrhenius fit parameters for polymer electrolytes measured at 80% RH.

Material	A (mS cm^{-1})	E_a (kJ mol^{-1})
P2VP	441	16.78
xP2VP-2	2384	21.69
xP2VP-4	3478	23.06
xP2VP-6	17843	27.75
xP2VP-8	77611	32.45

Further investigations entailed temperature-dependent conductivity measurements at a constant RH level of 80% for all materials. The data exhibited Arrhenius-type temperature dependence (Figure 3.13b), with fitting parameters provided in Table 3.1. Under these conditions, the thermal activation energy for ion transport ranged from 16.78 kJ mol^{-1} to 32.45 kJ mol^{-1}. Materials with higher degree of crosslinking showed increased activation energy due to the lower water concentration, which impeded efficient ion transport. Such Arrhenius-type temperature-dependent conductivity is commonly reported in the literature.[22,23,33]

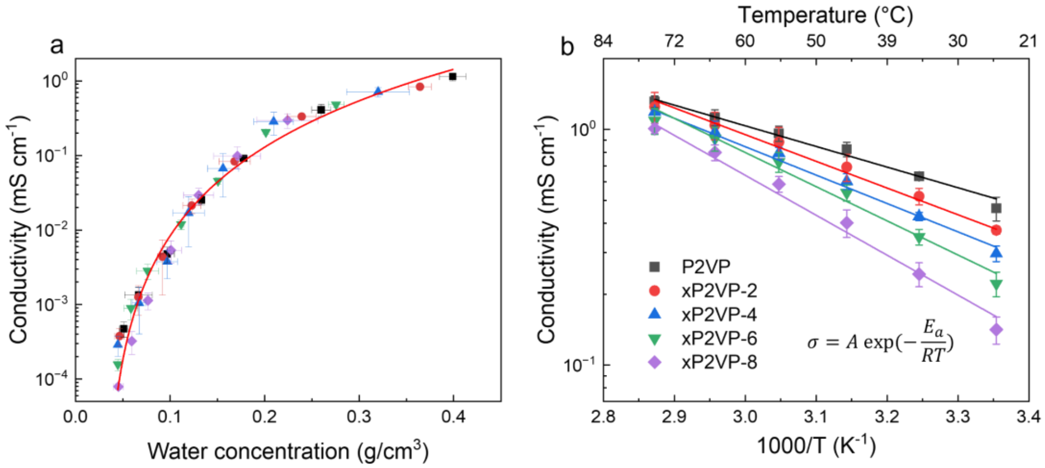

Figure 3.13. (a) Conductivity as a function of water concentration. Orange solid line represents a power law fit. (b) Ionic conductivity of methylated P2VP with different degree of crosslinking in Arrhenius-type temperature plot.

To further investigate the effect of segmental dynamics and water concentration on the ion transport property, we chose two materials, namely xP2VP-4 and xP2VP-8. We first performed DSC to measure the Tg of both crosslinked and uncrosslinked materials under two conditions: unfunctionalized and hydrated state (80% RH) as shown in Figure 3.14. The crosslinked polymers have higher Tg than their uncrosslinked counterparts for both conditions, indicating decreased segmental dynamics.

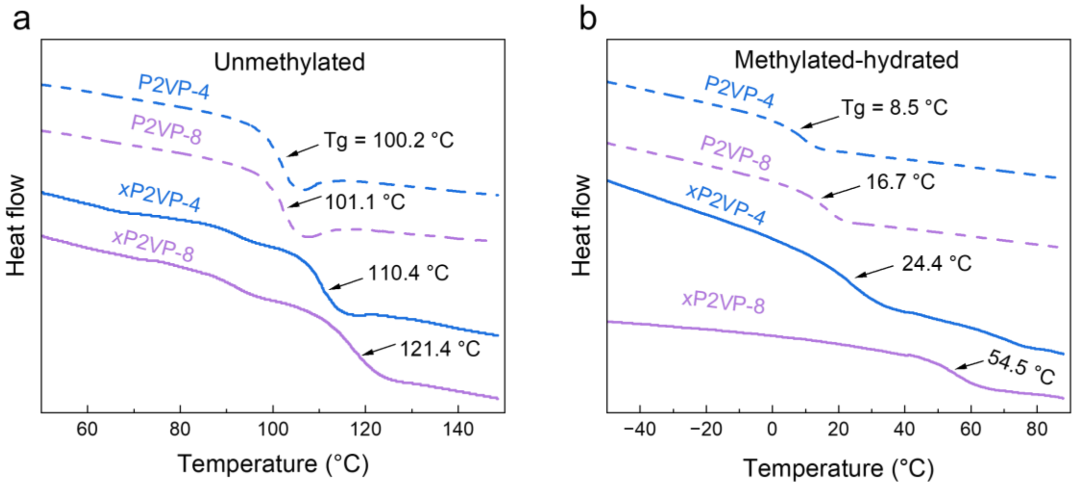

Figure 3.14 DSC curves of crosslinked and uncrosslinked P2VP-4 and P2VP-8 before methylation (a) and at hydrated state (b).

We then calculated their water concentration as a function of RH for both crosslinked and uncrosslinked one as shown in Figure 3.15a-b. At given RH, the water concentration of uncrosslinked polymer is higher than the crosslinked counterparts and the disparity decreases as the degree of crosslinking decreases. We then measured the conductivity of the uncrosslinked polymers at certain RH levels so that same water concentration as the crosslinked polymers can be achieved and the data was plotted in Figure 3.15c. It is obvious that when the water concentration for both these two polymers are hold constant, whether the materials are crosslinked or not does not affect the conductivity. In other words, the segmental dynamics induced by crosslinking has no effect on determining ion transport. Instead, water concentration dictates the ion transport property, as clearly the conductivity increases rapidly with higher water concentration and the conductivity of crosslinked and uncrosslinked polymers collapse.

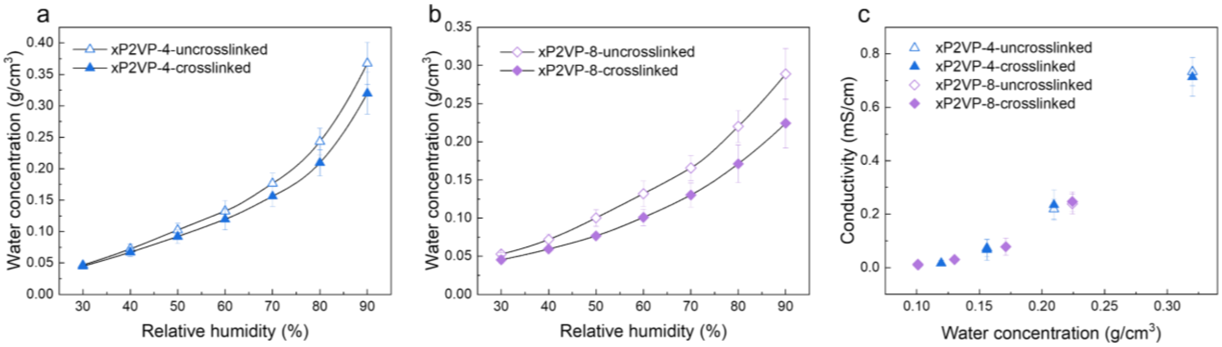

Figure 3.15. Water concentration as a function of RH of both crosslinked and uncrosslinked polymers for (a) xP2VP-4 and (b) xP2VP-8. (c) Ionic conductivity as a function of water concentration.

In many studies, conductivity is typically plotted against hydration number λ,[22,23,34,35] therefore we performed analysis based on hydration number besides water concentration as shown in Figure 3.16. Figure 3.16a-b show the hydration number as a function of RH for these two materials, both crosslinked and uncrosslinked. Similar trends were observed that hydration number increases as increasing RH and the uncrosslinked polymer always have higher hydration number. However, when the conductivity of the uncrosslinked polymer was measured at the same hydration number as crosslinked counterparts, there is substantial difference between crosslinked and uncrosslinked polymers as shown in Figure 3.16c. This indicates that hydration number might not be able to effectively serve as a parameter to account for the conductivity difference. Therefore, in our study, plotting against water concentration is more robust. This comparison indicates that not just the number of water molecules maters but more precisely the spatial distribution of them plays a central role in affecting the ion transport.

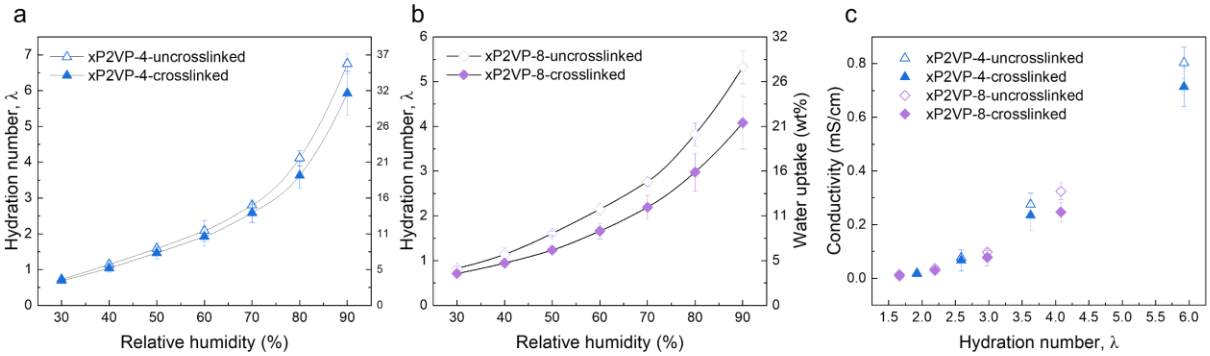

Figure 3.16. Hydration number as a function of RH of both crosslinked and uncrosslinked polymers for (a) xP2VP-4 and (b) xP2VP-8. (c) Ionic conductivity as a function of hydration number.

3.3 Conclusion

In summary, we synthesized and characterized a series of crosslinked poly(2-vinylpyridine) (P2VP)-based polymers with different DC. The integration of varying amounts of crosslinkable 4-vinylbenzocyclobutene (BCB) units, followed by thermal crosslinking and methylation, provided us with tunable degree of crosslinking in our polymer series. We observed that increased degree of crosslinking effectively curtailed water absorption and swelling. Although higher DC led to a reduction in ionic conductivity, the impact of the polymer backbone's segmental mobility on the ion transport was negligible. By a comprehensive analysis of hydration, swelling, and conductivity properties, we revealed that the water concentration within the polymer electrolytes plays a pivotal role in the efficiency of iodide ion transport. This study not only offers a new platform for exploring the structure-property relationship of crosslinked AEMs, but it also provides insights to guide future advances in polymer electrolytes for use in AEMFCs.

3.4 Experimental Section

3.4.1 Materials

2-vinylpyridine (2VP) was purchased from Fisher Scientific and the inhibitor was removed through a basic alumina column before use. 4-vinylbenzocyclobutene (BCB) was purchased from Sigma-Aldrich and vacuum distilled (75°C, 1 Torr) before use. The alkoxyamine NMP initiator, N-tert-Butyl-N-(2-methyl-1-phenylpropyl)-O-(1-phenylethyl)hydroxylamine, was purchased from Sigma-Aldrich and used as received. Tetrahydrofuran (THF) and hexanes were purchased from Fisher Scientific and used as received. All other chemicals (methyl iodide, toluene, 2-propoanol, N-methyl-2-pyrrolidone, acetone) were purchased from Sigma-Aldrich or Fisher Scientific and used without further purification. 5 MHz Au Quartz Crystals for Quartz Crystal Microbalance (QCM) measurement were bought from Gamry. The interdigitated electrodes (IDEs) were fabricated on semiconducting polished wafer (1 μm thermally grown oxide layer) received from WRS materials. Negative photoresist (AZ nLof 2020) and developer (AZ 300 MIF) for microfabrication were both purchased from AZ Electronic Materials.

3.4.2 Characterizations

^{1}H NMR spectra were recorded on a Bruker Avance III HD nanobay 400 MHz spectrometer. Size-exclusion chromatography with multi-angle light scattering (SEC-MALS) to determine the Mn and dispersity (Đ) of xP2VP polymers was performed on a Shimadzu gel permeation chromatography system equipped with a Wyatt DAWN HELEOS II multi-angle light scattering detector, a Wyatt ViscoStar III differential viscometer, a Wyatt Optilab T-rEX differential refractive index detector and a Shimadzu SPD-M30A photodiode array detector (200–800 nm). A 1:3 DMF/THF mobile phase was used, and the column sets were two Agilent PLgel 5 μm MIXED-D plus guards. The dn/dc used to determine absolute molecular weights was measured by injecting four dilute solutions of polymer in 1:3 DMF/THF (approx. concentrations: 2, 4, 6, 8 mg/mL) in succession into the refractive index detector alone until the dRI signal was stable (approximately five minutes per solution), after which the data was processed and linearly fit by Wyatt Astra software. Thermogravimetric analysis (TGA) was recorded on a TA Discovery thermogravimetric analyzer, where the samples were equilibrated at 50 °C for 5 min to remove any trapped volatile components, and then heated at a rate of 10 °C min−1 to 700 °C under an N2 atmosphere. Differential scanning calorimetry (DSC) was performed on a TA Discovery DSC 2500. The glass transition temperature (Tg) was measured on the second heating cycle. Fourier-transform infrared spectroscopy (FTIR) were performed on PerkinElmer Frontier FT-IR spectrometer in the range of 2000 cm^{-1} to 1000 cm^{-1} with 20 scans using an attenuated total reflectance (ATR) accessory to determine the degree of methylation level.

3.4.3 Synthesis of crosslinkable poly(2-vinylpyridine-co-4-vinylbenzocyclobutene) [xP2VP]

xP2VP was synthesized by nitroxide-mediated polymerization (NMP) as copolymers of 2VP with varying molar feed ratios of BCB (0-8%). The alkoxyamine NMP initiator (12.2 mg, 0.0375 mmol) was combined with 20 mmol of total monomer (e.g., for 8 mol% feed of BCB: 1934.9 mg 2VP [18.4 mmol] and 208.3 mg BCB [1.6 mmol]) in a glass tube with a magnetic stir bar. The resulting mixture was bubbled with dry nitrogen for 30 mins, after which the reaction mixture was stirred at 120°C for 24 h under a nitrogen atmosphere. To determine the kinetics of the polymerization, a needle and syringe were sparged with dry nitrogen, and a small volume of the reaction mixture containing 8 mol% feed of BCB was extracted at specific reaction times for analysis. After 24 h of reaction time, the reaction vessel was rapidly quenched via immersion of the tube into liquid nitrogen. A large volume of THF was then added to the tube, and after three cycles of precipitation of this solution into hexanes, the purified product was dried overnight in high vacuum at room temperature to yield **xP2VP** as a white powder. The copolymer compositions of each resulting polymer were determined by ^{1}H NMR spectroscopy, using the integrations of 2VP and BCB asterisked here: ^{1}H NMR (400 MHz, THF-d_8); δ ppm: 8.6-8.0* (1H, 2VP ArH), 7.5-6.1 (3H, 2VP ArH; 3H, BCB ArH), 3.2-2.8* (4H, cyclobutene CH_2 BCB) 2.6-1.3 (backbone CH and CH_2).

3.4.4 Thermal cross-linking procedures for thin film

Thin films of cross-linkable polymers were first made by spin-coating polymer solution (dissolved in Anisole) onto the silicon wafer substrates (ca. 1cm × 1 cm). Then the samples were placed onto a hotplate with temperature set at 240 °C in N_2-filled glovebox for 15 min to start thermal cross-linking reaction. Thickness was measured with ellipsometry after cross-linking, with around 100 nm film thickness obtained.

3.4.5 Methylation of polymer thin film

Substrates coated with cross-linked polymer thin film were then transferred to a 200 ml dark jar with face up. Subsequently, 4 ml vial filled with 2 ml of methyl iodide was placed on the bottom of the jar and then close the jar. The methylation reaction happened at room temperature, and it took 24 hours to fully functionalize the 2VP units.

3.4.6 Determination of methylation level

Around 100 nm of thin film was first spin coated on gold-coated (100 nm) silicon wafers (1 × 1 cm^2), which were chosen as substrates due to excellent reflectance. Then procedures for methylation reaction was followed as described above. Methylation level is specified as f, mole fraction of 2VP/NMP$^+$I$^-$ unit in the P2VP chain. This value was estimated by FTIR measurement, which can be calculated by equation S1,

$$f = \frac{A_{\mathrm{C}-N^+}}{A_{\mathrm{C}-N^+} + A_{\mathrm{C-N}}} \tag{S1}$$

where $A_{\mathrm{C}-N^+}$ is the integrated area of peaks associated with C-N$^+$ stretching, and $A_{\mathrm{C-N}}$ is the integrated area of peaks corresponding to C-N stretching. C–N$^+$ stretching was observed at 1630 cm^{-1}, while C-N signal intensity was displayed in the range of 1570–1590 cm^{-1} and the signal increased with increased exposure time to methyl iodide vapor.

3.4.7 In-situ thin film thickness measurement via ellipsometry

Methylated cross-linked thin film deposited on silicon wafer (2 × 2 cm^2) was placed on the liquid cell stage (500 µl Alpha Liquid Cell) installed on the ellipsometer (J.A. Woollam alpha-SE). The liquid cell chamber was subsequently fastened firmly onto the sample surface to ensure sealed environment. Linkam RH95 Humidity Controller was connected to the flow cell to control the RH level by pumping humidified air at constant flow rate. RH level was first set at 0% to dry the sample completely, then increased to 30% -90%. Film thickness was measured and recorded after equilibrium state was reached at certain RH for roughly 5 min. With this method, thickness of thin film at different RH level was measured without changing probed area of samples, rendering higher accuracy.

3.4.8 Water uptake measured by quartz crystal microbalance (QCM)

Methylated P2VP and xP2VP samples were first fabricated on 5 MHz Au quartz crystal following the sample procedures described before. Then the crystal was placed into the mini chamber of QCM (Gamry eQCM 10M) with a small piece of tape (*ca*. 2 mm^2) attached to the overlapping area on the backside to resist ringing effect of the quartz crystal as suggested by Gamry technician. RH of the working chamber, in which water uptake was measured, was controlled by connecting Linkam RH95 Humidity Controller to the inlet of QCM chamber. Thermal circulator (Huber mini chiller 300) was used during the measurement to keep the temperature stable at 25 °C, preventing frequency drift. The samples were all equilibrated for 10 min at each RH level before changing to the next. The change of mass due to water absorption was calculated by frequency difference as equation S2,

$$\frac{\Delta m}{\Delta f} = 4.24\, ng/Hz \tag{3.2}$$

where Δm is the water uptake of polymer thin film, Δf is the frequency shift due to change of mass measured by QCM, and 4.24 ng/Hz is coefficient determined by the properties of the chosen crystal. At least three samples were prepared and measured for each material for better statistics.

3.4.9 Ionic conductivity determined by electrochemical impedance spectroscopy (EIS)

The impedance of methylated thin film was measured on IDEs using Gamry Reference 600+ potentiostat. Polymer coated on the two pads of IDEs were wiped off by commercial Q-tip to ensure good electrical contact between pads and clips that connected to the potentiostat. IDEs were then placed inside humidity chamber (ESPEC SH-242) with temperature where temperature and relative humidity can be controlled. The polymer thin film was equilibrated for 10 min before each impedance measurement. A 50 mV AC potential was applied at frequencies ranging from 1 Hz to 1 MHz. Then the impedance data was fit to equivalent circuit model using Gamry Echem Analyst software.

3.4.10 Measurements of glass transition temperature via Differential Scanning Calorimetry (DSC)

Aluminum pans and lids (Tzero Pans) were first weighted on microbalance. Then weight of different polymers (5-10 mg) was measured and sealed into the pans (Tzero DSC Sample Encapsulation Press). Three sets of glass transition temperature of polymers were measured on the DSC tool (TA Instruments Discovery 2500). For unfunctionalized polymers, namely P2VP and 4 xP2VPs, the samples were thermally cross-linked if possible. The samples were equilibrated at 50 °C for 5 min to eliminate thermal history and then heated to 250°C at a rate of 10 °C min^{-1} and equilibrated for another 5 min followed by a cooling cycle at 10 °C min^{-1} to − 90°C. For dry functionalized polymers, the samples were first thermally cross-linked if possible. Then the samples were transferred into pans and functionalized by soaking with calculated amount of liquid methyl iodide for 24 hours. The samples were equilibrated at 50 °C for 5 min and then heated to 150°C (to fully eliminate water associated with polymers) at a rate of 10 °C min^{-1} and equilibrated for another 5 min followed by a cooling cycle at 10 °C min^{-1} to − 90°C. For hydrated functionalized polymer, the samples were first cross-linked and functionalized. After that, the samples were placed inside the RH chamber for 30 min with RH set at 80%, where the pans were sealed, to ensure the polymers were at a specific RH level. The samples were equilibrated at 50 °C for 5 min and then heated to 90°C (to prevent loss of water associated with the polymers) at a rate of 10 °C min^{-1} and equilibrated for another 5 min followed by a cooling cycle at 10 °C min^{-1} to − 90°C. The glass transition temperature (T_g) was measured on the second heating cycle for all samples.

3.4.11 Calculation of swelling ratio

Swelling ratio is defined as fractional increase in the volume of hydrophilic thin film due to water absorption. Since the thin film was confined in the plane of silicon wafer, we chose thickness/height of the film to perform the calculation. Swelling ratio can be calculated by equation S3,

$$\text{swelling ratio} = (h - h_M)/h_M \tag{3.3}$$

where h is the thickness of methylated thin film at different RH, h_M is the thickness of corresponding methylated thin film at 0 RH.

3.4.12 Calculation of hydration number

Hydration number λ is defined as number of water molecules absorbed per 2VP/NMP$^+$ cation. Mole of water absorbed can be calculated by the weight of absorbed water as equation S4,

$$n_w = \Delta m/M_w \tag{3.4}$$

where n_w is the mole of water absorbed in the thin film, Δm is the weight of absorbed water in the thin film, and M_w is the molar mass of water. Mole of 2VP/NMP$^+$ can be obtained by equation S5,

$$n_{\mathrm{2VP/NMP+}} = f\rho S h_0/M_{2VP} \tag{3.5}$$

where $n_{\mathrm{2VP/NMP+}}$ is the mole of 2VP/NMP$^+$ cation, f is the degree of methylation, ρ is the density of unfunctionalized P2VP, S is the overlapping area of electrodes on the two sides of QCM crystal, h_0 is the thickness of unfunctionalized P2VP thin film, and M_{2VP} is the molar mass of the 2VP monomer. Then hydration number λ can be derived as equation S6,

$$\lambda = n_w/n_{\mathrm{2VP/NMP+}} \tag{3.6}$$

where λ is the hydration number of the methylated thin film as a specific RH level.

3.4.13 Calculation of water uptake

The water uptake of the thin film was calculated as a function of RH. The water uptake of the membranes was calculated in weight percent (WU%) using the following equation:

$$WU = \frac{W_{wet} - W_{dry}}{W_{dry}} \times 100\% \tag{3.7}$$

where W_{wet} and W_{dry} are the weights of the wet and dry thin films, respectively.

3.4.14 Calculation of water concentration

Water concentration is defined as weight of water per unit volume in the hydrated polymer electrolytes. It can be calculated by equation S8,

$$c = \Delta\mathrm{m}/Sh \tag{3.8}$$

where c is the water concentration (g/cm^3) in the polymer electrolytes, Δm is the weight of water absorbed, S is the overlapping area of electrodes on the two sides of QCM crystal, and h is the thickness of methylated polymer thin film at different RH levels.

3.5 References

(1) Hickner, M. A.; Ghassemi, H.; Kim, Y. S.; Einsla, B. R.; McGrath, J. E. Alternative Polymer Systems for Proton Exchange Membranes (PEMs). *Chem. Rev.* **2004**, *104* (10), 4587–4611. https://doi.org/10.1021/cr020711a.

(2) Jinnouchi, R.; Kudo, K.; Kodama, K.; Kitano, N.; Suzuki, T.; Minami, S.; Shinozaki, K.; Hasegawa, N.; Shinohara, A. The Role of Oxygen-Permeable Ionomer for Polymer Electrolyte Fuel Cells. *Nat. Commun.* **2021**, *12* (1). https://doi.org/10.1038/s41467-021-25301-3.

(3) Liu, D.; Kyriakides, S.; Case, S. W.; Lesko, J. J.; Yanxiang, L. I.; Mcgrath, J. E. Tensile Behavior of Nafion and Sulfonated Poly(Arylene Ether Sulfone) Copolymer Membranes and Its Morphological Correlations. *J. Polym. Sci. Part B Polym. Phys.* **2006**, *44* (10), 1453–1465. https://doi.org/10.1002/polb.20813.

(4) Tang, H.; Peikang, S.; Jiang, S. P.; Wang, F.; Pan, M. A Degradation Study of Nafion Proton Exchange Membrane of PEM Fuel Cells. *J. Power Sources* **2007**, *170* (1), 85–92.

https://doi.org/10.1016/j.jpowsour.2007.03.061.

(5) Fernandes, A. C.; Ticianelli, E. A. A Performance and Degradation Study of Nafion 212 Membrane for Proton Exchange Membrane Fuel Cells. *J. Power Sources* **2009**, *193* (2), 547–554. https://doi.org/10.1016/j.jpowsour.2009.04.038.

(6) Han, J.; Zhu, L.; Pan, J.; Zimudzi, T. J.; Wang, Y.; Peng, Y.; Hickner, M. A.; Zhuang, L. Elastic Long-Chain Multication Cross-Linked Anion Exchange Membranes. *Macromolecules* **2017**, *50* (8), 3323–3332. https://doi.org/10.1021/acs.macromol.6b01140.

(7) Gu, S.; Cai, R.; Luo, T.; Chen, Z.; Sun, M.; Liu, Y.; He, G.; Yan, Y. A Soluble and Highly Conductive Ionomer for High-Performance Hydroxide Exchange Membrane Fuel Cells. *Angew. Chemie - Int. Ed.* **2009**, *48* (35), 6499–6502. https://doi.org/10.1002/anie.200806299.

(8) Hren, M.; Božič, M.; Fakin, D.; Kleinschek, K. S.; Gorgieva, S. Alkaline Membrane Fuel Cells: Anion Exchange Membranes and Fuels. *Sustain. Energy Fuels* **2021**, *5* (3), 604–637. https://doi.org/10.1039/d0se01373k.

(9) Tsai, T. H.; Ertem, S. P.; Maes, A. M.; Seifert, S.; Herring, A. M.; Coughlin, E. B. Thermally Cross-Linked Anion Exchange Membranes from Solvent Processable Isoprene Containing Ionomers. *Macromolecules* **2015**, *48* (3), 655–662. https://doi.org/10.1021/ma502362a.

(10) Wang, J.; Gu, S.; Xiong, R.; Zhang, B.; Xu, B.; Yan, Y. Structure–Property Relationships in Hydroxide-Exchange Membranes with Cation Strings and High Ion-Exchange Capacity. *ChemSusChem* **2015**, *8* (24), 4229–4234. https://doi.org/https://doi.org/10.1002/cssc.201501035.

(11) Lee, W.-H.; Park, E. J.; Han, J.; Shin, D. W.; Kim, Y. S.; Bae, C. Poly(Terphenylene) Anion Exchange Membranes: The Effect of Backbone Structure on Morphology and Membrane Property. *ACS Macro Lett.* **2017**, *6* (5), 566–570. https://doi.org/10.1021/acsmacrolett.7b00148.

(12) Xue, Z.; He, D.; Xie, X. Poly(Ethylene Oxide)-Based Electrolytes for Lithium-Ion Batteries. *J. Mater. Chem. A* **2015**, *3* (38), 19218–19253. https://doi.org/10.1039/c5ta03471j.

(13) Zardalidis, G.; Ioannou, E.; Pispas, S.; Floudas, G. Relating Structure, Viscoelasticity, and Local Mobility to Conductivity in PEO/LiTf Electrolytes. *Macromolecules* **2013**, *46* (7), 2705–2714. https://doi.org/10.1021/ma400266w.

(14) Diederichsen, K. M.; Buss, H. G.; McCloskey, B. D. The Compensation Effect in the Vogel–Tammann–Fulcher (VTF) Equation for Polymer-Based Electrolytes. *Macromolecules* **2017**, *50* (10), 3831–3840. https://doi.org/10.1021/acs.macromol.7b00423.

(15) Chu, W.; Webb, M. A.; Deng, C.; Colón, Y. J.; Kambe, Y.; Krishnan, S.; Nealey, P. F.; de Pablo, J. J. Understanding Ion Mobility in P2VP/NMP+I– Polymer Electrolytes: A Combined Simulation and Experimental Study. *Macromolecules* **2020**, *53* (8), 2783–2792. https://doi.org/10.1021/acs.macromol.9b02329.

(16) Ertem, S. P.; Tsai, T. H.; Donahue, M. M.; Zhang, W.; Sarode, H.; Liu, Y.; Seifert, S.; Herring, A. M.; Coughlin, E. B. Photo-Cross-Linked Anion Exchange Membranes with Improved Water Management and Conductivity. *Macromolecules* **2016**, *49* (1), 153–161.

https://doi.org/10.1021/acs.macromol.5b01784.

(17) Wu, L.; Pan, Q.; Varcoe, J. R.; Zhou, D.; Ran, J.; Yang, Z.; Xu, T. Thermal Crosslinking of an Alkaline Anion Exchange Membrane Bearing Unsaturated Side Chains. *J. Memb. Sci.* **2015**, *490*, 1–8. https://doi.org/10.1016/j.memsci.2015.04.046.

(18) Srebnik, S.; Pusara, S.; Dekel, D. R. Effect of Carbonate Anions on Quaternary Ammonium-Hydroxide Interaction. *J. Phys. Chem. C* **2019**, *123* (26), 15956–15962. https://doi.org/10.1021/acs.jpcc.9b03131.

(19) Zelovich, T.; Simari, C.; Nicotera, I.; Dekel, D. R.; Tuckerman, M. E. The Impact of Carbonation on Hydroxide Diffusion in Nano-Confined Anion Exchange Membranes. *J. Mater. Chem. A* **2022**, *10* (20), 11137–11149. https://doi.org/10.1039/D2TA00830K.

(20) Stutz, H.; Illers, K.-H.; Mertes, J. A Generalized Theory for the Glass Transition Temperature of Crosslinked and Uncrosslinked Polymers. *J. Polym. Sci. Part B Polym. Phys.* **1990**, *28* (9), 1483–1498. https://doi.org/https://doi.org/10.1002/polb.1990.090280906.

(21) Panayiotou, C. G. Glass Transition Temperatures in Polymer Mixtures. *Polym. J.* **1986**, *18* (12), 895–902. https://doi.org/10.1295/polymj.18.895.

(22) Mandal, M.; Huang, G.; Kohl, P. A. Highly Conductive Anion-Exchange Membranes Based on Cross-Linked Poly(Norbornene): Vinyl Addition Polymerization. *ACS Appl. Energy Mater.* **2019**, *2* (4), 2447–2457. https://doi.org/10.1021/acsaem.8b02051.

(23) Chen, W.; Mandal, M.; Huang, G.; Wu, X.; He, G.; Kohl, P. A. Highly Conducting Anion-Exchange Membranes Based on Cross-Linked Poly(Norbornene): Ring Opening Metathesis Polymerization. *ACS Appl. Energy Mater.* **2019**, *2* (4), 2458–2468. https://doi.org/10.1021/acsaem.8b02052.

(24) Boldini, A.; Porfiri, M. A Non-Ideal Solution Theory for the Mechanics and Electrochemistry of Charged Membranes. *npj Comput. Mater.* **2022**, *8* (1), 144. https://doi.org/10.1038/s41524-022-00827-2.

(25) Son, C. Y. W. Z.-G. Ion Transport in Small-Molecule and Polymer Electrolytes. *J. Chem. Phys.* **2020**, *153* (10), 100903. https://doi.org/10.1063/5.0016163.

(26) Liu, C.; Sharon, D.; Grocke, G.; Patel, S. N.; Bennington, P.; Nealey, P. F.; Burnett, V. F.; Dong, B. X.; Kambe, Y.; Dolejsi, M. Interrogation of Electrochemical Properties of Polymer Electrolyte Thin Films with Interdigitated Electrodes. *J. Electrochem. Soc.* **2018**, *165* (16), H1028–H1039. https://doi.org/10.1149/2.0291816jes.

(27) Sharon, D.; Bennington, P.; Dolejsi, M.; Webb, M. A.; Dong, B. X.; De Pablo, J. J.; Nealey, P. F.; Patel, S. N. Intrinsic Ion Transport Properties of Block Copolymer Electrolytes. *ACS Nano* **2020**, *14* (7), 8902–8914. https://doi.org/10.1021/acsnano.0c03713.

(28) Kambe, Y.; Arges, C. G.; Czaplewski, D. A.; Dolejsi, M.; Krishnan, S.; Stoykovich, M. P.; De Pablo, J. J.; Nealey, P. F. Role of Defects in Ion Transport in Block Copolymer Electrolytes. *Nano Lett.* **2019**, *19* (7), 4684–4691. https://doi.org/10.1021/acs.nanolett.9b01758.

(29) Dong, B. X.; Bennington, P.; Kambe, Y.; Sharon, D.; Dolejsi, M.; Strzalka, J.; Burnett, V.

F.; Nealey, P. F.; Patel, S. N. Nanothin Film Conductivity Measurements Reveal Interfacial Influence on Ion Transport in Polymer Electrolytes. *Mol. Syst. Des. Eng.* **2019**, *4* (3), 597–608. https://doi.org/10.1039/c9me00011a.

(30) Ye, Y.; Sharick, S.; Davis, E. M.; Winey, K. I.; Elabd, Y. A. High Hydroxide Conductivity in Polymerized Ionic Liquid Block Copolymers. *ACS Macro Lett.* **2013**, *2* (7), 575–580. https://doi.org/10.1021/MZ400210A/SUPPL_FILE/MZ400210A_SI_001.PDF.

(31) Salvatore, D. A.; Gabardo, C. M.; Reyes, A.; O'Brien, C. P.; Holdcroft, S.; Pintauro, P.; Bahar, B.; Hickner, M.; Bae, C.; Sinton, D.; Sargent, E. H.; Berlinguette, C. P. Designing Anion Exchange Membranes for CO2 Electrolysers. *Nat. Energy* **2021**, *6* (4), 339–348. https://doi.org/10.1038/s41560-020-00761-x.

(32) Kim, J.; Koo, B.; Lim, J.; Jeon, J.; Lim, C.; Lee, H.; Kwak, K.; Cho, M. Dynamic Water Promotes Lithium-Ion Transport in Superconcentrated and Eutectic Aqueous Electrolytes. *ACS Energy Lett.* **2022**, *7* (1), 189–196. https://doi.org/10.1021/acsenergylett.1c02012.

(33) Zhu, L.; Zimudzi, T. J.; Wang, Y.; Yu, X.; Pan, J.; Han, J.; Kushner, D. I.; Zhuang, L.; Hickner, M. A. Mechanically Robust Anion Exchange Membranes via Long Hydrophilic Cross-Linkers. *Macromolecules* **2017**, *50* (6), 2329–2337. https://doi.org/10.1021/acs.macromol.6b01381.

(34) Chen, X. C.; Wong, D. T.; Yakovlev, S.; Beers, K. M.; Downing, K. H.; Balsara, N. P. Effect of Morphology of Nanoscale Hydrated Channels on Proton Conductivity in Block Copolymer Electrolyte Membranes. *Nano Lett.* **2014**, *14* (7), 4058–4064. https://doi.org/10.1021/nl501537p.

(35) Shrivastava, U. N.; Zhegur-Khais, A.; Bass, M.; Willdorf-Cohen, S.; Freger, V.; Dekel, D. R.; Karan, K. Water Content and Ionic Conductivity of Thin Films of Different Anionic Forms of Anion Conducting Ionomers. *J. Phys. Chem. C* **2020**, *124* (43), 23469–23478. https://doi.org/10.1021/acs.jpcc.0c04278.

CHAPTER 4

ROLE OF INTERFACE ON ION TRANSPORT IN HYDRATED BLOCK COPOLYMER ELECTROLYTES

Abstract

The relationship between interface, confinement, and the ion transport in BCEs was investigated. We chose polystyrene-b-poly(2 vinyl pyridine) with different molecular weights to tune the volume fraction of the interface by both changing the domain size and segregation strength. Parallel lamellae of the BCEs consisted of single grain structure were fabricated on the silicon substrate, which alleviates the concerns on ion transport arising from the grain boundary or defects. We used X-ray reflectivity to experimentally determine the volume fraction of interface for each BCE. Thin film measurements of water uptake and swelling ratio indicate the higher water concentration in lower molecular weight material, which can be ascribed to the higher volume fraction of interface. Molecular dynamic simulation provides insight into the role of interface controlling the swelling of the BCE. Higher free volume exists in the interface region, which can accommodate more water compared to the bulk of the conducting domain without experiencing excessive swelling, which enable fast ion transport due to higher water concentration.

4.1 Introduction

Solid polymer electrolytes (SPEs) have gained prominence for their potential in fuel cell performance.[1,2] Nafion, a perfluorinated sulfonic acid (PFSA)-based membrane, is considered a standard in proton exchange membrane fuel cells (PEMFCs) due to its superior conductivity, chemical stability, and mechanical properties.[3–5] However, the acidic environment in which PEMs operate limits the choice of catalysts to precious metals such as platinum.[6,7] As an alternative, anion exchange membrane fuel cells (AEMFCs) operate in an alkaline environment, facilitating oxygen reduction and fuel oxidation reactions and permitting the use of low-cost, non-noble metal catalysts.[8,9] Despite this, AEMs typically exhibit lower ionic conductivity than PEMs due to the intrinsically lower mobility of OH^-.[8] While increasing the ion exchange capacity (IEC) of AEMs can enhance ionic conductivity, this often leads to dimensional swelling and loss of mechanical integrity due to increased water absorption,[10,11] resulting in defects during fuel cell operation.[12–15]

Block copolymer electrolytes (BCE), however, is an excellent candidate for circumventing the trade-off between mechanical property and ionic conductivity, where microphase separation happens after thermal annealing. The hydrophobic domain provides mechanical properties, and the hydrophilic ionic domain gives rise to ion conducting property, which enables independently modification of both domains. Many studies have reported excellent conductivity of BCE compared to homopolymer analog, while the actual mechanism for the conductivity enhancement is unclear.[16,17] For example, the Winey group reported higher hydroxide conductivity of poly (ionic liquid) at high RH over a range of temperatures.[16] They speculate that the higher conductivity might be due to confinement effect of the nanostructure formed due to phase separation. Balsara et al. studied the substructure of water confined in the nanodomains of BCEs.[18] They found that when the size of the domain decreases to sub-10 nm, the substructure of water will disappear, which might account for the higher conductivity in lower molecular weight BCEs. Additionally, The Segalman group has studied the poly(ionic liquid) of homo-polymer and block copolymer and they concluded that the confinement in the block copolymer has been shown to improve the connectivity of the hydrogen-bonding network, leading to a dramatic increase in proton conductivity.[17]

On the other hand, the role of interface between blocks of the BCE has gain interest in the anhydrous polymer electrolytes field. When the BCEs undergo phase separation, the interface between the two blocks exist due to the covalently connected nature of the blocks, and the sharpness will depend on the segregation strength, namely χN, which is the product of the Flory-Huggins interaction parameter and degree of polymerization. Researchers found that the more interface exist in the system, the lower efficiency the ion transport would be. For example, the Nealey group has demonstrated that the interfacial region almost serves as non-conducting part in the polystyrene-b-poly(ethylene oxide) materials and this region decreases when more salt was added as the interaction parameter increases.[19] They observed that even a small fraction of the non-conducting part in the interface would disrupt the connectivity of the solvation sites. Similar founding has been made by the Park group, where the highest conductivity was measured for poly(styrenesulfonate-b-methylbutylene) with the sharpest interface, tuned by different types of ionic liquids.[20] However, this mechanism might not apply to the water-assisted transport of ions in hydrated polymer electrolytes.

In this work, we investigate the relationship between interface, confinement, and the ion transport in BCEs. We chose polystyrene-b-poly(2 vinyl pyridine) with different molecular weights to tune the volume fraction of the interface by both changing the domain size and segregation strength. Parallel lamellae of the BCEs consisted of single grain structure were fabricated on the silicon substrate, which alleviates the concerns on ion transport arising from the grain boundary or defects. We used X-ray reflectivity to experimentally determine the volume fraction of interface for each BCE. Thin film measurements of water uptake and swelling ratio indicate the higher water concentration in lower molecular weight material, which can be ascribed to the higher volume fraction of interface. Molecular dynamic simulation provides insight into the role of interface controlling the swelling of the BCE. Higher free volume exists in the interface region, which can accommodate more water compared to the bulk of the conducting domain without experiencing excessive swelling, which enable fast ion transport due to higher water concentration. This study combines thin film study of BCEs with molecular dynamics simulation tool to construct a deep understanding of how interface affect the confinement of water inside the BCEs, which leads to the higher conductivity.

4.2 Results and Discussion

4.2.1 Fabrication of parallel lamellae of PS-b-P2VP/NMP$^+$I$^-$ on IDEs

Figure 4.1 illustrates the device fabrication processes. We first fabricated platinum interdigitated electrodes (IDEs) on a silicon wafer (see Figure 4.1a for electrode geometry). The specifics of our microfabrication processes align with those detailed in earlier studies.[19,21] Subsequently, a 5 nm layer of cross-linkable Polystyrene (x-PS) was deposited onto the IDEs, followed by spin-coating a PS-b-P2VP solution in toluene. Importantly, our block copolymer (BCP) achieves parallel lamellae upon thermal annealing when its thickness equals an integer multiple of L_0 (BCP's domain spacing). We characterized three BCPs of differing molecular weight (MW) (13k-13k, 25k-25k, and 57k-57k) using size exclusion chromatography equipment (Figure 4.2), demonstrating a lamellar morphology post-phase separation by small-angle X-ray scattering (Figure 4.3). Following characterization, we subjected the samples to a vapor infiltration reaction, transforming BCPs into block copolymer electrolytes (BCEs) through 24-hour exposure to methyl iodide (MeI) vapor. Figure 4.1b outlines the reaction scheme. The MeI selectively reacts with the P2VP block's pyridine group, partly converting the 2VP unit into a quaternary ammonium cation (NMP$^+$) and a free iodide anion (I$^-$).[22] Notably, the P2VP/NMP$^+$I$^-$ domain conducts, with I$^-$ serving as the conducting ion when hydrated, while the PS domain is non-conducting.

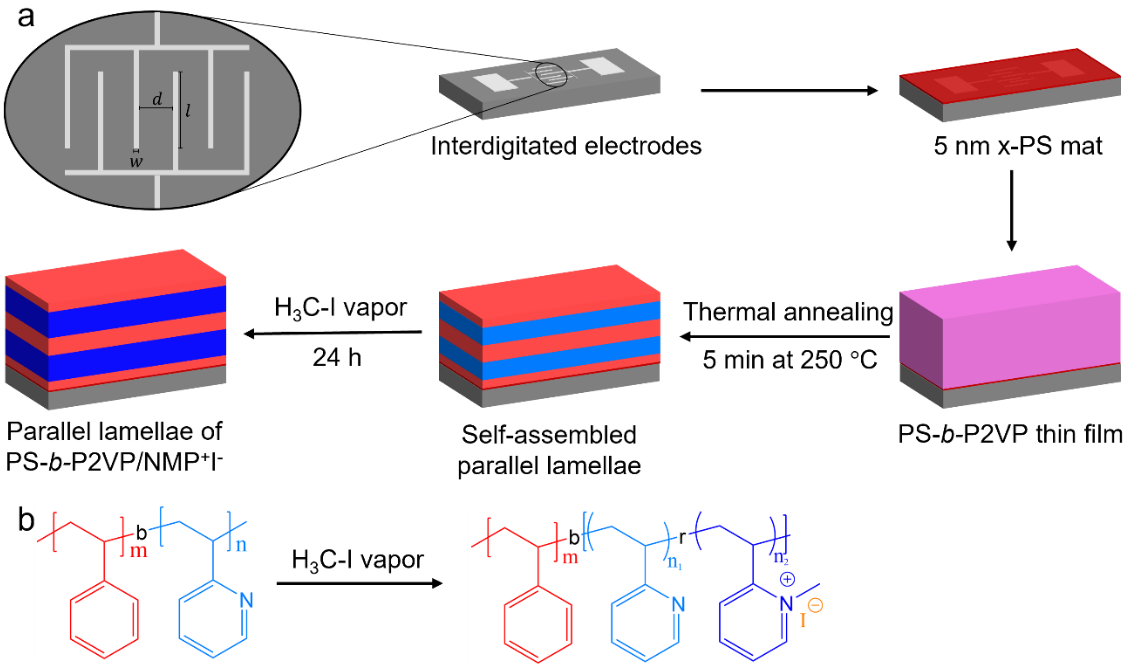

Figure 4.1. (a) Top-down view of IDEs and schematic process flow for making symmetric self-assembled BCE films parallel to the IDEs surface. (b) Reaction scheme of preparing PS-b-P2VP/NMP$^+$I$^-$ BCE.

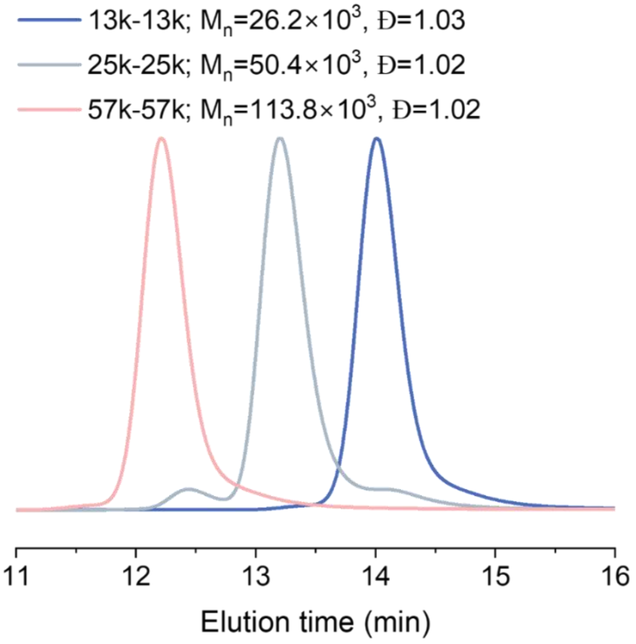

Figure 4.2. The representative SEC profiles of 13k-13k, 25k-25k, and 57k-57k PS-b-P2VP in THF with molecular weight and dispersity presented.

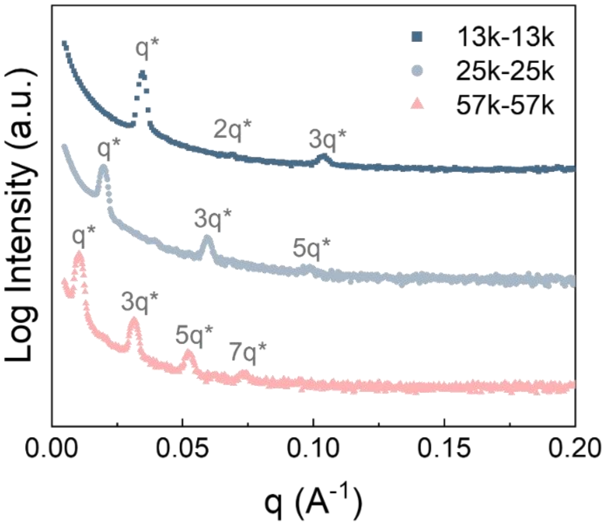

Figure 4.3. SAXS profiles of PS-P2VP block copolymers with molecular weights of 13k-13k, 25k-25k, and 57k-57k. Samples were annealed at 210 °C for 24 h.

After sample fabrication, we applied Electrochemical Impedance Spectroscopy (EIS) to gauge the impedance of the BCE thin film. The conductivity (σ) can be computed using equation (1):

$$\sigma = \frac{d}{(N-1)lR_{film}t} \tag{1}$$

where d signifies the electrode separation distance, N represents the total electrode teeth number, l denotes the overlapping electrode teeth length, R_{film} is the film resistance derived from the Nyquist plot by EIS, and t is the film thickness.[21]

Our work relies heavily on the resilience of the BCE's parallel lamellar structure. Despite the lamellar morphology exhibited by the neutral BCP, the introduction of MeI and subsequent hydration could potentially alter the phase behavior of block copolymers, as the Flory-Huggins interaction parameters and volume fraction of one block are subject to change. Consequently, it is crucial to ascertain the persistence of the BCP's lamellar structure following its conversion to BCE.

Figure 4.4 showcases optical and AFM height images of the self-assembled samples, using 57k-57k as a representative example. By modulating the film thickness, we prepared hold-islands and flat films of annealed BCP, where 1.75 L_0 formed holes, 2 L_0 resulted in a flat film, and 2.25 L_0 created islands.[23] Optical images provided a comparative analysis of the same area pre- and post-MeI functionalization, as highlighted by pink circles in Figure 4.4a,b and Figure 4.4e,f. This revealed no lateral structural changes in the holes and islands. However, a significant color shift was evident in the hole-islands and flat film, indicating a thickness alteration post-P2VP block functionalization. This hypothesis was further supported by AFM height profiles of the hole-islands, which documented a step height increase from approximately 52 nm to roughly 60 nm (Figure 4.4a,b and Figure 4.4e,f). Remarkably, the parallel lamellae flat film (2 L_0) remained mostly unchanged, displaying only a minor increase in surface roughness after the P2VP block had been converted to hydrophilic P2VP/NMP$^+$I$^-$ (Figure 4.4c,d). It's important to note that the functionalized sample measurements were conducted under ambient conditions, permitting the hydrophilic P2VP/NMP$^+$I$^-$ domain to swell due to absorption of airborne water molecules. Due to experimental constraints, we were not capable to control the relative humidity (RH). Nevertheless, these results affirm that the parallel lamellae structure remains intact following the introduction of MeI and water molecules, with expansion restricted to the direction perpendicular to the substrate.

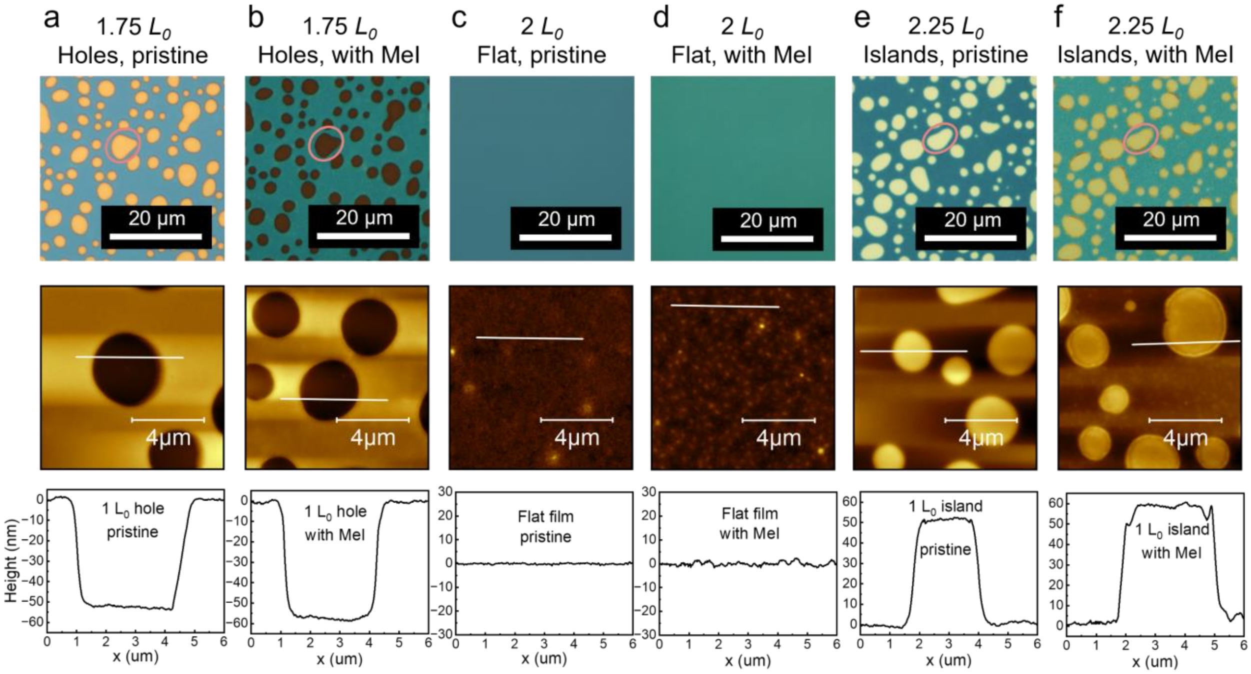

Figure 4.4. Optical images and AFM height images with corresponding height profiles (top to bottom) of (a) 1.75 L_0 holes (pristine), (b) 1.75 L_0 holes (with MeI), (c) 2 L_0 flat film (pristine), (d) 2 L_0 flat film (with MeI), (e) 2.25 L_0 islands (pristine), and (f) 2.25 L_0 islands (with MeI) of self-assembled BCP (57k-57k). Pink circles in the optical images are for comparison of the microstructure of hole-islands between pristine and functionalized self-assembled BCP. White solid lines in the AFM images indicate the linecuts for the corresponding height profiles.

4.2.2 Water absorption and swelling behavior of BCP thin films

Hydrophilic P2VP/NMP$^+$I$^-$ domain in BCEs and homopolymer thin film absorbs water molecule and swell significantly with thickness changing as a function of relative humidity (RH) (**Figure 4.5**). All self-assembled BCEs for water uptake and swelling ratio measurements have the same number of pitches (2 L_0) with pitch size different from each other as shown in **Figure 4.5**a.

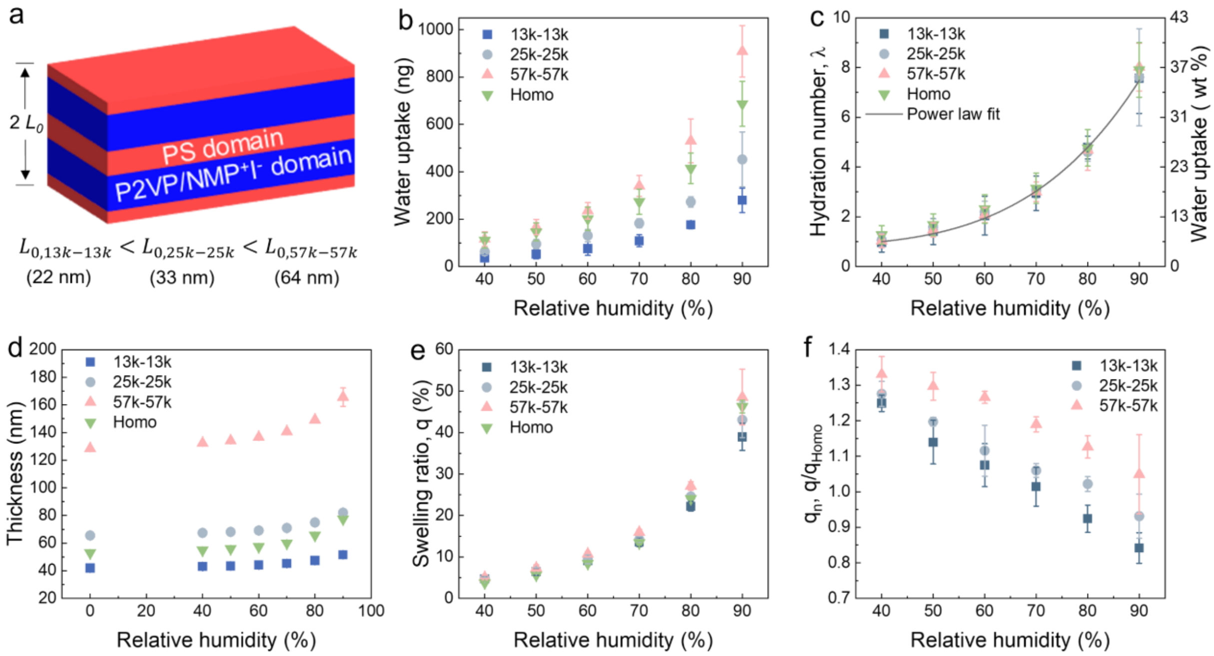

Figure 4.5. Water uptake and swelling ratio results in thin films. (a) Schematic of self-assembled BCEs for water uptake and swelling ratio measurements. (b) Water uptake (ng) of BCEs and homopolymer, and (c) calculated hydration number and corresponding water uptake (wt%) of conducting P2VP/NMP$^+$I$^-$ domain in BCEs and homopolymer as a function of RH. Grey solid curve represents power law fit results. (d) Film thickness of BCEs and homopolymer, (e) swelling ratio, q, of conducting P2VP/NMP$^+$I$^-$ domain in BCEs and homopolymer, and (f) normalized swelling ratio, q_n, of conducting P2VP/NMP$^+$I$^-$ domain in BCEs with respect to homopolymer as a function of RH.

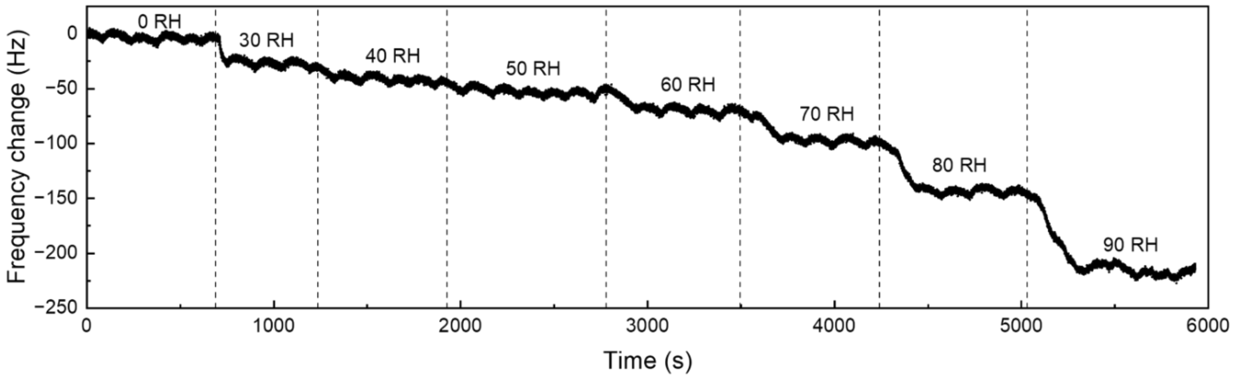

Figure 4.6. Step change of frequency as a function of time under varying RH levels measured by QCM at 25 °C, a representative curve of PS-*b*-P2VP/NMP$^+$I$^-$ (57k-57k, 2 L_0).

To probe thin film water uptake (ng), quartz crystal microbalance (QCM) was employed with the use of humidity control system (see Supporting Information for details). **Figure 4.6** shows a representative step change curve of frequency shift for 57k-57k during QCM measurement as a function of time, with decreased frequency owing to increased water absorption at higher RH. It is shown in **Figure 4.5**b that water uptake in weight (ng) for BCEs of 2 L_0 thickness and homopolymer of certain thickness (*ca.* 53 nm) as a function of RH (note the probing area of QCM crystal is 0.24 cm^2). Water uptake increases significantly for all materials with increasing RH. There is water uptake discrepancy between different materials as different amounts of materials were measured (L_0 is different for BCEs of different MW).

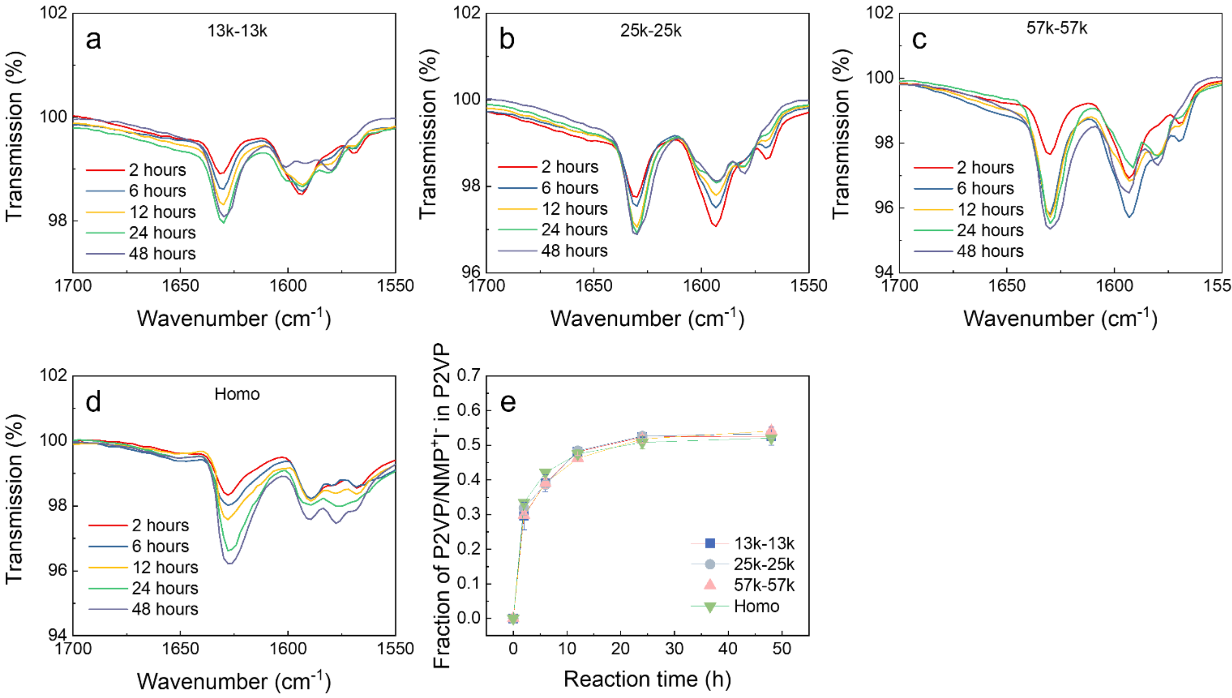

Figure 4.7. FTIR spectra for (a)13k-13k, (b) 25k-25k, (c) 57k-57k, and (d) Homo for different methylation times in the range of 1700-1550 cm^{-1}. (e) Fraction of P2VP/NMP$^+$I$^-$ in the P2VP block as a function of methylation time.

It's worth to note that the degree of functionalization for MeI converting P2VP to P2VP/NMP$^+$I$^-$ is identical (53%) for all BCPs and homopolymer, determined by Fourier-transform infrared spectroscopy (FTIR) measurements (**Figure 4.7**). Ion exchanged capacity (IEC) for BCEs and homopolymer then can be calculated to be 1.92 meq g^{-1} and 2.94 meq g^{-1}, respectively. IEC for the conducting P2VP/NMP$^+$I$^-$ domain in BECs, however, matches IEC of homopolymer due to the same degree of conversion. Therefore, hydration number λ, defined as number of water molecules per ionic site, as well as water uptake in wt% are the same for all conducting P2VP/NMP$^+$I$^-$ domain of BCEs and homopolymer through the RH range, following power law fit as shown in **Figure 4.5**c. The power law fit behavior of the water vapor absorption in this RH range is a combination of Henry's law and water clustering,[24] which has also been reported elsewhere for other materials like polystyrenesulfonate-block-polyethylene-block-polystyrenesulfonate.[25] Since film thickness of 2 L_0 for 13k-13k, 25k-25k, and 57k-57k are different, we picked 13k-13k as example to determine if hydration number is dependent on film thickness by choosing different number of pitches (e.g., 2 L_0 vs. 4 L_0). Hydration numbers of the two thickness overlap well for all RH levels, indicating no thickness-dependence for water uptake property in these films (**Figure 4.8**).

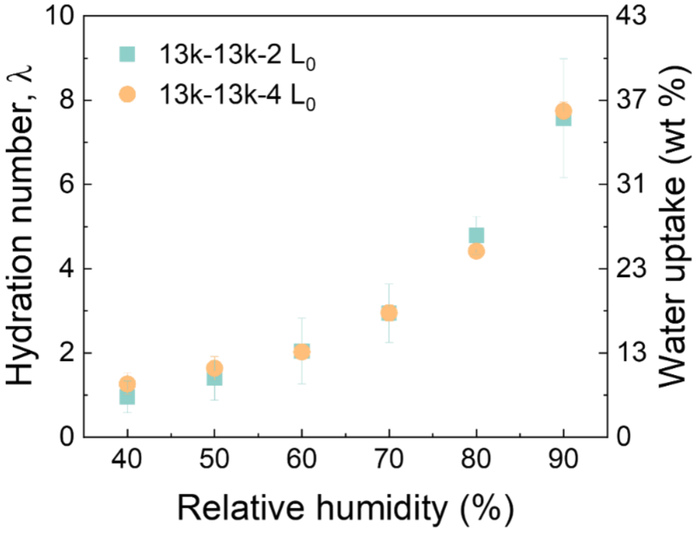

Figure 4.8. Hydration number of 13k-13k BCE with 2 L_0 and 4 L_0 thickness as a function of RH.

To quantify thin film thickness change as a function of RH, *in-situ* ellipsometry measurements were performed on ellipsometer equipped with liquid cell under controlled humidity environment (see Supporting Information). **Figure 4.5**d shows the thickness of BCEs and homopolymer increases with the increase of RH. Like water uptake difference between materials, higher MW material has more thickness change (nm) due to more materials were presented in film of 2 L_0. Note that thickness at dry state (RH = 0) was also reported here for swelling ratio calculation purpose. Swelling ratio in this study was defined as the thickness expansion percentage of the P2VP/NMP$^+$I$^-$ domain (see Supporting Information for calculation details). **Figure 4.5**e shows the swelling ratio of BCEs and homopolymer as a function of RH. Unsurprisingly, swelling ratios for all materials increase dramatically as the RH increases. What is interesting here is the discrepancy of swelling ratios between BCEs at each RH level. **Figure 4.5**f represents the normalized swelling ratio, q_n, of P2VP/NMP$^+$I$^-$ in BCEs with respect to homopolymer as a function of RH, where $q_n = q/q_{Homo}$. For all the RH range studied, higher MW of the BCEs has higher normalized swelling ratio (e.g., $q_{n,57k-57k} > q_{n,25k-25k} > q_{n,13k,13k}$), that is, the hydrophilic domain in higher MW swells to greater extent compared to lower MW. We speculate that the interface between blocks can constrain the volume expansion of hydrophilic P2VP/NMP$^+$I$^-$ domain when water is absorbed. 57k-57k BCE is supposed to have lowest volume fraction of interface than lower MW counterparts due to stronger segregation strength and larger domain size. 57k-57k, therefore, has the least ability to constrain volume expansion and experiences highest swelling ratio. We also measured swelling ratios for 13k-13k of different number of pitches (e.g., 2 L_0 vs. 4 L_0) and it displayed no thickness-dependent swelling ratio property (**Figure 4.9**).

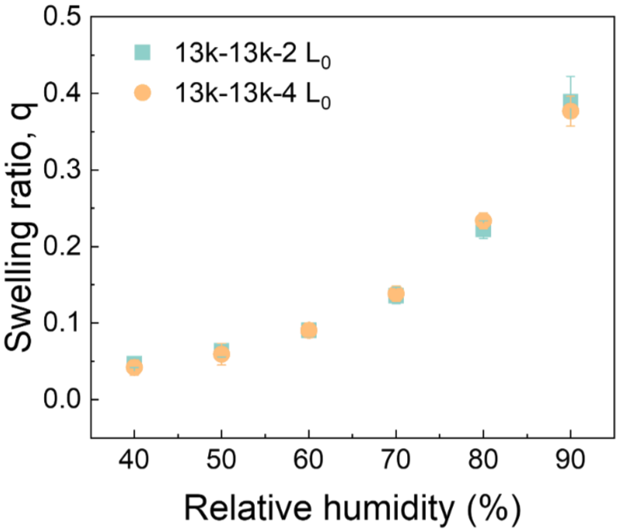

Figure 4.9. Swelling ratio of P2VP/NMP$^+$I$^-$ domain of 13k-13k BCE with 2 *L₀* and 4 *L₀* thickness as a function of RH.

4.2.3 Role of interface in affecting swelling of BCP domain – a combination of experiments and simulation

We further performed X-ray reflectivity measurements to further examine the persistence of parallel lamellar structure and quantify individual layer thickness. XRR is powerful in probing buried nanostructure in block copolymers.[26] First, measurements on parallel lamellae of native BCPs samples were conducted **(Figure 10**a). The experimental reflectivity intensity decay curve for all BCPs overlay simulated data from multilayer model, suggesting the existence of lamellar structure parallel to the substrate. Since density of PS and P2VP domain is approximately the same, fringes of the reflectivity curve for all individual BCP are similar at different q. Parallel lamellae of native BCP samples were then functionalized to BCEs and measured for reflectivity under vacuum, giving rise to the change of fringe pattern due to higher density contrast between layers (**Figure 10**b). It appears that the ordered structures experienced no change after the vapor reaction of P2VP domain with MeI. Lastly, X-ray reflectivity measurements were conducted in ambient condition at certain RH level (ca. 50%) to qualitatively probe if the addition of water affects the structure (**Figure 10**c). Ambient condition was chosen due to limited access to controlled RH system for the X-Ray tool. Like measurements performed in vacuum, experimental data measured in ambient match simulated data significantly, showing the robustness of multilayer model and proving the persistence of nanostructure with the addition of water. These results strongly demonstrate that the method of functionalizing the conducting domain after self-assembly of BCP by vapor infiltration reaction is practicable.

Structural parameters such as thickness of each layer for P2VP (or P2VP/NMP$^+$I$^-$), PS, and interface between blocks were derived from fits for reflectivity as summarized in **Table 4.1**. Unsurprisingly, thickness of hydrophobic PS domain remains constant, regardless of the introduction of MeI vapor and water to the system (e.g., 8.3 nm for 13k-13k), meaning only the 2VP units react with MeI and the corresponding 2VP/NMP$^+$I$^-$ units absorb water. As a result, thickness of P2VP domain increases significantly when converted to P2VP//NMP$^+$I$^-$ domain (e.g., from 8.7 nm to 10.8 nm for 13k-13k) and the thickness of hydrophilic P2VP/NMP+I- domain increase slightly due to water absorption (e.g., from 10.8 nm to 11.1 nm for 13k-13k). It is worth to note that thickness data derived from reflectivity data corresponds well to *in-situ* ellipsometry measurements.

Table 4.1. Individual domain layer thickness in PS-P2VP BCPs and BCEs measured by X-Ray reflectivity and calculated volume fraction of interface in P2VP domain.

Sample	**PS$_{P}$[a] (nm)**	**PS$_{V}$[b] (nm)**	**PS$_{A}$[c] (nm)**	**P2VP$_{P}$ (nm)**	**P2VP$_{V}$ (nm)**	**P2VP$_{A}$ (nm)**	**w_P (nm)**	**w_V (nm)**	**w_A (nm)**	**φ_P**	**φ_V**	**φ_A**
13k-13k	8.3	8.3	8.3	8.7	10.8	11.1	3.6	3.1	2.9	0.41	0.29	0.26
25k-25k	14.4	14.3	14.1	14.2	17.5	18.1	3.5	3.3	3.2	0.25	0.19	0.18
57k-57k	26.2	26.4	26.5	26.6	32.9	33.6	3.4	3.7	3.6	0.13	0.11	0.11

[a] P denotes native, as measurements taken on native unfunctionalized BCPs.
[b] V denotes vacuum, as measurements taken on functionalized BCEs in vacuum condition.
[c] A denotes ambient, as measurements taken on functionalized BCEs in ambient condition.

X-ray reflectivity also allows quantification of interfacial width of BCEs as shown in **Table 4.1**. Interfacial width of all samples was around 3 to 4 nm, with small discrepancy between different MWs. However, interfacial width slightly decreased with functionalization of P2VP domain and subsequent water absorption (except for 57k-57k BCP to BCE) due to increased Flory-Huggins parameter χ. We evaluated the influence that interface had on P2VP domain by calculating the volume fraction of interface φ. Two observations were made: (1) φ decreased significantly after the MeI reaction and decreased slightly when measured in ambient condition, and (2) more importantly, φ in BCEs increased remarkably with smaller domain size ($\varphi_{13k-13k} > \varphi_{25k-25k} > \varphi_{57k-57k}$). As discussed before, P2VP/NMP$^+$I$^-$ domain in 13k-13k expanded the least percentage compared to higher molecular weight ones while having the same hydration number. This is likely attributed to the larger $\varphi_{interface}$ in 13k-13k as demonstrated by X-ray reflectivity.

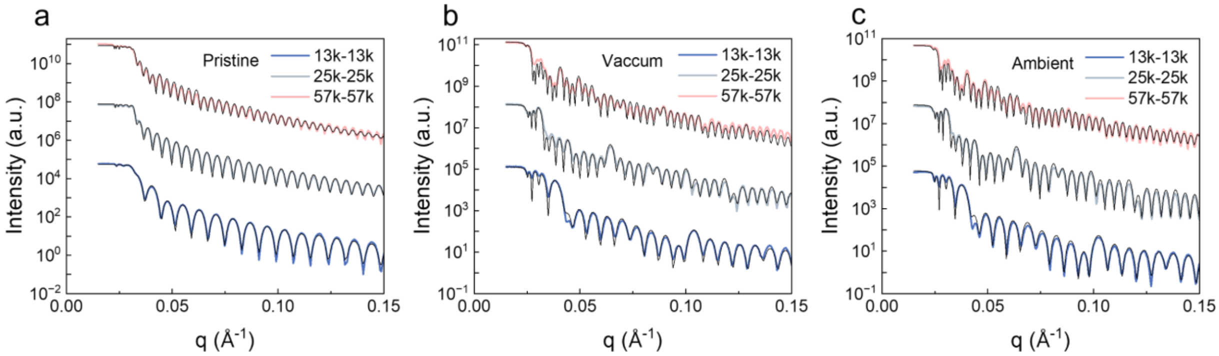

Figure 4.10. X-ray reflectivity measurements of 13k-13k, 25k-25k, and 57k-57k with (a) pristine BCPs, and functionalized BCEs measured in (b) vacuum and (c) ambient condition. Colored lines represent experimental data and black line represent simulated data. The curves are arbitrarily shifted vertically for clarity purpose.

We conducted atomistic molecular dynamics (MD) simulation to gain molecular insight into the impact of water content on ion transport behavior within the conducting domain of a block copolymer (BCP) with varying molecular weights. Specifically, the 13k-13k PS-b-P2VP/NMP+I- system was simulated at different experimental relative humidity levels (30%, 40%, 50%, 60%, and 70%). The analysis was motivated by observed differences in swelling ratio and conductivity among BCP systems with different molecular weights. As discussed previously, we attribute the observed behavioral differences in BCPs with varying molecular weights to the influence of the interface. Consequently, we focus our simulation efforts on elucidating the influence of interfacial effects on the local packing of the conducting domain in the BCP, as well as the solvation structure and dynamics of Iodide ions within the conducting domain. In brief, after preparing and equilibrating the 13k-13k BCP systems at different relative humidity, we ran 200 ns production run at 300°C. Analysis of the simulation trajectories unveiled the impact of the interface on polymer and ion behaviors. Additional details on simulation setup, equilibration, and production runs can be found in the section 4.4.

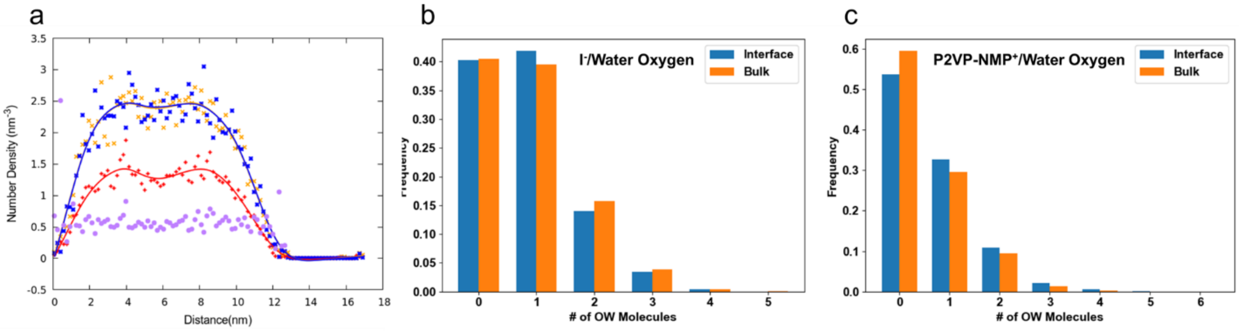

Figure 4.11. Distribution and coordination profiles in 13k-13k PS-b-P2VP/NMP+I- BCP at 30% relative humidity at 300K. (a) Number density profile data of P2VP/NMP+ functional sites (blue squared marks), iodide ions (yellow cross marks), water molecules (red plus marks), and normalized water density profile (i.e., number of water molecules per P2VP/NMP+ functional sites) (purple circled marks). The number density profile data of P2VP/NMP+ functional sites, iodide ions, and water molecules are also smoothed into a natural smoothed spline, plotted in blue, yellow, and red solid lines, respectively. (b) Comparison of coordination motif frequency of iodide ions and water oxygens between the interfacial region and bulk region. (c) Comparison of coordination motif frequency of P2VP/NMP+ functional sites and water oxygens between the interfacial region and bulk region.

Figure 4.11a illustrates the number density profile of P2VP/NMP$^+$ functional sites, iodide ions, and water molecules at 30% relative humidity, room temperature. Additionally, a normalized water density profile representing the amount of water uptake per P2VP/NMP$^+$ functional site is presented. The normalized water density profile remains consistent throughout both the interfacial and bulk regions, indicating that the amount of water per P2VP/NMP$^+$ functional site remains constant across the interface. Therefore, the presence of the interface does not affect water uptake by the P2VP/NMP$^+$ functional sites. We know that water molecules are primarily solvated by P2VP/NMP$^+$ functional sites and iodide ions.[27] Figure 4.11b-c present the frequency of coordination motifs within the first solvation shell cutoff for both the Iodide ion-water molecule and P2VP/NMP$^+$ functional site-water molecule interactions. We defined interfacial species as those residing in the interfacial region for more than 90% of the 200 ns trajectory, whereas bulk species were classified as those predominantly located in the bulk region for more than 90% of the time (Figure 4.12).

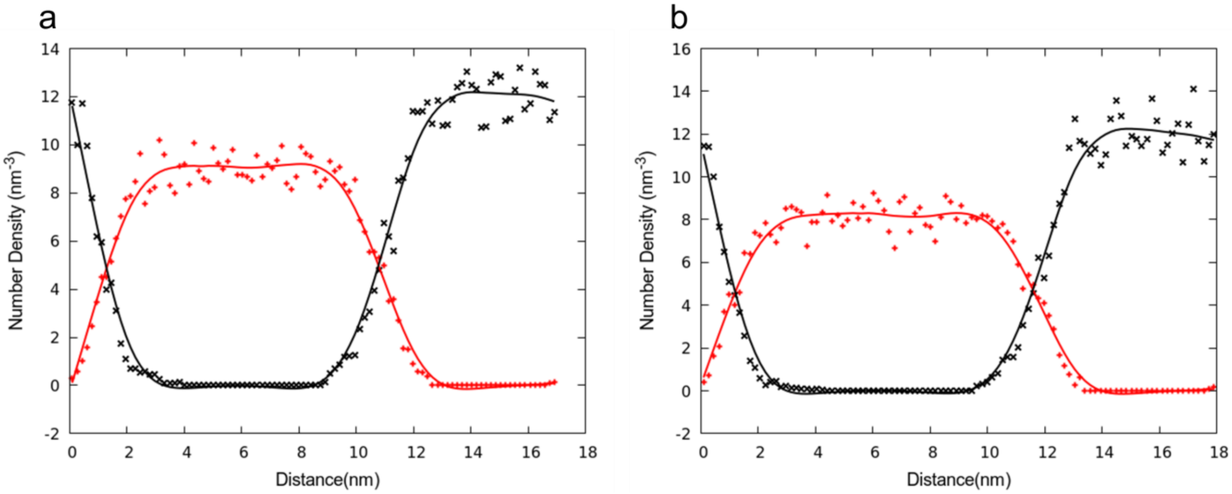

Figure 4.12. Number density profile of PS backbone carbon atoms (black) and P2VP/NMP+ backbone carbon atoms (red) in 13k-13k PS-b-P2VP/NMP+I- BCP systems. The number density profile data are also smoothed into a natural smoothed spline, plotted in solid lines. The x-axis represents the distance in the z-direction, perpendicular to the interface. (a) Number density profile at 30% relative humidity. (b) Number density profile at 70% relative humidity.

It is observed that the differences in motif frequency between the interfacial region and bulk are minimal in both cases. Moreover, we conducted a similar analysis for the system at 70% relative humidity and obtained the same conclusion (Figure 4.13), further supporting the observed consistency in water's solvation behavior across different conditions. Therefore, from our study of the local solvation structure and distribution profile, we can conclude that the presence of interface has no effect in the local solvation of water molecules.

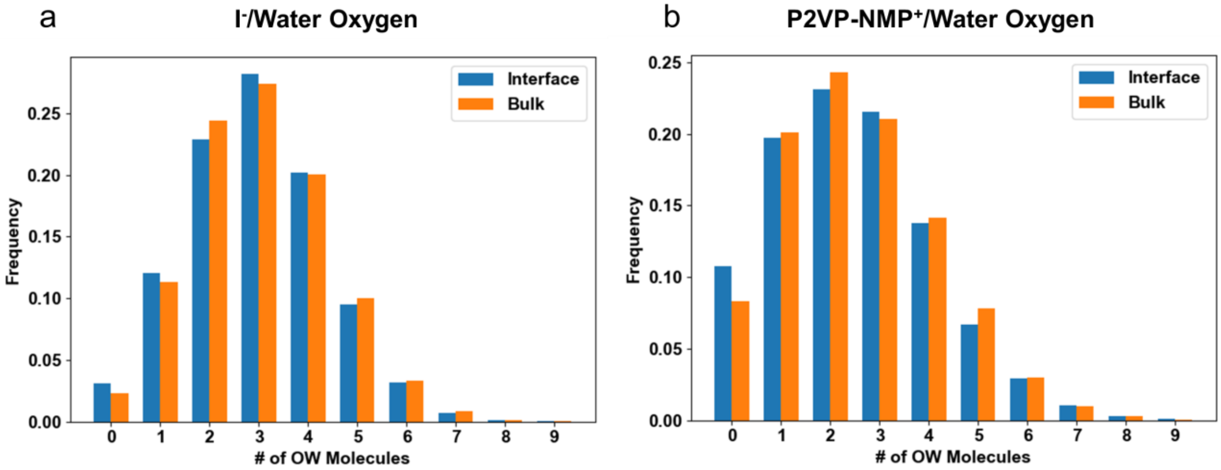

Figure 4.13. Coordination profiles in 13k-13k PS-b-P2VP/NMP+I- BCP at 70% relative humidity at 300K. (a) Comparison of coordination motif frequency of iodide ions and water oxygens between the interfacial region and bulk region. (b) Comparison of coordination motif frequency of P2VP/NMP+ functional sites and water oxygens between the interfacial region and bulk region.

Furthermore, an examination of the coordination motif frequency between the iodide ion and P2VP/NMP$^+$ functional site (Figure 4.14) reveals remarkable similarity between the interface and bulk regions. However, it is notable that the iodide ion exhibits a slightly higher tendency to coordinate with more P2VP/NMP$^+$ functional sites in the bulk, potentially due to the relatively limited availability of P2VP/NMP$^+$ functional sites in the interfacial region.

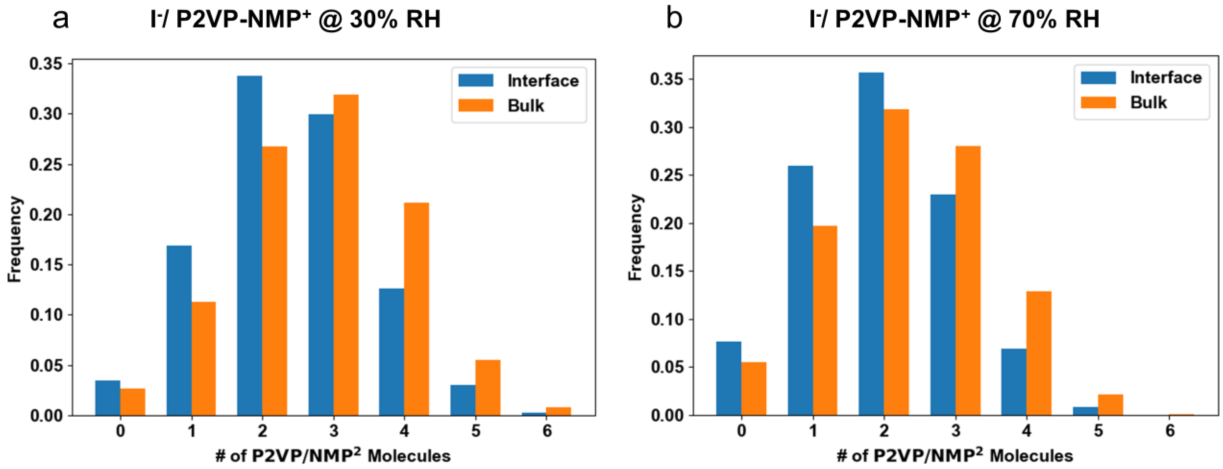

Figure 4.14. Comparison of coordination motif frequency of iodide ions and P2VP/NMP+ functional sites between the interfacial region and bulk region in 13k-13k PS-b-P2VP/NMP+I- BCP at (a) 30% and (b) 70% relative humidity at 300K.

To investigate the impact of the interface on local solvation structures, we compared the radial distribution functions (RDFs) in the block copolymer (BCP) and in P2VP/NMP+I- homopolymer at the same relative humidity (Figure 4.15). Remarkably, the RDFs for iodide ion/water oxygen, iodide ion/P2VP/NMP$^+$ functional site, and P2VP/NMP+ functional site/water oxygen exhibit identical peak positions and first solvation shell cutoffs. This observation suggests that the solvation structure remains consistent in both the homopolymers and BCPs, indicating that the presence of the interface does not significantly alter the local solvation environments.

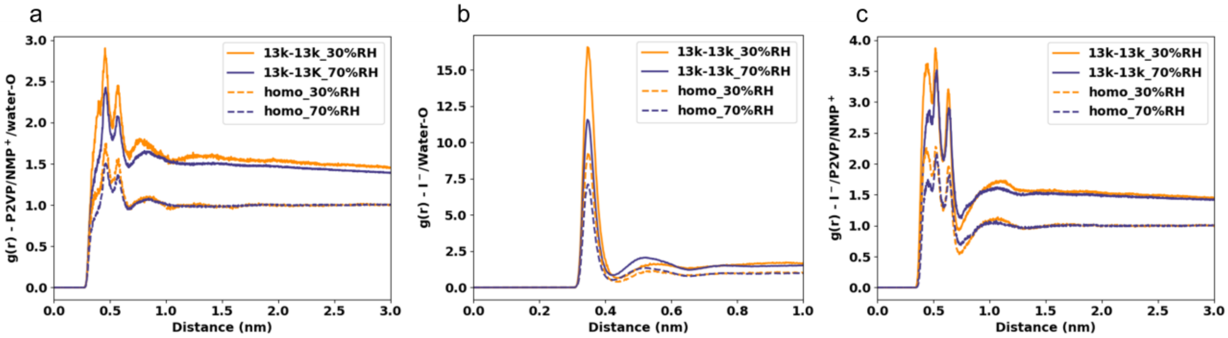

Figure 4.15. Comparison of Radial Distribution Functions (RDFs) in 13k-13k PS-b-P2VP/NMP+I- BCPs (solid lines) and P2VP/NMP+I- homopolymers (dashed lines) at 30% (orange) and 70% (purple) relative humidity. (a) RDF between P2VP/NMP+ functional sites and iodide ions. (b) RDF between iodide ion and water oxygen. (c) RDF between iodide ion and P2VP/NMP+ functional sites.

Our findings demonstrate that the presence of the interface does not impact the local solvation structure. To further investigate the disparity in swelling ratio between the interfacial region and bulk, we focused on examining the differences in polymer local packing between these regions. Figure 4.16a illustrates the bond-vector autocorrelation function (BVAF) for both the interfacial region and the bulk region at relative humidity of 30% and 70%. BVAF provides valuable insights into the dynamics of polymer systems by measuring the rate at which the bond vector adjoining two backbone atoms decorrelates from its initial orientation.[27] Figure 4.16a compares BVAF data for P2VP/NMP^+ backbone bonds in the interfacial and bulk regions. It is evident that both the interfacial and bulk BVAF exhibit faster decay at higher water content. This can be attributed to the plasticizing effect of water molecules on the BCPs, which enhances polymer dynamics and facilitates their movement. However, intriguingly, we find that the interfacial BVAF decays faster than the bulk BVAF at both relative humidity, indicating a faster polymer dynamic at the interface compared to the bulk region. This unexpected result suggests the presence of unique factors influencing polymer dynamics specifically at the interface. To gain further insights, we also determined the free volume per P2VP/NMP^+ functional site in the dry BCP system. This analysis is crucial because, during the insertion of water molecules into the BCP, the available free volume is occupied by water molecules before the BCP begins to swell.[28] In the bulk region, the free volume per P2VP/NMP^+ functional site is calculated to be 0.46 nm^3, whereas at the interfacial region, it is significantly larger at 0.71 nm^3 per P2VP/NMP^+ functional site. This indicates that the free volume in the interfacial region is 52.8% larger compared to the bulk region. Refer to the section 4.4 for details on free volume calculation. The increased free volume per P2VP/NMP^+ functional site at the interface can be attributed to the repulsive interactions between the PS and P2VP segments. This repulsion effect results in a less compact packing arrangement of

P2VP/NMP$^+$ chains at the interface. As established in the previous section, the water uptake per P2VP/NMP$^+$ functional site is uniform across both the interfacial region and the bulk region. Consequently, the increased free volume per P2VP/NMP$^+$ functional site at the interface results in reduced swelling when the same amount of water molecules is added compared to the bulk region. Figure 4.16b-c also shows an illustration of this effect. In the previous section, it was established that the thickness of the interface remains consistent across different molecular weight BCPs, indicating a higher fraction of interfaces in lower molecular weight BCPs (e.g., 13k-13k). Therefore, due to the lesser extent of swelling in the interfacial region upon the insertion of the same amount of water, BCP systems with a larger fraction of interfaces exhibit comparatively less overall swelling.

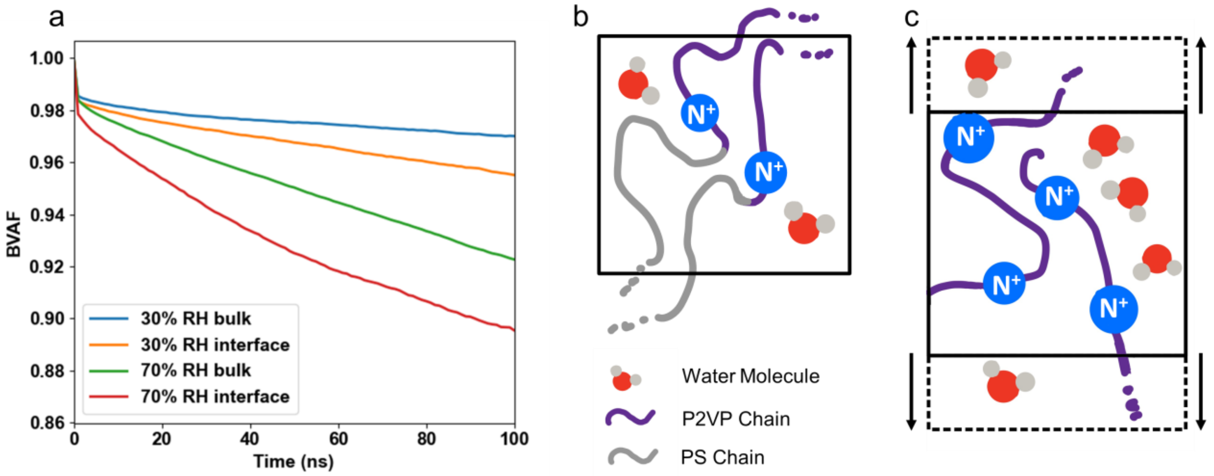

Figure 4.16. Comparison of P2VP/NMP+ chain behavior between interface and bulk. (a) Bond-vector autocorrelation function of P2VP/NMP+ backbones in the interfacial region at 30% relative humidity (orange) and 70% relative humidity (red), and in the bulk region at 30% relative humidity (blue) and 70% relative humidity (green). Illustration depicting the impact of free volume on the swelling ratio in the (b) interfacial region and (c) the bulk region.

To briefly sum up this section, we conducted molecular dynamics (MD) simulations to investigate the influence of the interface on 13k-13k PS-b-P2VP/NMP$^+$I$^-$ block copolymer systems under different relative humidity conditions. Our results indicate that the water uptake per

P2VP/NMP$^+$ functional site remains consistent across both the interface and bulk regions. Additionally, we found that the presence of the interface does not affect the solvation behavior of water molecules at any relative humidity level. Interestingly, we observed a faster polymer dynamic at the interfacial region, which can be attributed to the 53% larger free volume per P2VP/NMP$^+$ functional site compared to the bulk region. As a result, the interfacial region experiences reduced swelling when the same amount of water is introduced. This finding provides an explanation for the variation in swelling ratio observed in block copolymers with different molecular weights, with systems containing a higher proportion of interfaces showing relatively lower overall swelling.

4.2.4 Relationship between interface, water concentration and ion transport

Conductivity of homopolymer and BCEs were compared in **Figure 4.17**a-c. Conductivity increases nearly 3 orders of magnitude with increasing RH for all polymers as ion transport in hydrated polymer electrolytes follows water-assisted mechanism.[29] σ of BCEs is lower than σ_{Homo} at all RH levels with this difference decreasing with increasing humidity. To exclude the IEC difference between BCEs and homopolymer, we further compared the normalized σ of BCEs with respect to volume fraction of P2VP/NMP$^+$I$^-$ domain ($\sigma_{BCEs}/\varphi_{P2VP}$, namely σ of the conducting P2VP/NMP$^+$I$^-$ domain) with σ_{Homo}. Still, $\sigma_{BCEs}/\varphi_{P2VP}$ is lower than σ_{Homo} over all RH as shown in **Figure 4.17**a-c. On the contrary, higher conductivity of BCE than homopolymer counterpart has been reported for some other polymer electrolyte materials.[16,30] We speculate that properties like size of the mobile ions, ion dissociation, and polymer chain flexibility might affect this behavior. Note that in this work conductivity was measured on parallel lamellae of BCEs with single-grain structure, where no impediments for ion transport across defects[31] and grain boundaries[32] exist in the BCE system.

We are interested in the intrinsic conductivity difference between conducting domain in BCEs of different molecular weight. We first compared conductivity of P2VP/NMP$^+$I$^-$ domain σ_c and σ_{Homo} at various RH levels (**Figure 4.17**d). σ_c of different BCEs differed from each other and were all lower than σ_{Homo}. To compare the σ_c of different BCEs in a more distinct fashion, all σ_c were normalized to σ_{Homo} as shown in **Figure 4.17**e. Interestingly, $\sigma_{n,13k-13k} > \sigma_{n,25k-25k} > \sigma_{n,57k-57k}$ at every RH level, which means P2VP/NMP$^+$I$^-$ domain of 13k-13k is the most ionic conductive among these BCEs. Based on equation (1), we know thickness used for conductivity calculation can affect the conductivity value. Nevertheless, $\sigma_{n,13k-13k}$ is almost two time higher than $\sigma_{n,57k-57k}$ at 90% RH, while thickness expansion difference is not that much (39% vs. 49%). Therefore, intrinsic conductivity of P2VP/NMP+I- domain in these BCEs is different. Some work attributed this difference to the smaller size of the domain confining formation of ionic clusters within ionic domain, which in turn reduced the activation energy of ionic hopping.[33] However, this might not be universal to other materials as many intrinsic factors play a role. On the other hand, in this work we have gained adequate insights on the water uptake and volume expansion of different BCEs, allowing us to interpret the conductivity difference from the perspective of water concentration in the hydrated domain. As we discussed, hydration number in 13k-13k approximately equals to that of 25k-25k and 57k-57k while 13k-13k swells the least among all the BCEs, giving 13k-13k the highest water concentration (c_w) in ionic domain at every RH level. Conductivity of P2VP/NMP$^+$I$^-$ domain was plotted against c_w as shown in **Figure 4.17**f. Apparently, conductivity is largely dependent on c_w no matter what molecular weight the BCE is as all the data points follow the same trend. Conductivity increases fast with c_w especially when

c_w is pretty low. Thus, we conclude that higher conductivity of P2VP/NMP+I- domain in 13k-13k is achieved because of higher water concentration presented in the system.

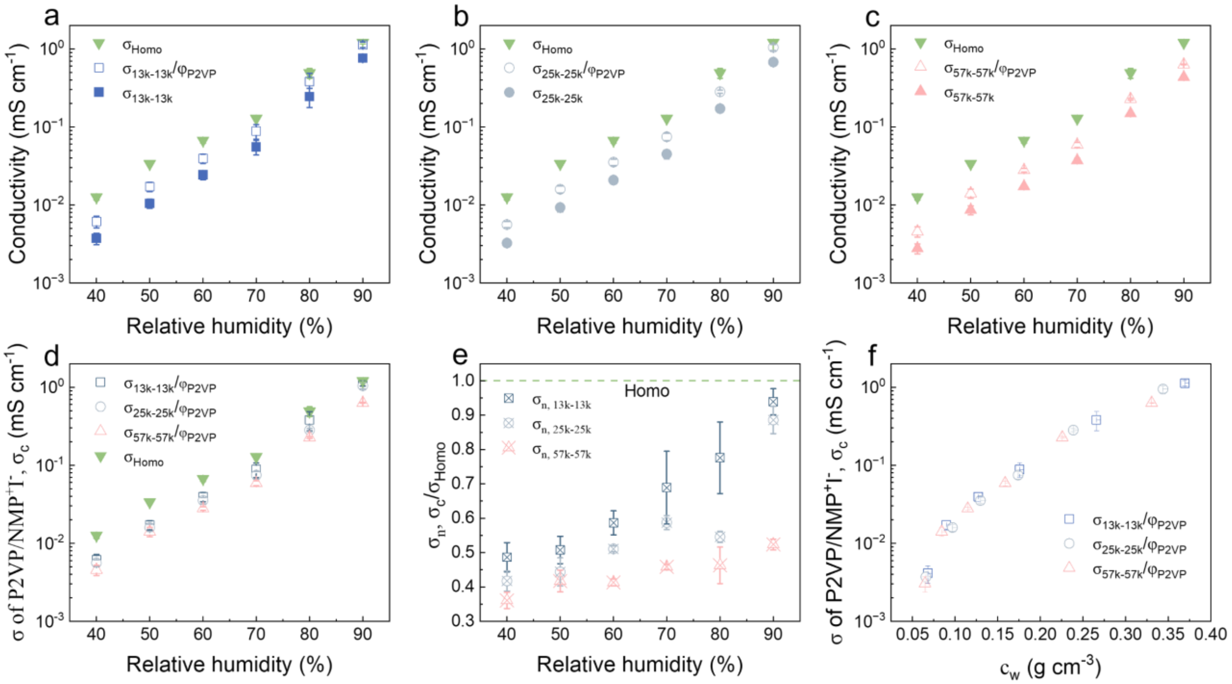

Figure 4.17. Conductivity results of BCEs and homopolymer. σ of homopolymer, σ of conducting P2VP domain in BCEs, and corresponding σ of BCEs for (a) 13k-13k, (b) 25k-25k, and (c) 57k-57k as a function of RH. (d) σ of conducting P2VP/NMP^{+}I^{-} in BCEs and homopolymer as a function of RH. (e) Normalized σ of conducting P2VP/NMP^{+}I^{-} in BCEs with respect to homopolymer. Green dashed line represents baseline of homopolymer ($\sigma_n = 1$). (f) σ of conducting P2VP/NMP^{+}I^{-} in BCEs as a function of water concentration.

4.3 Conclusion

In summary, we chose BCEs of 3 different molecular weight (13k-13k, 25k-25k, and 57k-57k) and employed BCE thin film of parallel lamellae structure as a platform. Coupled with techniques allowing measurements in thin film format, we investigated polymer electrolyte properties such as water uptake, swelling ratio, and ionic conductivity in a quantitative manner. The lamellar morphology of self-assembled BCP can be well-retained after functionalization of one block and addition of water into the conducting domain. Although hydration number of conducting domain in BCEs is similar to each other, swelling ratio of conducting domain in BCEs varies, leading to different water concentration in the conducting P2VP/NMP$^+$I$^-$ domain. Among these BCEs, P2VP/NMP$^+$I$^-$ in 13k-13k has the highest water concentration, which is attributed to highest volume fraction of interface. We used MD simulation to explain the variation in swelling ratio observed in block copolymers with different molecular weights. As a result, highest water concentration in 13k-13k gives rise to the highest ionic conductivity. These results provide fundamental understanding on water uptake, swelling ratio and ion transport in BCEs, shedding light on the design of anion exchange membranes to realize higher performance in electrochemical applications.

4.4 Methodology

4.4.1 Experimental section

Materials. Three block copolymers Poly (styrene-b-2 vinyl pyridine) (PS-*b*-P2VP) (13k-13k, 25k-25k, 57k-57k) and homopolymer P2VP (Mn = 25 kg mol^{-1}) were bought from Polymer Source Inc. and used as is. The cross-linked polystyrene solution (x-PS) was received from AZ Electronic Materials. All other chemicals (methyl iodide, toluene, 2-propoanol, *N*-methyl-2-pyrrolidone, acetone) were purchased from Sigma-Aldrich or Fisher Scientific and used without further purification. 5 MHz Au Quartz Crystals for Quartz Crystal Microbalance (QCM) measurement were bought from Gamry. The interdigitated electrodes (IDEs) were fabricated on semiconducting polished wafer (1 μm thermally grown oxide layer) received from WRS materials. Negative photoresist (AZ nLof 2020) and developer (AZ 300 MIF) for microfabrication were both purchased from AZ Electronic Materials.

Block copolymer characterizations. The molecular weight and dispersity (Đ) of BCPs were measured by Shimadzu gel permeation chromatography (GPC) system equipped with a Wyatt

DAWN HELEOS II multi-angle light scattering detector. THF with 250 ppm of BHT was used as the eluent. Small angle X-ray scattering (SAXS) was performed on block copolymers to determine domain spacing using SAXSLAB GANESHA instrument at the University of Chicago. Bulk samples of BCP were first annealed at 250 °C for two days under vacuum for microphase separation and were then placed on stage with double sided tape for SAXS measurement. The domain spacing, L_0, was determined as $2\pi/q^*$, where q^* is the primary scattering peak. Atomic force microscopy (AFM) with tapping mode was performed (Cypher ES AFM) at the University of Chicago MRSEC Facility. AFM data was analyzed using Gwyddion software. Fourier Transform infrared (FTIR) measurement were performed on PerkinElmer Frontier FT-IR spectrometer in the range of 2000 cm^{-1} to 1000 cm^{-1} with 20 scans using an attenuated total reflectance (ATR) accessory to determine the degree of methylation level.

Self-assembly of parallel lamellae PS-*b*-P2VP/NMP$^+$I$^-$ on IDEs. A series of PS-*b*-P2VP solutions with various polymer concentration, using toluene as solvent, were prepared under ambient conditions. First, the solutions of S2VP polymer were left to stir for 6 hours before using syringe-driven filter to remove undissolved, if any, purities. The IDEs[21] surfaces were homogenized with thin cross-linked polystyrene layer (*ca.* 5 nm) to ensure uniform wetting of S2VP polymer on the substrate and achieve symmetric parallel lamella. The x-PS solution was first spin coated onto the IDEs surface to generate a thin layer, which was subsequently annealed at 250 °C for 5 min to cross-link the mat. Thin films of S2VP polymer were then prepared by spin coating onto x-PS coated IDEs with polymer solutions to achieve desirable thickness (integer number of L_0 for parallel lamella with no hole or island). The film thickness on IDEs were determined by measuring thickness of witness polymer films spin coated on Si with native oxide under the same conditions with ellipsometry (J.A. Woollam alpha-SE ellipsometer). Then the

S2VP film were annealed on hot plate at 250 °C for 5 min to drive phase separation process and generate parallel lamella morphology on IDEs. The formed structure was examined with optical microscopy (BX60 Olympus). Then the samples were placed inside a 250 ml jar with 2 ml methyl iodide in a 4 ml vial for 24 hours to functionalize the P2VP block.[22]

***In-situ* measurement of thin film thickness under controlled relative humidity (RH).** Parallel lamellae of PS-*b*-P2VP/NMP$^+$I$^-$ were first fabricated on silicon wafer (1×1 inch) following the same procedures as on IDEs. Then the sample was placed on a liquid cell stage (500 µl Alpha Liquid Cell) installed on the ellipsometer (J.A. Woollam alpha-SE). The liquid cell chamber was subsequently fastened firmly onto the sample surface to ensure sealed environment. Then humidified air generated by Linkam RH95 Humidity Controller was connected to the flow cell to control the RH level for ellipsometry measurement. Film thickness was recorded after equilibrium state was reached at certain RH for 5 min.

Measurement of thin film water uptake *via* QCM. Parallel lamellae of PS-*b*-P2VP/NMP$^+$I$^-$ were first fabricated on 5 MHz Au quartz crystal following the same procedures as on IDEs. Then the crystal was placed into the QCM (Gamry eQCM 10M) with a small piece of tape (*ca*. 2 mm^2) attached to the overlapping area on the backside to resist ringing effect of the quartz crystal as suggested by Gamry technician. Relative humidity of the working chamber, in which water uptake was measured, was controlled by connecting Linkam RH95 Humidity Controller to the inlet of QCM chamber. Thermal circulator (Huber mini chiller 300) was used during the measurement to keep the temperature stable at 25 °C. The samples were equilibrated for 10 min at each RH level before changing the RH to the next level. The change of mass was calculated by frequency shift as equation S1,

$$\frac{\Delta m}{\Delta f} = 4.24\, ng/Hz \tag{S1}$$

where Δm is the water uptake of polymer thin film, and Δf is the frequency shift due to change of mass measured by QCM. Three samples were prepared and measured for each material.

X-ray reflectivity measurement on multilayer BCEs samples. X-ray Reflectivity measurements were conducted on a SmartLab reflectometer, with a Cu Kα X-ray source in the high-resolution geometry with a 2 bounce Ge monochromator. Data analysis was conducted using the Refnx package[34] according to previously described methods[26,35]. The model used to simulate the data consisted of the PS-b-P2VP in an asymmetric wetting stack with an ~6 nm thick layer of PS at the bottom substrate to account for the brush.

Ionic conductivity measurement by electrochemical impedance spectroscopy (EIS). The impedance of thin film was measured on IDEs using Gamry Reference 600+. Polymer coated on the two pads of IDEs were scraped by commercial Q-tip to ensure good electrical contact. IDEs were then placed inside a humidity chamber (ESPEC SH-242) with temperature set at 25 °C under different RH levels from 40% to 90%. The polymer thin film was equilibrated for 10 min before impedance measurement. A 50 mV AC potential was applied at frequencies ranging from 1 Hz to 1 MHz. Then the impedance data was fit to equivalent circuit model using Gamry Echem Analyst software. The obtained resistance value was then used to calculate ionic conductivity of polymer electrolytes.

Determination of methylation level in P2VP block. Methylation level is specified as f, mole fraction of 2VP/NMP^{+}I^{-} unit in the P2VP domain. This value was estimated by FTIR measurement, which can be described as equation S2,

$$f = \frac{A_{\mathrm{C}-N^{+}}}{A_{\mathrm{C}-N^{+}} + A_{\mathrm{C-N}}} \tag{S2}$$

where $A_{\mathrm{C}-N^{+}}$ is the integrated area of peaks associated with C-N^{+} stretching, and $A_{\mathrm{C-N}}$ is the integrated area of peaks associated with C-N stretching. C–N^{+} stretching was observed at 1630 cm^{-1}, while C-N signal intensity was displayed in the range of 1570–1590 cm^{-1} and the signal increased with prolonged exposure time to methyl iodide vapor. This method has been reported elsewhere with the same chemistry.[2] Regarding sample preparation for FTIR characterization, 5 nm x-PS was first spin coated on gold-coated (100 nm) silicon wafers (1 × 1 cm^{2}), which were chosen as substrates due to excellent reflectance. Three different BCP thin film of 2 L_0 thickness and homopolymer (*ca.* 40 nm) were then spin coated on the x-PS coated substrates. The samples were then placed on the bottom of a 250 ml dark jar with 2 ml methyl iodide inside for a series of exposure time (2h, 6h, 12h, 24h, and 48h). It is worth to note that the amount of methyl iodide was adequate under all circumstances.

Calculation of thickness of individual domain and swelling ratio. After self-assembly of parallel lamellae on silicon wafer, film thickness of 2 L_0 was measured by ellipsometer. As the PS and P2VP domain share the same volume fraction, total thickness (sum of disconnected domains) of PS and P2VP domain are given by equation S3,

$$h_{PS} = h_{P2VP} = h_{BCP}/2 \tag{S3}$$

where h_{PS} is total thickness of the PS domain, h_{P2VP} is total thickness of the P2VP domain, and h_{BCP} is the thickness of 2 L_0 parallel lamellar BCP.

Then the sample was exposed to MeI vapor for 24 hours to functionalize the P2VP domain to hydrophilic P2VP/NMP^{+}I^{-} domain, which swells when exposed to humidified environment. Since the thickness of PS domain remains constant regardless of RH change, the total thickness of P2VP/NMP$^+$I$^-$ domain then can be calculated by equation S4,

$$h_{P2VP/NMP^+I^-} = h_{BCP/MeI} - h_{PS} \tag{S4}$$

where $h_{BCP/MeI}$ is the thickness of methylated BCP lamellae. When pure nitrogen gas (flow rate controlled to be the same as RH95 Humidity Controller) was connected to the liquid cell inlet, thickness of non-hydrated P2VP/NMP+I- domain can be obtained. Swelling ratio of ion conducting P2VP/NMP$^+$I$^-$ domain was then calculated by equation S5,

$$swelling\ ratio = \frac{h_{BCP/MeI} - h_0}{h_0} \tag{S5}$$

where h_0 is the thickness of methylated P2VP domain at 0 RH. Four samples were measured for each material for better reproducibility.

Calculation of hydration number. Hydration number, λ, here is specified as the number of surrounding water molecules per 2VP/NMP$^+$ unit, which can be calculated by equation S6,

$$\lambda = \frac{m_{H_2O} \cdot M_{2VP}}{M_{H_2O} \cdot f \cdot S \cdot h_{P2VP} \cdot \rho_{P2VP}} \tag{S6}$$

where m_{H_2O} is the weight of water added to the P2VP/NMP$^+$I$^-$ domain, M_{H_2O} is the molecular weight of water (18.02 g mol^{-1}), f is the methylation level determined by FTIR (0.53), S is the overlapping area of two electrodes of QCM crystal (0.24 cm^2), M_{2VP} is the molecular weight of 2VP unit (105.14 g mol^{-1}), h_{P2VP} is the total thickness of P2VP domain before methylation, and ρ_{P2VP} is the mass density of P2VP (0.9985 g cm^3) before methylation. Film thickness and water uptake were measured at different RH, thus λ as a function of RH can be obtained.

4.4.2 Simulation section

In this work, we use Theoretical Informed Coarse Grain (TICG) model to generate the PS-*b*-P2VP/NMP+I- BCP equilibrium topology.[36] Then we backmapped the coarse grain results to all-atom representation. We then relaxed the all-atom system using GROMACS version 2020[37,38] packages with GPU acceleration.

TICG Model. We have 48 chains randomly generated in a $1\times1\times1.61$ Rg^3 box, where Rg is the radius of gyration of chains. Each chain has 40 beads with 20 A-type beads and 20 B-type beads. In the simulation, compatibility parameter χN is 25, compressibility parameter κN is, square root of invariant degree of polymerization $\sqrt{\bar{N}}$ is 30, bond length is 0.169. After 1 million Monte Carlo steps, lamellar morphology was obtained.

Backmapping. We mapped six monomers to each polymer bead. Since the distance between polymer beads fluctuates, the number of monomers we mapped for each bead changes accordingly to reduce overlapping or stretching between monomers. 53% of the P2VP chains were functionalized with NMP+ to remain consistency with experiments. To minimize overlapping or stretching between monomers, the number of mapped monomers for each bead fluctuates according to the fluctuating distances between polymer beads. Iodide ions were then randomly inserted into the P2VP/NMP+ domain. The resulting system has 118 PS monomers per chain and 120 P2VP/NMP+ monomers per chain, with 3050 iodide ions. The energy of this resulting system was then minimized using LAMMPS. We then relaxed the system in NVE ensemble in LAMMPS with soft potentials to remove ring interlocking. The resulting system was then transferred to GROMACS and utilized as the initial system for further relaxation.

All-atom Simulation. Molecular dynamics (MD) simulations were conducted using GROMACS version 2020[37,38] packages with GPU acceleration. Polymer chains were terminated with hydrogen atoms, and the polymer backbone of P2VP chains was modeled using parameters from a polystyrene chain.[39,40] The pyridine side group was modeled using parameters from the OPLS-AA force field,[41] while parameters for the methylpyridinium side group were obtained from Sambasivarao and Acevedo,[42] where the authors derived OPLS-AA-based force field parameters for ionic liquids, including the side group of interest. Iodide ion parameters were taken from Joung and Cheetham[43] and water molecules were modeled using SPC/E parameters.[44] The energy of this initial configuration was then minimized using the steepest decent minimization algorithm with a stopping criterion reached when the maximum total force of the system was less than 10.0 kJ/mol/nm. Electrolytes and ions were equilibrated for 30 ns in an NPT ensemble using a Berendsen barostat[45] at 1 bar, velocity-rescaling thermostat at 300 K, and a time step of 1 fs. Water molecules were subsequently added to the equilibrated system based on experimentally measured hydration numbers at different relative humidity levels. The hydrated systems were then equilibrated for 30 ns in an NPT ensemble with fixed x and y direction box length using a Berendsen barostat[45] at 1 bar, velocity-rescaling thermostat at 300 K, and a time step of 1 fs. Production runs were then carried out in the NVT ensemble at 300K using Nose-Hoover as the thermostat[46] for 200 ns with a 2 fs timestep. MD trajectory data were stored every 10 ps. The particle-particle-mesh Ewald summation method was used to compute the electrostatic interactions.[47] Bond lengths between hydrogens and heavy atoms were constrained using the LINCS algorithm. A cutoff of 1.1 nm was set for both the Lennard-Jones (LJ) and Coulombic interactions.[48] Atoms residing in the interfacial region (i.e., 9 nm – 12 nm in z direction for 30% RH and 10 nm – 13 nm in z direction for 70% RH) for more than 90% of the time are characterized as interfacial atoms. Atoms residing in the bulk region (i.e., 4.5 nm – 7.5 nm in z direction for 30% RH and 5.5 nm – 8 nm in z direction for 70% RH) for more than 90% of the time are characterized as bulk atoms. Please refer to Figure 4.12 for the number density profiles of the PS domain and P2VP/NMP+ domain, including the interfacial and bulk regions, at 30% RH and 70% RH.

Bond-vector Autocorrelation Function (BVAF). The bond-vector autocorrelation function (BVAF) is calculated as $\langle b_i(t) \cdot b_i(0) \rangle$, where $b_i(t)$ represents the bond vector between atom i and atom $i + 1$ at time t. In this analysis, BVAF was computed using the backbone bonds of the polymer chains. In the P2VP/NMP+ domain, the interfacial bonds were defined as the consecutive 15 backbone bonds starting from the junction point connecting PS to P2VP/NMP+ in each chain. The bulk bonds, on the other hand, were defined as the consecutive 15 backbone bonds within the bulk P2VP/NMP+ region (refer to the last section for the definition of the bulk region).

Free Volume Calculation. Free volume was calculated using GROMACS version 2020. The program attempts to insert a probe into the simulation box, and if the distance between the probe and any atom is smaller than the sum of their van der Waals (VDW) radii, the position is considered to be occupied or non-free. A probe radius of 0 was utilized to calculate the true free volume.[49] The VDW radii employed in the calculations were obtained from Bondi (1964).[50] In the interfacial region, the total volume was determined by considering only the volume within that specific region. When calculating the free volume, the probe was inserted solely in the interfacial region. Conversely, for the bulk region, the total volume was calculated by considering only the volume within the bulk region. During the free volume calculation, the probe was inserted exclusively in the bulk region. The calculated free volume was subsequently normalized by dividing it by the total number of P2VP/NMP+ functional sites present in the corresponding region.

4.5 References

(1) Hickner, M. A.; Ghassemi, H.; Kim, Y. S.; Einsla, B. R.; McGrath, J. E. Alternative Polymer Systems for Proton Exchange Membranes (PEMs). *Chem. Rev.* **2004**, *104* (10), 4587–4611. https://doi.org/10.1021/cr020711a.

(2) Jinnouchi, R.; Kudo, K.; Kodama, K.; Kitano, N.; Suzuki, T.; Minami, S.; Shinozaki, K.; Hasegawa, N.; Shinohara, A. The Role of Oxygen-Permeable Ionomer for Polymer Electrolyte Fuel Cells. *Nat. Commun.* **2021**, *12* (1). https://doi.org/10.1038/s41467-021-25301-3.

(3) Liu, D.; Kyriakides, S.; Case, S. W.; Lesko, J. J.; Yanxiang, L. I.; Mcgrath, J. E. Tensile Behavior of Nafion and Sulfonated Poly(Arylene Ether Sulfone) Copolymer Membranes and Its Morphological Correlations. *J. Polym. Sci. Part B Polym. Phys.* **2006**, *44* (10), 1453–1465. https://doi.org/10.1002/polb.20813.

(4) Tang, H.; Peikang, S.; Jiang, S. P.; Wang, F.; Pan, M. A Degradation Study of Nafion Proton Exchange Membrane of PEM Fuel Cells. *J. Power Sources* **2007**, *170* (1), 85–92. https://doi.org/10.1016/j.jpowsour.2007.03.061.

(5) Fernandes, A. C.; Ticianelli, E. A. A Performance and Degradation Study of Nafion 212 Membrane for Proton Exchange Membrane Fuel Cells. *J. Power Sources* **2009**, *193* (2), 547–554. https://doi.org/10.1016/j.jpowsour.2009.04.038.

(6) Han, J.; Zhu, L.; Pan, J.; Zimudzi, T. J.; Wang, Y.; Peng, Y.; Hickner, M. A.; Zhuang, L. Elastic Long-Chain Multication Cross-Linked Anion Exchange Membranes. *Macromolecules* **2017**, *50* (8), 3323–3332. https://doi.org/10.1021/acs.macromol.6b01140.

(7) Gu, S.; Cai, R.; Luo, T.; Chen, Z.; Sun, M.; Liu, Y.; He, G.; Yan, Y. A Soluble and Highly Conductive Ionomer for High-Performance Hydroxide Exchange Membrane Fuel Cells. *Angew. Chemie - Int. Ed.* **2009**, *48* (35), 6499–6502. https://doi.org/10.1002/anie.200806299.

(8) Hren, M.; Božič, M.; Fakin, D.; Kleinschek, K. S.; Gorgieva, S. Alkaline Membrane Fuel Cells: Anion Exchange Membranes and Fuels. *Sustain. Energy Fuels* **2021**, *5* (3), 604–637. https://doi.org/10.1039/d0se01373k.

(9) Tsai, T. H.; Ertem, S. P.; Maes, A. M.; Seifert, S.; Herring, A. M.; Coughlin, E. B. Thermally Cross-Linked Anion Exchange Membranes from Solvent Processable Isoprene Containing Ionomers. *Macromolecules* **2015**, *48* (3), 655–662. https://doi.org/10.1021/ma502362a.

(10) Dang, H.-S.; Jannasch, P. Exploring Different Cationic Alkyl Side Chain Designs for Enhanced Alkaline Stability and Hydroxide Ion Conductivity of Anion-Exchange Membranes. *Macromolecules* **2015**, *48* (16), 5742–5751. https://doi.org/10.1021/acs.macromol.5b01302.

(11) Barnett, A.; Karnes, J. J.; Lu, J.; Major, D. R. J.; Oakdale, J. S.; Grew, K. N.; McClure, J. P.; Molinero, V. Exponential Water Uptake in Ionomer Membranes Results from Polymer

Plasticization. *Macromolecules* **2022**, *55* (15), 6762–6774. https://doi.org/10.1021/acs.macromol.2c01042.

(12) Pestrak, M.; Li, Y.; Case, S. W.; Dillard, D. A.; Ellis, M. W.; Lai, Y.-H.; Gittleman, C. S. The Effect of Mechanical Fatigue on the Lifetimes of Membrane Electrode Assemblies. *J. Fuel Cell Sci. Technol.* **2010**, *7* (4). https://doi.org/10.1115/1.4000629.

(13) Vandiver, M. A.; Caire, B. R.; Carver, J. R.; Waldrop, K.; Hibbs, M. R.; Varcoe, J. R.; Herring, A. M.; Liberatore, M. W. Mechanical Characterization of Anion Exchange Membranes by Extensional Rheology under Controlled Hydration. *J. Electrochem. Soc.* **2014**, *161* (10), H677–H683. https://doi.org/10.1149/2.0971410jes.

(14) Kim, S.; Ahn, B. K.; Mench, M. M. Physical Degradation of Membrane Electrode Assemblies Undergoing Freeze/Thaw Cycling: Diffusion Media Effects. *J. Power Sources* **2008**, *179* (1), 140–146. https://doi.org/10.1016/j.jpowsour.2007.12.114.

(15) Lim, C.; Ghassemzadeh, L.; Van Hove, F.; Lauritzen, M.; Kolodziej, J.; Wang, G. G.; Holdcroft, S.; Kjeang, E. Membrane Degradation during Combined Chemical and Mechanical Accelerated Stress Testing of Polymer Electrolyte Fuel Cells. *J. Power Sources* **2014**, *257*, 102–110. https://doi.org/10.1016/j.jpowsour.2014.01.106.

(16) Ye, Y.; Sharick, S.; M. Davis, E.; I. Winey, K.; A. Elabd, Y. High Hydroxide Conductivity in Polymerized Ionic Liquid Block Copolymers. *ACS Macro Lett.* **2013**, *2* (7), 575–580. https://doi.org/10.1021/mz400210a.

(17) Jain, S. K.; Rawlings, D.; Antoine, S.; Segalman, R. A.; Han, S. Confinement Promotes Hydrogen Bond Network Formation and Grotthuss Proton Hopping in Ion-Conducting Block Copolymers. *Macromolecules* **2022**, *55* (2), 615–622. https://doi.org/10.1021/acs.macromol.1c01808.

(18) Kim, S. Y.; Park, M. J.; Balsara, N. P.; Jackson, A. Confinement Effects on Watery Domains in Hydrated Block Copolymer Electrolyte Membranes. *Macromolecules* **2010**, *43* (19), 8128–8135. https://doi.org/10.1021/ma101620k.

(19) Sharon, D.; Bennington, P.; Dolejsi, M.; Webb, M. A.; Dong, B. X.; De Pablo, J. J.; Nealey, P. F.; Patel, S. N. Intrinsic Ion Transport Properties of Block Copolymer Electrolytes. *ACS Nano* **2020**, *14* (7), 8902–8914. https://doi.org/10.1021/acsnano.0c03713.

(20) Kim, O.; Jo, G.; Park, Y. J.; Kim, S.; Park, M. J. Ion Transport Properties of Self-Assembled Polymer Electrolytes: The Role of Confinement and Interface. *J. Phys. Chem. Lett.* **2013**, *4* (13), 2111–2117. https://doi.org/10.1021/jz4009536.

(21) Liu, C.; Sharon, D.; Grocke, G.; Patel, S. N.; Bennington, P.; Nealey, P. F.; Burnett, V. F.; Dong, B. X.; Kambe, Y.; Dolejsi, M. Interrogation of Electrochemical Properties of Polymer Electrolyte Thin Films with Interdigitated Electrodes. *J. Electrochem. Soc.* **2018**, *165* (16), H1028–H1039. https://doi.org/10.1149/2.0291816jes.

(22) Arges, C. G.; Kambe, Y.; Suh, H. S.; Ocola, L. E.; Nealey, P. F. Perpendicularly Aligned, Anion Conducting Nanochannels in Block Copolymer Electrolyte Films. *Chem. Mater.* **2016**, *28* (5), 1377–1389. https://doi.org/10.1021/acs.chemmater.5b04452.

(23) Smith, A. P.; Douglas, J. F.; Meredith, J. C.; Amis, E. J.; Karim, A. Combinatorial Study of Surface Pattern Formation in Thin Block Copolymer Films. *Phys. Rev. Lett.* **2001**, *87* (1), 15503. https://doi.org/10.1103/PhysRevLett.87.015503.

(24) Detallante, V.; Langevin, D.; Chappey, C.; Métayer, M.; Mercier, R.; Pinéri, M. Water Vapor Sorption in Naphthalenic Sulfonated Polyimide Membranes. *J. Memb. Sci.* **2001**, *190* (2), 227–241. https://doi.org/10.1016/S0376-7388(01)00437-9.

(25) Chen, X. C.; Wong, D. T.; Yakovlev, S.; Beers, K. M.; Downing, K. H.; Balsara, N. P. Effect of Morphology of Nanoscale Hydrated Channels on Proton Conductivity in Block Copolymer Electrolyte Membranes. *Nano Lett.* **2014**, *14* (7), 4058–4064. https://doi.org/10.1021/nl501537p.

(26) Sunday, D. F.; Thelen, J. L.; Zhou, C.; Ren, J.; Nealey, P. F.; Kline, R. J. Buried Structure in Block Copolymer Films Revealed by Soft X-Ray Reflectivity. *ACS Nano* **2021**, *15* (6), 9577–9587. https://doi.org/10.1021/acsnano.0c09907.

(27) Chu, W.; Webb, M. A.; Deng, C.; Colón, Y. J.; Kambe, Y.; Krishnan, S.; Nealey, P. F.; De Pablo, J. J. Understanding Ion Mobility in P2VP/NMP+I- Polymer Electrolytes: A Combined Simulation and Experimental Study. *Macromolecules* **2020**. https://doi.org/10.1021/acs.macromol.9b02329.

(28) Chen, C.; Tse, Y.-L. S.; Lindberg, G. E.; Knight, C.; Voth, G. A. Hydroxide Solvation and Transport in Anion Exchange Membranes. *J. Am. Chem. Soc.* **2016**, *138* (3), 991–1000. https://doi.org/10.1021/jacs.5b11951.

(29) Salvatore, D. A.; Gabardo, C. M.; Reyes, A.; O'Brien, C. P.; Holdcroft, S.; Pintauro, P.; Bahar, B.; Hickner, M.; Bae, C.; Sinton, D.; Sargent, E. H.; Berlinguette, C. P. Designing Anion Exchange Membranes for CO2 Electrolysers. *Nat. Energy* **2021**, *6* (4), 339–348. https://doi.org/10.1038/s41560-020-00761-x.

(30) Mandal, M.; Huang, G.; Hassan, N. U.; Mustain, W. E.; Kohl, P. A. Poly(Norbornene) Anion Conductive Membranes: Homopolymer, Block Copolymer and Random Copolymer Properties and Performance. *J. Mater. Chem. A* **2020**, *8* (34), 17568–17578. https://doi.org/10.1039/d0ta04756b.

(31) Kambe, Y.; Arges, C. G.; Czaplewski, D. A.; Dolejsi, M.; Krishnan, S.; Stoykovich, M. P.; De Pablo, J. J.; Nealey, P. F. Role of Defects in Ion Transport in Block Copolymer Electrolytes. *Nano Lett.* **2019**, *19* (7), 4684–4691. https://doi.org/10.1021/acs.nanolett.9b01758.

(32) Chintapalli, M.; Chen, X. C.; Thelen, J. L.; Teran, A. A.; Wang, X.; Garetz, B. A.; Balsara, N. P. Effect of Grain Size on the Ionic Conductivity of a Block Copolymer Electrolyte. *Macromolecules* **2014**, *47* (15), 5424–5431. https://doi.org/10.1021/ma501202c.

(33) Beers, K. M.; Balsara, N. P. Design of Cluster-Free Polymer Electrolyte Membranes and Implications on Proton Conductivity. *ACS Macro Lett.* **2012**, *1* (10), 1155–1160. https://doi.org/10.1021/mz300389f.

(34) Nelson, A. R. J.; Prescott, S. W. Refnx: Neutron and X-Ray Reflectometry Analysis in

Python. *J. Appl. Crystallogr.* **2019**, *52*, 193–200. https://doi.org/10.1107/S1600576718017296.

(35) Sunday, D. F.; Chang, A. B.; Liman, C. D.; Gann, E.; Delongchamp, D. M.; Thomsen, L.; Matsen, M. W.; Grubbs, R. H.; Soles, C. L. Self-Assembly of ABC Bottlebrush Triblock Terpolymers with Evidence for Looped Backbone Conformations. *Macromolecules* **2018**, *51* (18), 7178–7185. https://doi.org/10.1021/acs.macromol.8b01370.

(36) Pike, D. Q.; Detcheverry, F. A.; Müller, M.; de Pablo, J. J. Theoretically Informed Coarse Grain Simulations of Polymeric Systems. *J. Chem. Phys.* **2009**, *131* (8), 84903. https://doi.org/10.1063/1.3187936.

(37) Plimpton, S. Fast Parallel Algorithms for Short-Range Molecular Dynamics. *J. Comput. Phys.* **1995**, *117* (1), 1–19. https://doi.org/https://doi.org/10.1006/jcph.1995.1039.

(38) Abraham, M. J.; Murtola, T.; Schulz, R.; Páll, S.; Smith, J. C.; Hess, B.; Lindahl, E. GROMACS: High Performance Molecular Simulations through Multi-Level Parallelism from Laptops to Supercomputers. *SoftwareX* **2015**, *1–2*, 19–25. https://doi.org/https://doi.org/10.1016/j.softx.2015.06.001.

(39) Müller-Plathe, F. Local Structure and Dynamics in Solvent-Swollen Polymers. *Macromolecules* **1996**, *29* (13), 4782–4791. https://doi.org/10.1021/ma9518767.

(40) Ndoro, T. V. M.; Voyiatzis, E.; Ghanbari, A.; Theodorou, D. N.; Böhm, M. C.; Müller-Plathe, F. Interface of Grafted and Ungrafted Silica Nanoparticles with a Polystyrene Matrix: Atomistic Molecular Dynamics Simulations. *Macromolecules* **2011**, *44* (7), 2316–2327. https://doi.org/10.1021/ma102833u.

(41) Jorgensen, W. L.; McDonald, N. A. Development of an All-Atom Force Field for Heterocycles. Properties of Liquid Pyridine and Diazenes. *J. Mol. Struct.* **1998**, *424*, 145–155.

(42) Sambasivarao, S. V; Acevedo, O. Development of OPLS-AA Force Field Parameters for 68 Unique Ionic Liquids. *J. Chem. Theory Comput.* **2009**, *5* (4), 1038–1050. https://doi.org/10.1021/ct900009a.

(43) Joung, I. S.; Cheatham, T. E. I. I. I. Determination of Alkali and Halide Monovalent Ion Parameters for Use in Explicitly Solvated Biomolecular Simulations. *J. Phys. Chem. B* **2008**, *112* (30), 9020–9041. https://doi.org/10.1021/jp8001614.

(44) Berendsen, H. J. C.; Grigera, J. R.; Straatsma, T. P. The Missing Term in Effective Pair Potentials. *J. Phys. Chem.* **1987**, *91* (24), 6269–6271. https://doi.org/10.1021/j100308a038.

(45) Berendsen, H. J. C.; van der Spoel, D.; van Drunen, R. GROMACS: A Message-Passing Parallel Molecular Dynamics Implementation. *Comput. Phys. Commun.* **1995**, *91* (1), 43–56. https://doi.org/https://doi.org/10.1016/0010-4655(95)00042-E.

(46) Evans, D. J.; Holian, B. L. The Nose–Hoover Thermostat. *J. Chem. Phys.* **1985**, *83* (8), 4069–4074. https://doi.org/10.1063/1.449071.

(47) Páll, S.; Hess, B. A Flexible Algorithm for Calculating Pair Interactions on SIMD

Architectures. *Comput. Phys. Commun.* **2013**, *184* (12), 2641–2650. https://doi.org/https://doi.org/10.1016/j.cpc.2013.06.003.

(48) Hess, B.; Bekker, H.; Berendsen, H. J. C.; Fraaije, J. G. E. M. LINCS: A Linear Constraint Solver for Molecular Simulations. *J. Comput. Chem.* **1997**, *18* (12), 1463–1472. https://doi.org/https://doi.org/10.1002/(SICI)1096-987X(199709)18:12<1463::AID-JCC4>3.0.CO;2-H.

(49) Jansen, J. C.; Macchione, M.; Tocci, E.; De Lorenzo, L.; Yampolskii, Y. P.; Sanfirova, O.; Shantarovich, V. P.; Heuchel, M.; Hofmann, D.; Drioli, E. Comparative Study of Different Probing Techniques for the Analysis of the Free Volume Distribution in Amorphous Glassy Perfluoropolymers. *Macromolecules* **2009**, *42* (19), 7589–7604. https://doi.org/10.1021/ma901244d.

(50) Bondi, A. Van Der Waals Volumes and Radii. *J. Phys. Chem.* **1964**, *68* (3), 441–451. https://doi.org/10.1021/j100785a001.

Chapter 5

Conclusion

The work in this thesis demonstrates the powerfulness of studying ion transport in polymer electrolytes in thin film format, with which extrinsic factors can be avoided and insights into the molecular level ion transport mechanism can be obtained. Chapter 2 described the experimental techniques that enable the characterization tool to make the thin film platform work. These includes customized thin film thickness measurement under different relative humidity by equipping ellipsometer with relative humidity generator; quartz crystal microbalance (QCM) to measure the thin film water uptake in the ng scale with high resolution; interdigitated electrodes (IDEs) that were designed and fabricated in cleanroom to effectively measure the thin film ionic conductivity; x-Ray tool to probe the buried structure in thin film.

In chapter 3, we proposed a strategy – crosslinking – to change the segmental dynamics of the polymer chain to study the effect on ion transport property. Surprisingly, the reduced chain dynamics has no influence on ion transport. However, due to the different degree of crosslinking, the water concentration in the polymer varies, which was found to be the key parameters that determined the ion transport efficiency. Basically, when the water concentration of the crosslinked material is the same as the uncrosslinked counterpart, the conductivity would be the same. This study has very high impact on the design of the polymer electrolytes. For example, materials with higher Tg can be synthesized to increase the mechanical property without worrying about sacrificing conductivity as long as the water concentration is kept.

In chapter 4, we took advantage of the knowledge obtained from chapter 3 to understand how the interface in block copolymer electrolytes affect ion transport through the confinement of water. We chose BCEs with different molecular weights to adjust the volume fraction of interface. Experiments tell us that the higher volume fraction of interface in lower molecular weight polymer can more effectively confine water in the interface, leading to higher conductivity due to higher water concentration. MD simulation explains the reason for the confinement of water in the interface. More free volume presents at the interface compared to the bulk, which enables accommodation of water without experiencing excessive swelling. This study is the first one in the hydrated block copolymer electrolytes field to unveil the role of interface in affecting ion transport by the confinement of water. BCEs with higher performance can thus be designed to solve the inferior conductivity problem for the anion exchange membrane fuel cells.